Summer 2022

Nickel Phosphide Photothermal Catalyst Development for CO2-Derived Solar Fuels

Hannah K. Hennig
Western Washington University, hannah.lazich@gmail.com

Recommended Citation

Hennig, Hannah K., "Nickel Phosphide Photothermal Catalyst Development for CO2-Derived Solar Fuels" (2022). *WWU Graduate School Collection*. 1126.
https://cedar.wwu.edu/wwuet/1126

Nickel Phosphide Photothermal Catalyst Development for CO_2-Derived Solar Fuels

By

Hannah K. Hennig (née Lazich)

Submitted for Partial Completion

of the Requirements for the Degree

Master of Science

ADVISORY COMMITTEE

Dr. Mark Bussell, Chair

Dr. Steven Emory

Dr. Robert Berger

GRADUATE SCHOOL

David L. Patrick, Dean

Master's Thesis

Hannah K. Hennig (née Lazich)

08/02/2022

Nickel Phosphide Photothermal Catalyst Development for CO_2-Derived Solar Fuels

A Thesis

Presented to the Faculty of

Western Washington University

In Partial Fulfillment

Of the Requirements for the Degree

Master of Science

by

Hannah K. Hennig (née Lazich)

August 2022

Abstract

Converting CO_2 to CO via the photocatalyzed reverse water gas shift (RWGS) reaction satisfies a critical step in the production of C1 solar fuels (e.g., CH_4, CH_3OH) and longer hydrocarbons via the Fischer-Tropsch process. Oxide-supported nickel phosphides (Ni_xP_y) are an emerging class of photocatalysts with a number of accessible crystalline phases. Additionally, the broad-spectrum absorption of Ni_xP_y materials affords photo-induced local heating to drive catalytic processes at mild operating temperatures. In the current project, Ni_xP_y with different P/Ni molar ratios were investigated as RWGS catalysts on two types of support materials: 1) silica (SiO_2) as a relatively inert support, and 2) a reducible oxide support (TiO_2).

Ni_xP_y/SiO_2 catalysts (2.5 wt%) were synthesized via incipient wetness impregnation followed by temperature-programmed reduction (TPR); crystalline phases (Ni_2P, $Ni_{12}P_5$, Ni_3P) were identified using X-ray diffraction and compositions were determined by inductively coupled plasma optical emission spectroscopy (ICP-OES), and ongoing RWGS studies were carried out in a batch photoreactor using a Xe lamp (300 W) with the gas composition monitored by gas chromatography. Initial studies were executed using a SiO_2 support, which is inactive for the RWGS reaction under light exposure, enabling the photocatalytic properties of the different Ni_xP_y phases to be probed. Trends of increasing CO selectivity and decreasing CO_2 conversion have emerged as the P/Ni molar ratio increases, while the photo enhancement (light/dark activity ratio) decreases. Studies were then repeated for 2.5 wt% Ni_xP_y/TiO_2 to evaluate the effect of a reducible oxide support and gain insight on the roles of the support and Ni_xP_y-support interface in determining the RWGS photocatalytic properties.

Acknowledgements

Thesis committee Chair:	Dr. Mark Bussell
Thesis Committee Members:	Dr. Steven Emory Dr. Robert Berger
Research Group members:	Jake Schare, Alex Bullock, Sam Baldwin, Michael Edwin, Evan Stern, Hannah Halstead, Reilly Lynch, and Ryan Hagmann
Instrument Specialists:	Dr. Michael Kraft, Dr. Steven Emory, Sam Danforth, Charles Wandler, and Kyle Mikkelson
Financial Support:	National Science Foundation (NSF) Research Corporation for Science Advancement NASA Washington Space Grant Consortium WWU Research and Sponsored Programs (RSP) Grant WWU Ross Travel Grant
Catalyst Synthesis:	Alex Bullock, Hannah Halstead, and Evan Stern
3D-Printed Material Design:	Jake Schare

Table of Contents

List of Figures

List of Tables

Chapter 1: Introduction

1.1 Climate Protection Goals

Global warming threatens catastrophic changes to the environment. On a global scale, risks include disruptions to physical systems such as glaciers, rivers, and coast lines; biological systems such as marine and terrestrial ecosystems; and human-managed systems such as food production and health services.[1] The Paris Agreement seeks to keep global warming below 2 °C relative to pre-industrial era levels through concerted mitigation efforts.[2] In the wake of such ambitions, the International Panel on Climate Change (IPCC) reported in its 2021 Assessment Report (AR6) a projected global warming of 1.5 °C by the early 2030s, underscoring the urgency with which action must be taken to minimize irreversible changes to the environment.[3]

Driving the climate crisis is the increasing concentration of greenhouse gases (GHGs), which accumulate in Earth's atmosphere and trap heat (i.e., the greenhouse effect). Some of these gases are naturally occurring—namely, water vapor (H_2O), carbon dioxide (CO_2), methane (CH_4), and nitrous oxide (N_2O)—and others are synthetic and have been introduced by humans through industrialization.[4] Among anthropogenic emissions, fossil fuel combustion represents the largest source of rising GHG concentrations.[5] As the global population grows, so too does energy demand; electricity, agriculture/food, transportation fuel, and commercial/residential heating production chains rely heavily on fossil fuels.[5] Common to the processes of burning fossil fuels (e.g., petroleum, natural gas, and coal) is the emission of CO_2, which accounts for the majority of human-driven GHG emissions.[5] To meet climate protection goals, mitigation of net CO_2 production is necessary.

1.2 Reverse Water Gas Shift Reaction

Equation 1: RWGS

$$CO_2(g) + H_2(g) \longrightarrow CO(g) + H_2O(g)$$

Equation 2: Fischer-Tropsch

$$(2n+1)H_2 + nCO \longrightarrow C_nH_{(2n+2)} + nH_2O$$

The photocatalytic conversion of CO_2 and renewable hydrogen (H_2) to carbon monoxide (CO) and H_2O via the reverse water gas shift reaction (RWGS, Equation 1) is a critical first step in the production of C1 solar fuels (e.g., methanol CH_3OH, methane CH_4) and longer chain hydrocarbons via the Fischer-Tropsch synthesis (FT, Equation 2).[6] CO_2 captured from point sources (e.g., fossil fuel power plants, cement production) could be a feedstock for the RWGS reaction and tandem FT systems as we transition industrial infrastructure away from fossil fuel reliance. Adsorption and permeable membrane approaches to CO_2 removal from multi-component flue gas is a complementary field of research making the RWGS approach increasingly feasible on an industrial scale.[7–11]

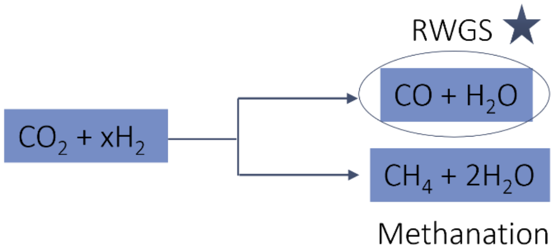

Figure 1. Parallel CO_2 hydrogenation pathways

At room temperature, the RWGS reaction is an endothermic process ($\Delta H_{298\ K}$ = +41 kJ/mol); achieving favorable conversion and high rate requires high temperatures and/or a catalyst.[12] When the uncatalyzed reaction is conducted in the 373-973 K temperature range, a parallel methanation reaction is favored and CH_4 is the main product observed (Figure 1).[13] High temperatures (> 973 K) are needed to achieve favorable conversion with high selectivity to CO via the thermal reaction.[13–15] To this aim, photothermal catalysis uses light as an energy source.

1.3 Photothermal Catalysis

In the effort to selectively produce CO under mild operating conditions (e.g., ≤ 573 K, ~1 atm), earth's most abundant energy source—the sun—becomes an attractive resource. Photothermal catalysis combines traditional thermal catalysis and photocatalysis to increase the thermal energy of the reactants and lower the transition state energy, respectively (Figure 2). A photothermal catalyst can lower the external heating requirements in one of two ways: 1) heat generated by a light-absorbing photocatalyst raises the temperature of adsorbed reactants, and 2) high local temperatures are generated by surface plasmonic resonance within a plasmonic photocatalyst.[6] Using strategic catalyst design, this indirect method of heating the RWGS reactants can improve CO_2 conversion efficiency and CO selectivity without relying on fossil fuel-powered furnaces.

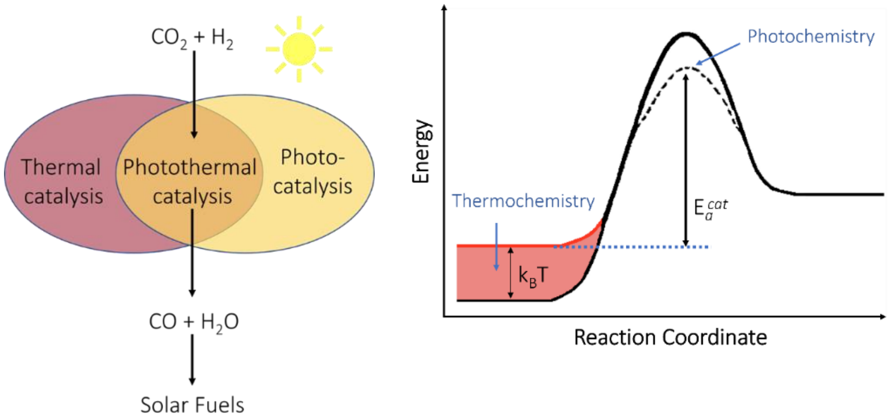

Figure 2. (Left) Venn diagram of photothermal design strategy. (Right) Reaction coordinate diagram of a generic photothermally catalyzed reaction. Figure adapted with permission from ref [20].

1.4 Heterogeneous Catalysis

Underpinning chemical manufacturing and fuel production systems is heterogeneous catalysis, in which solid-state materials catalyze gas- and liquid-phase reactions.[16,17] The RWGS process is a gas-phase reaction that relies upon the availability and regeneration of active sites on the catalyst surface. Nanoparticles (NPs) play a significant role in heterogeneous catalyst design, as their high surface-area-to-volume ratio (S/V) results in the chemical, optical, and electronic properties being heavily influenced by the modifiable surface structure rather than bulk properties.[18]

Commonly, NPs (e.g., gold, silver, metal phosphides) are supported on a high surface area substrate (e.g., silica, zeolites, graphene) to minimize sintering, control NP dispersal, and—potentially—contribute active sites for the catalyzed reaction (Figure 3)[14,17,19,20]

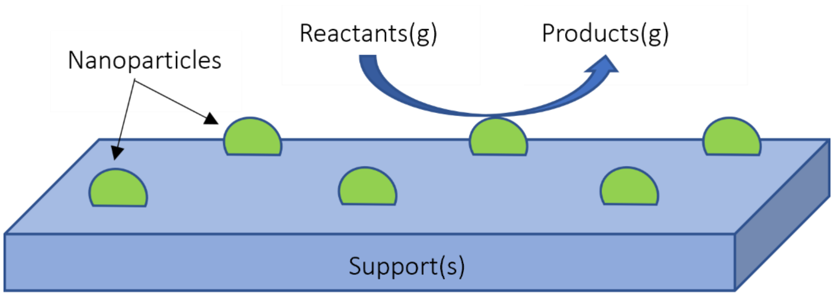

Figure 3. Schematic of a heterogeneous reaction of supported nanoparticles as a solid catalyst, gas phase reactants, and gas phase products.

For heterogeneous catalysis, a series of adsorption, reaction, and desorption steps must occur to form the desired product. The effect of these processes on the catalytic reaction rate is described by Sabatier's principle; reactants must adsorb strongly enough to facilitate a reaction, and weakly enough to desorb the resulting product (Figure 4).[21] In the case of the RWGS reaction, CO_2 and H_2 must adsorb to the catalyst surface and react to form CO and water vapor; if CO is too strongly adsorbed, it will remain on the surface and poison the catalyst. If CO_2 or H_2 are too weakly adsorbed, they will not stay adsorbed long enough to react. Additionally, selectivity toward the desired product is a requisite for an effective catalyst. NP, support, and NP-support interface can all influence the dominant intermediate pathways and, as such, must be finely tailored.

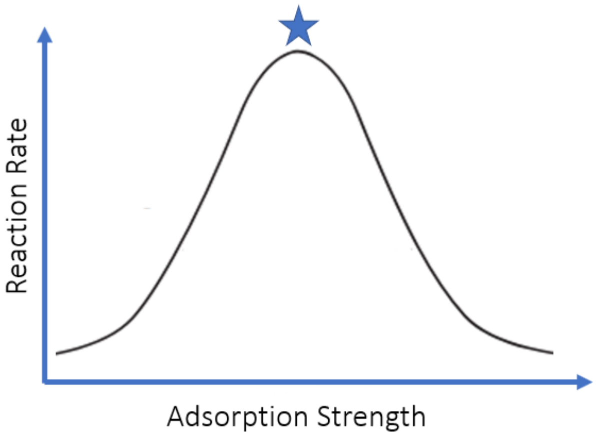

Figure 4. Volcano plot illustrating the Sabatier principle showing reaction rate as a function of adsorption strength.

1.5 Nickel-based RWGS Catalysts

The efficacy of various metal NPs (e.g., copper, nickel, palladium) as thermal catalysts for RWGS at high temperatures (>873 K) is supported by experimental and computational findings.[19,21,22] In a microkinetic study of eight metals as RWGS thermal catalysts (at 973 K), Qi et al. reported a CO formation activity trend of Rh~Ni > Pt~Pd > Cu > Co > Ru > Fe.[22] Among those with high catalytic activity, nickel (Ni) is particularly attractive due to its low cost and high abundance.[23] Nickel, in the form of a nickel phosphide (Ni_xP_y), has several accessible phases (e.g., Ni_2P, $Ni_{12}P_5$, and Ni_3P) with different Ni coordination geometries (Figure 5).[24] Under irradiation, Ni and its phosphides absorb light broadly across the entire solar spectrum, affording photo-induced local heating of a catalyst, thereby lowering the demand for external heating to achieve elevated reaction temperatures.[15,25]

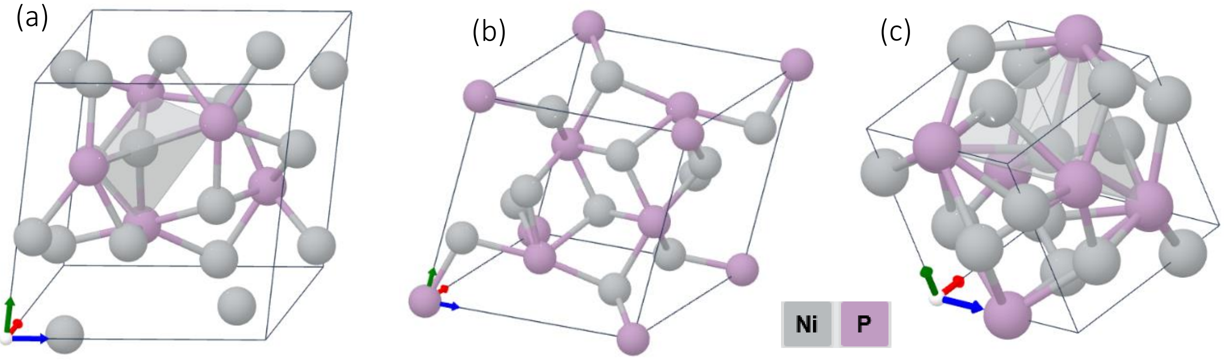

Figure 5. Crystalline structure of the unit cell of a) Ni_3P, b) $Ni_{12}P_5$, and c) Ni_2P with Ni and P atoms represented by grey and purple spheres, respectively. Structures reprinted from ref [24].

To elucidate the differences in the efficacy and selectivity of Ni-based catalysts for RWGS, it is useful to first look at Ni compared to Ni_xP_y performance. Xu et al. conducted a long-term stability study of the RWGS reaction on Ni/SiO_2 over 100 h of continuous irradiation at 563 K.[25] Following the reaction, notable sintering of the supported Ni NPs was observed by high resolution transmission electron microscopy (HRTEM), CO production decreased by 76%, and CO selectivity decreased by 15% from its initial performance.[25] In an earlier study by Du et al., aggregation of silica-supported Ni nanoparticles and reduced CO_2 HYD activity was observed at temperatures of 673 K and higher was accompanied by increased Ni–Ni coordination number.[26] Comparing the findings of the two studies leads to the conclusion that the reaction temperature in Xu et al.'s experiment—which combined external heating at 563 K and hypothesized photo-induced local heating of the Ni nanoparticles—likely reached ≥ 673 K, explaining the observed sintering.[25,26]

Xu et al. also investigated the RWGS reaction over $Ni_{12}P_5$ /SiO_2 using the same long-term conditions, wherein 99.8% of its initial CO production rate, >99.5% CO selectivity, and high $Ni_{12}P_5$ dispersion on the silica support were maintained.[25] These results suggest that Ni is stabilized by the presence of P within the Ni ensemble—in the form of $Ni_{12}P_5$—to resist sintering and maintain CO activity and selectivity at a temperature of 563 K with light exposure. The effect of P content on the temperature reached by photo-induced local heating requires further probing.

Further elucidating the influence of P within the Ni ensemble, an earlier study by Layman and Bussell reported infrared (IR) spectroscopic investigations of the surface chemistry of 20 wt% Ni/SiO_2 and Ni_2P/SiO_2 in a CO atmosphere.[27] In the case of Ni/SiO_2, IR spectra collected at 298 K yielded two weak peaks corresponding to CO adsorbed onto Ni^0 bridge sites, and one strong peak corresponding to CO bonded to Ni atop sites.[27] Additionally, a shoulder at 2056 cm^{-1} was assigned to adsorbed nickel tetracarbonyl ($Ni(CO_4)$).[27] In comparison, the spectrum for Ni_2P/SiO_2 revealed strong suppression of the vibrational modes of both the bridge-bonded CO and the $Ni(CO_4)$ adsorption.[27] The culmination of these results underlies the stabilizing and selectivity-enhancing role of P: hinderance of Ni bridge bonding sites and $Ni(CO_4)$ formation promotes reaction pathways favored by RWGS over methanation.[22,25,27]

In this work, the degree to which P is beneficial to the Ni ensemble as a CO-selective RWGS catalyst was investigated by studying Ni_xP_y phases with different P/Ni molar ratios (e.g., 0.5, 0.42, and 0.33 for Ni_2P, $Ni_{12}P_5$, and Ni_3P, respectively). To gain insight on the role of the Ni_xP_y-support interface in activity and selectivity determination, two metal oxide supports (SiO_2 and TiO_2) were compared for the same Ni_xP_y phases.

1.6 Non-reducible Metal Oxide Support: Silica

Amorphous silica (SiO_2) is a non-reducible oxide with a high surface area (100–400 m^2/g) that is widely used as a support for catalytically active NPs.[9,27–31] Its intrinsic resistance to changing oxidation states at the Si cation center makes it unlikely to give up a lattice oxygen; stabilizing the two free electrons left behind by an extracted O would be too energetically costly.[32,33] Moreover, amorphous SiO_2 has a wide bandgap (ca. 8-11 eV) corresponding to poor light absorption.[34,35] As a result, SiO_2 is relatively inert in CO_2 hydrogenation reactions, including photocatalyzed RWGS.[32,33] Despite this, the SiO_2 support influences the size, stability, and spatial distribution of NPs during catalyst synthesis and reactions, ultimately impacting the collective catalytic properties.[16,17,36]

In this project, amorphous SiO_2 was used to support Ni_xP_y NPs to probe for trends in catalytic properties over P/Ni molar ratio in the photocatalyzed RWGS reaction. The stabilizing role of the support minimized particle growth during synthesis and catalysis, which helped keep the Ni_xP_y NPs small. The same synthesis method, loading (2.5 wt% Ni_xP_y), and reaction conditions were used for all Ni_xP_y catalysts. By using the relatively inert SiO_2 support, CO_2 hydrogenation was catalyzed exclusively by the Ni_xP_y particles, allowing for conclusions to be drawn about selectivity and activity patterns among different Ni ensemble geometries, electronic properties, and P/Ni molar ratios. The study was then replicated using a reducible oxide support (TiO_2) to further probe the role of the support and Ni_xP_y-support interface and compare trends of P/Ni molar ratio dependence.

1.7 Reducible Oxide Support Materials

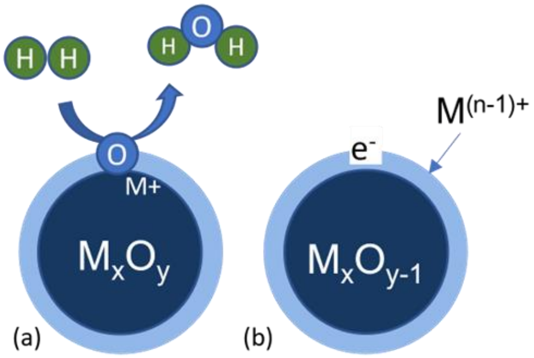

Figure 6. Schematic of (a) OV formation on a reducible oxide surface and (b) metal cation stabilization of the OV. Figure adapted from ref [38] with permission. Copyright 2018 American Chemical Society.

Reducible oxides are a class of materials that can relatively easily exchange oxygen with chemical species by stabilizing the cation (and electrons) left upon formation of oxygen vacancies.[32,36] Characteristically, the metal cation center (M^+) has its conduction band (CB) close enough to its valence band (VB) to enable redistribution of electrons; one of the excess electrons in the vacancy can transfer to the low-lying d orbital of the CB ($M^{(n-1)+}$).[32,37,38] The intrinsic ability to cycle between oxidation states ($M^+ \leftrightarrow M^{(n-1)+}$) at the cation center allows the reducible oxide to participate in the exchange of oxygen with reactants in heterogeneous catalysis (Figure 6).[32,36] As such, this class of materials has applications as both a catalyst and a catalytically active support for the RWGS reaction.

The two most relevant outcomes of using a reducible oxide as a RWGS catalyst support are 1) tunable electronic properties can modify optical properties to increase the photothermal effect, and 2) newly formed OVs can act as additional active sites for CO_2 adsorption, with implications on activity and selectivity. Expanding on the first outcome, the generation of surface oxygen vacancies (OVs) in reducible oxides has been previously demonstrated to darken the color and increase absorbance.[32,37,39–41] The increased absorbance is owed to a mid-gap defect state below the CB resulting from a newly generated OV, narrowing the effective bandgap (Figure 7).[32,37,42] In turn, electrons can be excited to the CB more easily under irradiation, resulting in improved photoconversion efficiency and increased local temperatures through non-radiative relaxation.[20,37,40,41,43]

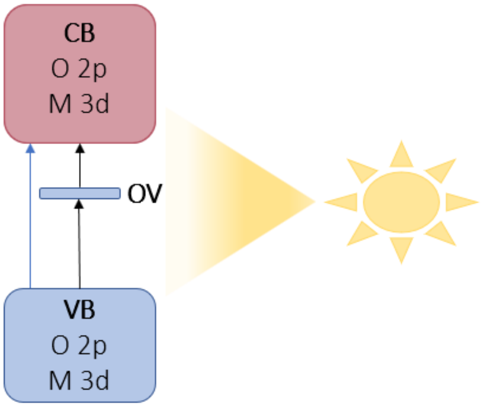

Figure 7. Diagram of a reducible oxide band structure with OV under irradiation. Adapted with permission from ref [41]. Copyright 2021 American Chemical Society.

In addition to enhancing light harvesting abilities and local heat generation, the OVs serve as CO_2 adsorption sites during the RWGS reaction.[32,37,43] Demonstrating this, Qi et al. carried out CO_2 temperature-programmed desorption (TPD-CO_2) studies to compare oxygen-deficient vs. stoichiometric indium oxide (In_2O_{3-x} vs. In_2O_3), in which the CO_2 adsorption decreased from 0.095 to 0.012 mmol g^{-1}, corresponding to a commensurate decrease in active site density for the vacancy-free In_2O_3.[43] Similarly, Kattel et al. performed density functional theory (DFT) calculations of the CO_2 binding energy (BE) on Pt/TiO_2 with and without interfacial OVs wherein their presence enhanced BE(CO_2) by more than 0.32 eV.[44] These results underlie the role of surface OVs in stabilizing CO_2 adsorption sites, which corresponds to anticipated enhancement in CO_2 hydrogenation activity.

1.7.1 Titania

Titania (TiO_2) is a semiconductor and reducible oxide with demonstrated CO_2 hydrogenation properties; its stability, earth abundance, and low toxicity make it an excellent candidate for scalable catalyst systems.[39,45–48] Unlike SiO_2, the reducibility of TiO_2 enables hydrogen spillover from a metal NP (e.g., Pt) onto the support where it produces Ti^{3+} cations and surface H^+ protons (Figure 8).[49] From this H-spillover arises a pathway for TiO_2 to participate directly in CO_2 hydrogenation via the RWGS reaction.

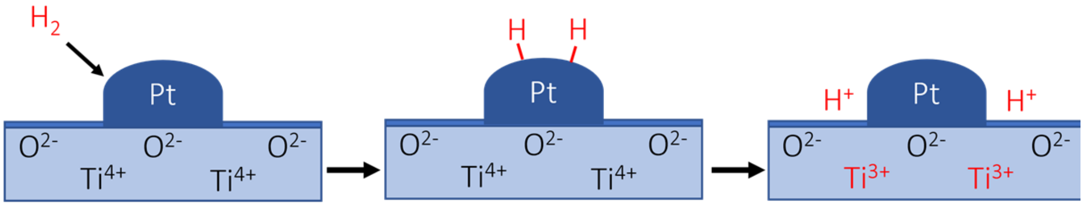

Figure 8. Schematic of H_2 adsorption on Pt and H spillover onto TiO_2 support, yielding surface protons and reduced metal cation centers (H^+ and Ti^{3+}). Adapted with permission from ref [49] Copyright 2012 ACS American Chemical Society.

TiO_2 has a wide intrinsic bandgap (3.1–3.4 eV), which can be effectively narrowed via reduction to form sub-stoichiometric TiO_{2-x} with OVs.[39,40,45,47] As described in the previous section, OVs serve the dual purpose of forming 1) mid-gap defect states within the bandgap to increase light absorption properties, and 2) new sites for reactant adsorption during CO_2 hydrogenation.[37,40,43,47,48,50] The formation of OVs yields an electron–hole pair stabilized by the Ti^{4+} cation center; the degree to which TiO_2 is oxygen-deficient determines the number of active sites available for CO_2 adsorption (Figure 9). Moreover, an OV formed at the interface of a supported NP (i.e., Pt-TiO_{2-x}) leads to greater CO_2 adsorption stability than either Pt or TiO_{2-x} as described by Kattel et al. As such, it is hypothesized that there will be a synergistic effect between Ni_xP_y and the support for Ni_xP_y/TiO_2 compared to Ni_xP_y/SiO_2.

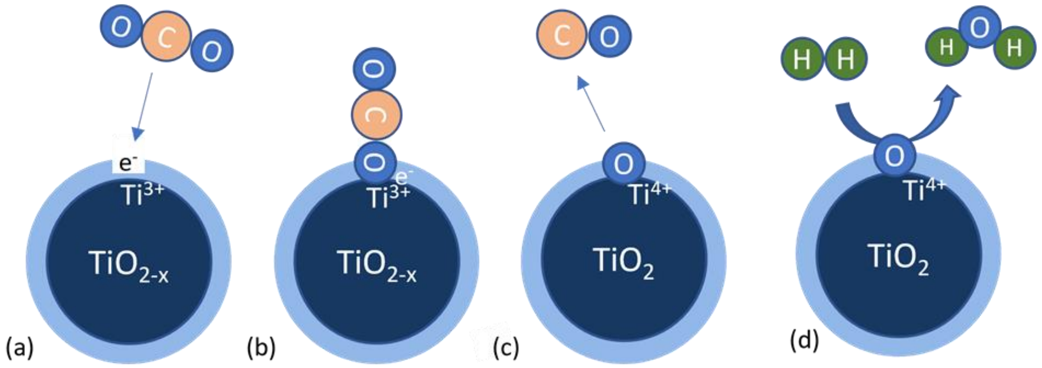

Figure 9. Schematic of (a) CO_2 adsorption on a stabilized OV, (b) chemical activation of adsorbate, (c) CO product desorption and refilled vacancy, and (d) H_2 reduction of the TiO_2 surface to form water and a new OV. Figure adapted from ref [38] with permission. Copyright 2018 American Chemical Society.

1.8 Thesis Outline and Research Aims

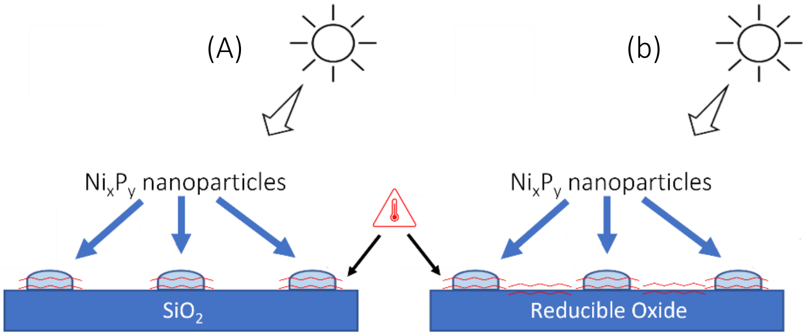

Figure 10. Hypothesized photothermal contributions of A) SiO_2-supported Ni_xP_y and B) reducible oxide-supported $NixP_y$.

The central goal of this thesis project was to gain insight on the role of the support and the Ni_xP_y-support interface in determining the photothermal catalytic properties for the RWGS reaction.

It was hypothesized that the proposed hybrid Ni_xP_y/reducible oxide design strategy would increase photocatalytic activity by generating new active sites for CO_2 adsorption and H_2 dissociation while also facilitating high local temperatures at the periphery of the Ni_xP_y-support interface (Figure 10). To test this, CO_2 HYD studies were conducted first using SiO_2 as a relatively inert support to probe the effect of Ni_xP_y phase (and hence, P/Ni molar ratio) on the CO_2 conversion and CO selectivity (Figure 11a). Next, TiO_2 was used as a reducible oxide support (e.g., Ni_xP_y/TiO_2) to elucidate the role of the support and Ni_xP_y-support interface in determining the photothermal catalytic activity (Figure 11b). If CO_2 adsorbed on OVs near the Ni_xP_y NPs was met with spill-over H atoms from dissociative H_2 adsorption on the NPs, it was hypothesized that the cumulative catalytic activity would be greater than the sum of its parts. Comparing two types of support materials further elucidated the role of photothermal enhancement on CO_2 HYD and CO selectivity.

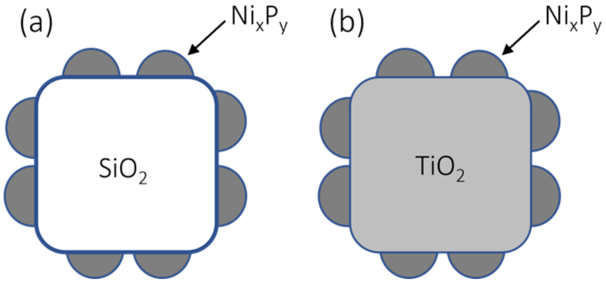

Figure 11. Proposed catalysts (a) Ni_xP_y/SiO_2 and (b) Ni_xP_y/reducible oxide with TiO_2 as an example.

X-ray diffraction (XRD) and inductively coupled plasma-optical emission spectroscopy (ICP-OES) were used to characterize crystalline phases and composition, respectively. Raman thermometry was used to probe the photothermal effect of supported Ni_xP_y. Morphology was characterized by scanning electron microscopy (SEM). Absorbance spectra were obtained by ultraviolet-visible-near infrared spectroscopy (UV-Vis-NIR). Chemisorption (CO) and physisorption (N_2) techniques were used to quantify active site density and surface area, respectively. CO_2 HYD reactions were monitored by gas chromatography with a flame ionization detector (GC-FID). Ultimately, the CO_2 conversion, CO selectivity, turnover frequency (TOF), apparent quantum yield (AQY), and light enhancement (light/dark) were the primary metrics used to compare performance of the different photothermal RWGS catalysts.

Chapter 2. Experimental Methods

2.1 Reagents

All reagents were used as received with exceptions of silica (SiO_2), titania (TiO_2), and the gases used for synthesis and CO_2 HYD reactions. SiO_2 (CAB-O-SIL, EH-5, CABOT, 380 m^2/g) was calcined in air for 3 h at 773 K and then stored in a 393 K oven. TiO_2 (Evonik, AEROXIDE, P25, 35-65 m^2/g) was calcined in air for 3 h at 673 K and then stored in a 393 K oven. Helium (Airgas, 99.999%), hydrogen (Airgas, 99.999%), and 10 mol% hydrogen in argon mixture (Airgas, 9.989/90.011 mol% H_2/Ar) gases were passed through in-line molecular sieve moisture (Alltech) and oxygen purification (OxiClear) traps. Carbon dioxide (Airgas, 99.999%) and 1 mol% oxygen in helium mixture (Airgas, 1.001/98.999 mol% O_2/He) gases were passed through an in-line molecular sieve moisture trap (Alltech). Solid reagents known to be hygroscopic were stored in a desiccator between uses.

2.2 Temperature-Programmed Reduction

Temperature-programmed reduction (TPR) was performed in a quartz U-tube heated by a furnace equipped with a temperature controller (Watlow Series 981). A known amount of catalyst precursor (200–600 mg) was loaded into the U-tube on a bed of quartz wool, and a greased glass adapter was placed on the tube inlet. The tube was connected to a gas manifold outfitted with mass flow controllers and gas cylinders (Figure 12). After a 30 min He (60 ml/min) degas treatment, H_2 was flowed (20–100 sccm) through the U-tube while heating to a desired temperature (673–923 K) at a rate of 5 K/min. The reduction was held at the setpoint temperature for 1–2 h. Following reduction and another 30 min He degas (60 sccm) while cooling to 298 K, 1 mol% O_2/He was flowed through the U-tube to passivate the catalyst by forming a thin oxide layer on the surface to increase stability and prevent a rapid oxidation event upon air exposure. Reduction conditions vary by catalyst composition and desired characteristics; see sections 2.3 and 2.4 detailed synthesis information.

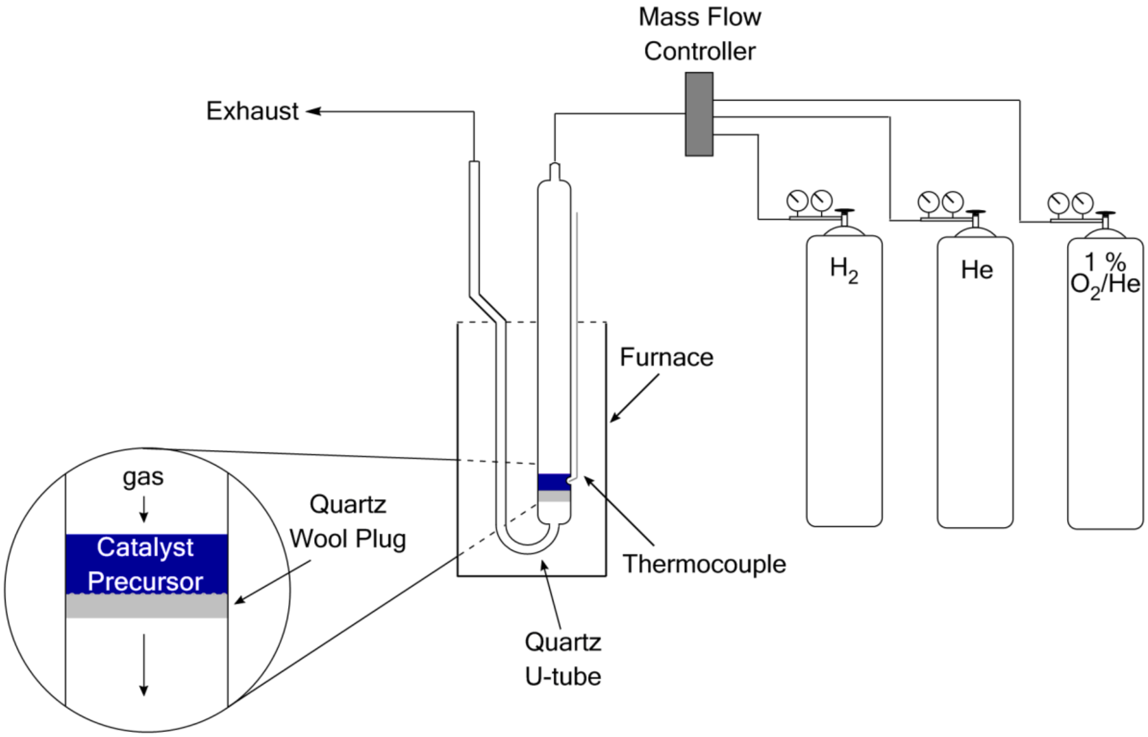

Figure 12. Diagram of temperature-controlled reduction apparatus with gas manifold

2.3 Ni_xP_y/SiO_2 Syntheses

2.3.1 Ni_xP_y/SiO_2 Precursor: Phosphate Method

To synthesize Ni_xP_y/SiO_2, a known amount of SiO_2 (Cabot EH-15) was measured out and placed in a beaker. To separate dry test tubes, nickel(II) nitrate hexahydrate ($Ni(NO_3)_2 \cdot 6H_2O$, Alfa Aesar, 99.9985%) and ammonium dihydrogen phosphate ($NH_4H_2PO_4$, Alfa Aesar, 98.0%) were added in the amounts needed to yield the nominal P/Ni ratio desired for a given synthesis (Table 1). Nanopure water was added to each test tube until both reagents were fully dissolved. Next, the aqueous $NH_4H_2PO_4$ was transferred dropwise to the $Ni(NO_3)_2 \cdot H_2O$ solution, yielding a translucent green impregnation solution. The impregnation solution was then added dropwise to the SiO_2 to the point of incipient wetness—drying at 343 K between additions as needed—until all solution was incorporated. The impregnated mixture was dried overnight at 343 K. The following day, the mixture was transferred to a ceramic crucible and calcined in air at 673 K for 3 h (5 K/min) to decompose the impregnated salts (Figure 13). The resulting cream-colored precursor was stored in a closed vial under ambient conditions. Ni/SiO_2 was found to have larger average crystallite size than the other Ni_xP_y/SiO_2 phases (discussed in Section 3.1). To control for the variable of size, Ni/SiO_2 was also synthesized without the calcination step, which resulted in smaller crystallites in the final product on the order of 2.5 wt% Ni_xP_y/SiO_2 for Ni_3P, $Ni_{12}P_5$, and Ni_2P. Characterization and CO_2 HYD reactions were carried out for both calcined and uncalcined Ni/SiO_2 (Ni/SiO_2-c and Ni/SiO_2-uc, respectively) to probe the effect of size. To achieve the target Ni_xP_y phases, the amounts of the Ni and P sources were varied to yield desired nominal molar ratios (Table 1).

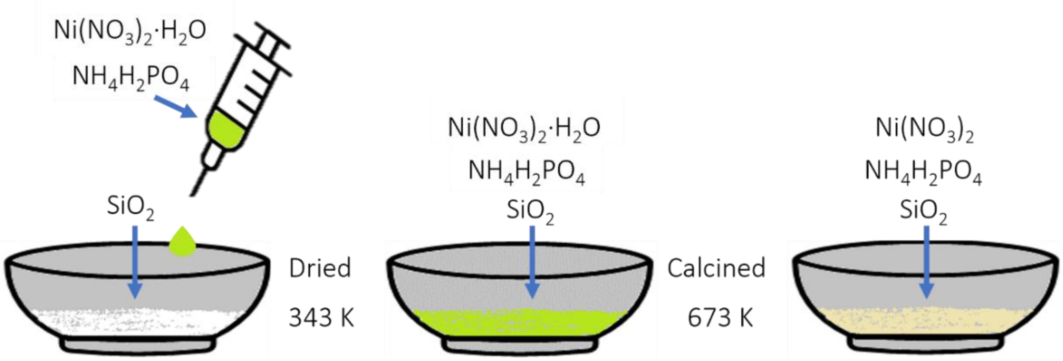

Figure 13. Schematic of precursor synthesis using incipient wetness impregnation

Table 1. Synthesis parameters for 2.5 wt% Ni_xP_y/SiO_2 catalysts

Final Catalyst	SiO_2 mass (g)	$Ni(NO_3)_2{\cdot}6H_2O$ mass (g)	$NH_4H_2PO_4$ mass (g)	P/Ni ratio
Ni/SiO_2	2.0012	0.2549	0	0
UC-Ni/SiO_2	2.0072	0.2541	0	0
Ni_3P/SiO_2	2.0019	0.2157	0.0298	0.35
$Ni_{12}P_5/SiO_2$	1.9999	0.2085	0.0412	0.5
Ni_2P/SiO_2	2.0011	0.2022	0.0804	1

2.3.2 Ni_xP_y/SiO_2: TPR

The calcined Ni_xP_y/SiO_2 precursor was reduced by TPR following the procedure in section 2.2 to yield a final product ranging from medium gray to black depending on the Ni_xP_y phase. For the reductant, H_2 was flowed over the sample (100 sccm) while heating to 923 K (5 K/min) and then the temperature was held for 1 h under continued flow (Figure 14).[51]

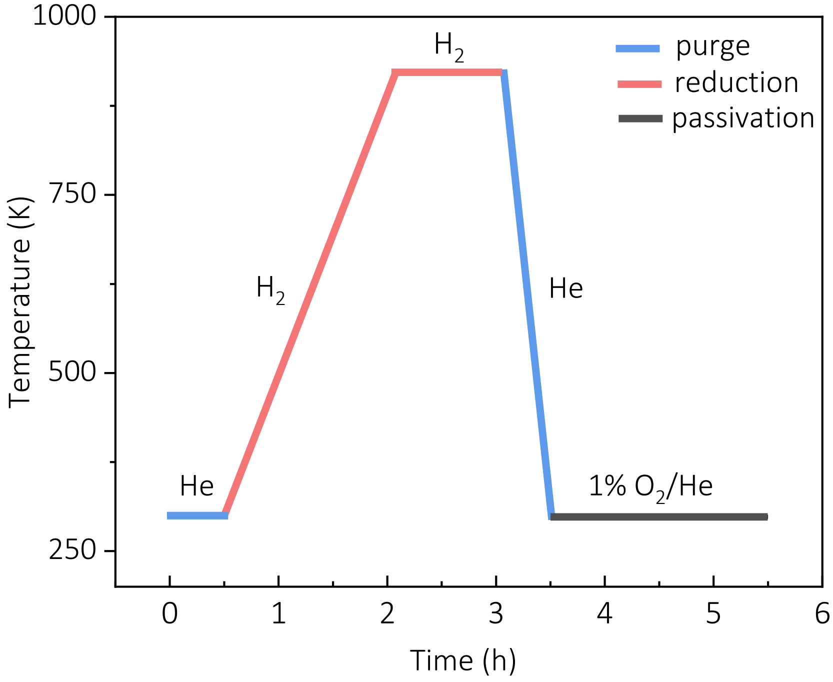

Figure 14. Heating profile of TPR used for calcined Ni_xP_y/SiO_2 precursors.

In addition to being affected by calcination, the crystallite size was also affected by reduction temperature. To synthesize Ni/SiO_2 nanoparticles on the order of the other Ni_xP_y/SiO_2 phases, the uncalcined Ni/SiO_2 precursor was reduced at 673 K instead of 923 K (Figure 15).

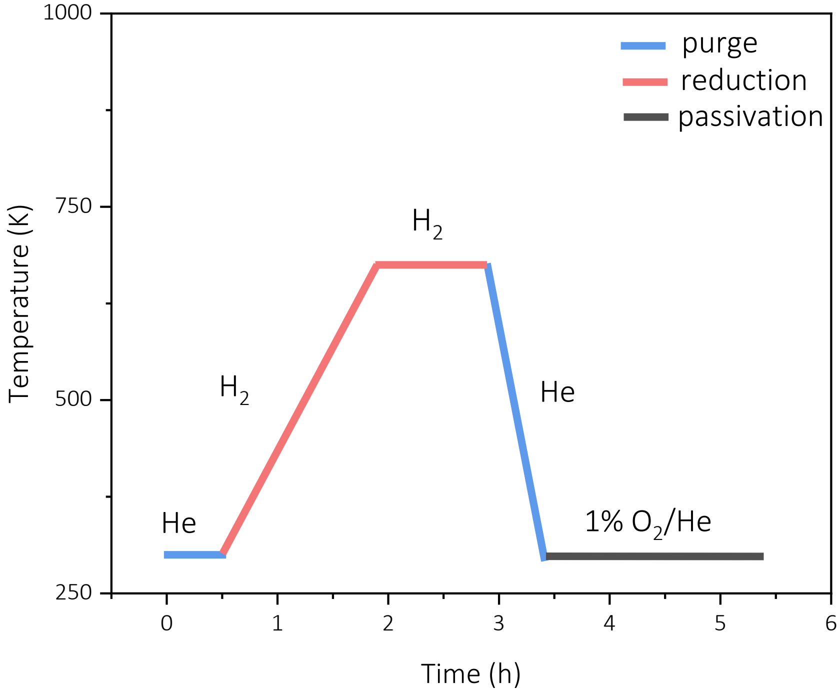

Figure 15. Heating profile of TPR used for uncalcined Ni/SiO_2 precursors.

2.4 Ni_xP_y/TiO_2 Syntheses

2.4.1 Ni_xP_y/TiO_2 Precursor: Triphenyl Phosphine (TPP) Method

To synthesize Ni_xP_y/TiO_2, a known amount of TiO_2 (Evonik, AEROXIDE, P25, 35-65 m^2/g) was measured out and placed in a beaker. To a dry test tube, nickel (II) acetylacetonate ($C_{10}H_{14}NiO_4$, Alfa Aesar, 95%) and triphenyl phosphine (TPP, $C_{18}H_{15}P$, Alfa Aesar 99%) were added (Table 2). Acetone (C_3H_6O, Sigma Aldrich, HPLC grade) was added to the test tube along with a stir bar. The mixture was placed in a 323 K water bath and stirred for 3–4 h until fully dissolved. Next, the impregnation solution was added slowly to the TiO_2 powder while stirring. The impregnated TiO_2

was dried overnight in a fume hood and then ground with a mortar and pestle to a fine powder. The Ni_xP_y/TiO_2 precursor was stored in a closed vial under ambient condition. To achieve the target Ni_xP_y phases, the ratio of the Ni and P sources were varied to yield desired nominal P/Ni molar ratios (Table 2).

Table 2. Synthesis parameters for 2.5 wt% Ni_xP_y/TiO_2 catalysts

Final Catalyst	TiO_2 mass (g)	Acetone volume (mL)	$C_{10}H_{14}NiO_4$ mass (g)	$C_{18}H_{15}P$ mass (g)	P/Ni ratio
$Ni_{12}P_5/TiO_2$	2.0036	20	0.2110	0.1723	0.8
Ni_2P/TiO_2	2.0008	20	0.2048	1.0389	5

2.4.2 NixPy/TiO2: TPR

The Ni_xP_y/TiO_2 precursor was reduced by TPR following the procedure in section 2.2 to yield a final product ranging from dark gray to black, depending on loading and Ni_xP_y phase. During the reduction, H_2 was flowed over the sample (100 sccm) while heating to 673 K (5 K/min) and then the temperature was held for 2 h under continued flow (Figure 16).[51]

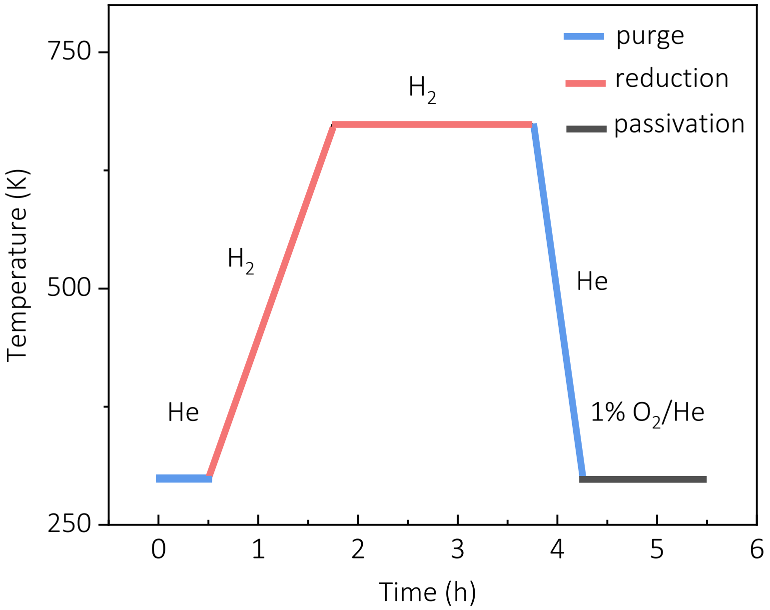

Figure 16. Heating profile of temperature-programmed reduction of Ni_xP_y/TiO_2 precursors.

2.5 Characterization: Material Properties

2.5.1 X-ray Diffraction

$$d = \frac{\mathrm{K}\,\lambda}{\beta\,\cos\theta}$$

Equation 3. Scherrer Equation

Synthesized precursors and reduced catalysts were characterized by x-ray diffraction (XRD) to identify phase(s) and to determine average crystallite sizes. Smartlab Studio II software was used to view the patterns, identify phases, and calculate the average crystallite sizes. The software computes the domain size from the coherent diffraction associated with each peak using the Scherrer equation (Equation 3), where d is the coherent diffraction domain size, K is the shape factor (K = 0.9 unless otherwise stated), λ is the wavelength of the X-ray source, and β is the reflection width (2θ), and θ is the Bragg angle in radians.[52] The domain sizes corresponding to the strongest three peaks were averaged to determine the average crystallite size of the Ni_xP_y phases. XRD phase identifications were made before proceeding with characterization and photoreactor studies. Smartlab II reference patterns are accompanied by their respective powder diffraction file card numbers: Ni (card no. 00-004-0850), Ni_3P (card no. 00-034-0501), $Ni_{12}P_5$ (card no. 03-065-1623), and Ni_2P (card no. 03-065-1989).[53] The SiO_2 support contributes a broad background to the XRD pattern due to its amorphous structure. Due to the weaker diffraction signal produced by low loadings (i.e., 2.5 wt%) of Ni_xP_y on amorphous SiO_2, 7.5-15 wt% Ni_xP_y/SiO_2 synthesized under equivalent conditions were analyzed by XRD to corroborate the phase identities of their 2.5 wt% counterparts. Furthermore, the 2.5 wt% Ni_xP_y crystallite size was too small to be computed by XRD; instead, transmission electron microscopy (TEM) will be needed to determine crystallite sizes in future work.

2.5.2 Energy Dispersive X-ray Spectroscopy

The P/Ni molar ratios for Ni_xP_y catalysts (supported and unsupported) were determined by energy dispersive X-ray spectroscopy (EDS) using a 150 mm^2 Oxford X-Max x-ray detector. Two electron microscopes were used to generate characteristic X-rays from the specimens: 1) a JEOL JSM-7200F Schottky field emission (FE) scanning electron microscope (SEM), and 2) a Tescan Vega 3 thermionic SEM. The FESEM and thermionic SEM used take-off angles of 29.0° and 35.0°, respectively, for the EDS measurements. Specimens were mounted on an isopropyl-based graphite suspension paint (PELCO, 20 ± 0.2 wt% colloidal graphite) by swiping a small amount of paint onto an aluminum stub and dispersing a minimal amount of the catalyst onto the paint while it was still wet. Excess powder was blown off with a rubber bulb once the paint had dried. When carbon contamination was evident from the electron micrograph viewer, plasma cleaning of the specimen was completed using an EZ-KLEEN remote plasma cleaner (15 W for 6 min).

EDS spectra collected on the FESEM were acquired on uncoated samples using an accelerating voltage of 5 kV, which is sufficient to provide the overvoltage necessary for at least one excitation energy of the present elements (Ni: Lα 0.851 keV, P: Kα 2.013 keV, Si: Kα 1.740 keV, Ti Lα 0.452 keV, and O: Kα 0.523 keV).[24] The FESEM beam was calibrated for EDS with both copper (Cu) manganese (Mn) K-line series. EDS spectra collected on the thermionic SEM were acquired on carbon-coated samples using an accelerating voltage of 15 kV. Samples were coated with 30-40 nm of carbon using a high-vacuum turbo carbon coater (Cressington 208C) using a high-resolution film thickness monitor (Cressington MTM-10).

EDS data were analyzed using factory standards built into AZtec 4.4 analysis software (Oxford Instruments Nanotechnology Tools Limited). The carbon coating thickness, when applicable, was considered during quantification. Results for atomic percentage (at%) and weight percentage (wt%) were normalized, and elements known to be present but not of interest (i.e., carbon and aluminum) were deconvoluted from the wt% and at% calculations.

2.5.3 Chemisorption

2.5.3.2 Pulse CO Chemisorption

The number of active sites for CO_2 hydrogenation were estimated by pulse CO chemisorption (Figure 17). Specifically, a known amount of CO (10 mol% CO/He, UN1956) was flowed over the catalyst in successive pulses at a constant temperature while monitoring the effluent composition by thermal conductivity detection (TCD). The pulses were repeated until the CO adsorption capacity of the sample had been reached as indicated by no detected change in CO concentration. The CO chemisorption capacity in μmol/g_{cat} was determined for each catalyst as an estimation of the number of active sites.[54]

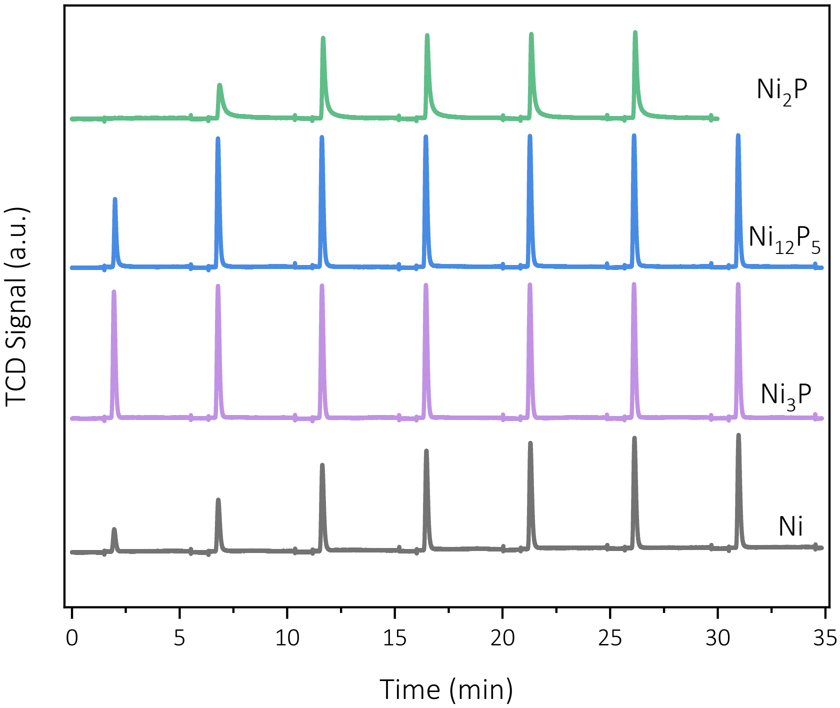

Figure 17. Typical CO pulse chemisorption profiles for 2.5 wt% Ni, Ni_3P, $Ni_{12}P_5$, and Ni_2P on SiO_2.

2.5.3.2 Temperature-Programmed Desorption

After pulse chemisorption was completed, temperature-programmed desorption (TPD) was performed to determine the type(s) of binding sites present, which corresponds to the number of peaks (Figure 18). In detail, the temperature of the sample was increased from 273 to 673 K (30 K/min) and the change in gas composition between sample and reference lines was monitored by TCD to determine the temperature(s) at which CO desorbs from the surface.[54]

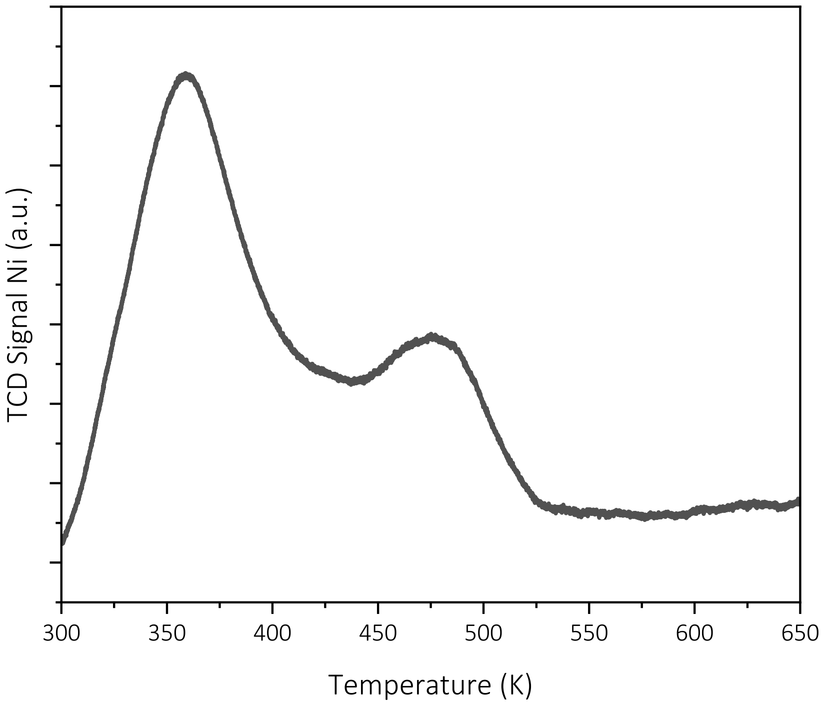

Figure 18. Typical CO-TPD profile of 2.5 wt% Ni/SiO_2.

2.5.4 Physisorption: BET Analysis

2.5.4.1 Single-Point BET Analysis

Following the CO chemisorption and TPD experiments, the specific surface area was determined from a single-point BET surface area measurement. To this aim, the sample tube was immersed in a liquid nitrogen (LN_2) bath while 30% N_2/He flowed over it. At low temperatures (ca. 77 K), N_2 adsorbs to the surface forming a monolayer of N_2. While monitoring composition by TCD, the sample tube is moved to a room-temperature water bath to warm the sample, causing rapid desorption of the N_2. The amount of adsorbed nitrogen was determined by the area of the desorption peak.[54] The single-point analysis was calibrated from a LN_2 headspace injection.

2.5.4.2 Multi-Point BET Analysis

Multi-point BET surface area analyses were performed on a Micromeritics ASAP 2020 Porosimeter using nitrogen (N_2, UN1066, 99.9999%) as the adsorbate. A known amount of sample (≥ 100 mg) in a pre-weighed sample tube was degassed with helium (He, Airgas, UHP) for 2–24 h. The mass of the degassed sample in the sealed sample tube was then determined and then the tube was secured on the analysis port and engulfed in an insulating sleeve. Next, the sample tube was placed inside a liquid nitrogen bath (LN_2, industrial grade) to lower the temperature to 77 K. Specific surface area was determined by Brunauer-Emmett-Teller (BET) analysis via isothermal N_2 physisorption at 77 K as the pressure increased from 1 kPa to 100 kPa using the adsorption isotherm (Figure 19). The pressure was then lowered to desorb the N_2, yielding a desorption isotherm.

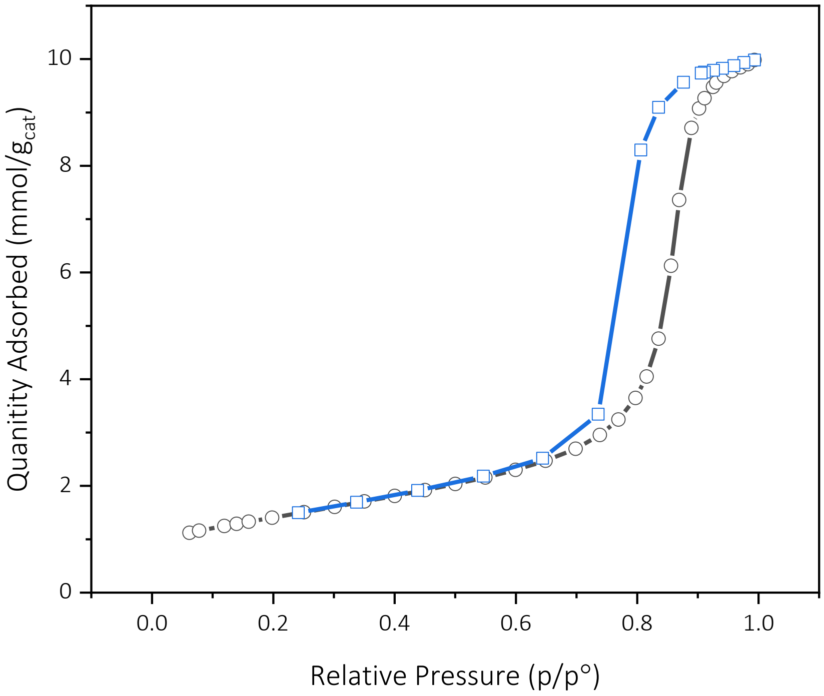

Figure 19. Typical BET N_2 adsorption isotherm at 77 K for of In_2O_3 nanocrystals. The adsorption and desorption isotherms are shown in black and blue, respectively.

2.5.5 Diffuse Reflectance Ultraviolet-Visible-Near Infrared Spectroscopy

Diffuse reflectance ultraviolet-visible-near infrared spectroscopy (DR-UV-Vis-NIR) spectra were obtained using a Jasco V-670 UV-Vis-NIR spectrophotometer outfitted with a 60 mm diffuse reflectance integrating sphere. Powder samples were ground using mortar and pestle to homogenize, then loaded into a sample cell (Jasco, PSH-002, 16x16 mm). The instrument was auto zeroed using a barium sulfate ($BaSO_4$) reflectance standard. Spectra were acquired over a range of 190 to 2500 nm (400 nm/min) using monochromator bandwidths of 5.0 and 20.0 nm for UV/Vis and NIR, respectively. Dual light sources, deuterium (190-350 nm) and halogen (350-3200 nm) lamps, were used with a source-changeover occurring at 330 nm. A discontinuity appeared at 900 nm in the raw spectra as an artifact of a grating changeover at 900 nm. To correct this, the difference in y-values between 899 and 900 nm was subtracted from the absorbance values of 250–899 nm (Figure 20).

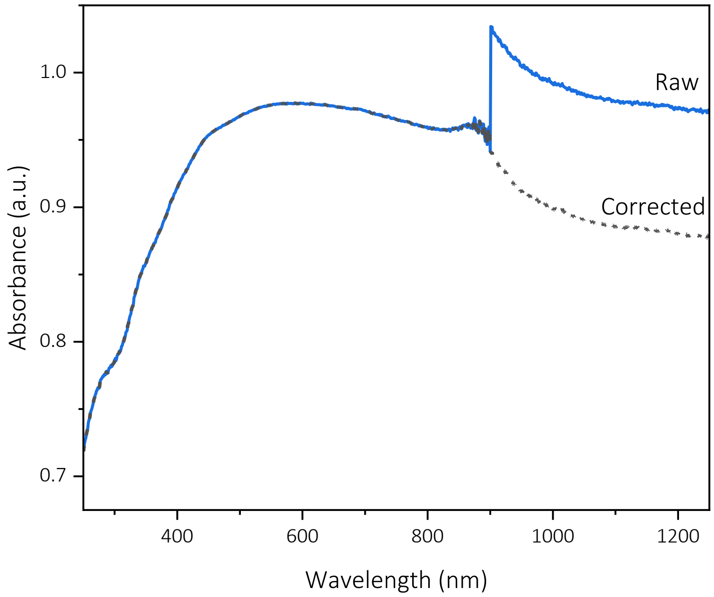

Figure 20. Absorbance spectrum of 2.5 wt% Ni/SiO_2 shown with and without artifact correction.

2.5.6 Raman Spectroscopy

Equation 4: Laser Spot Diameter

D = 1.22 λ / NA

Equation 5: Spatial Resolution

R_s = 0.61 λ / NA

D is the laser spot diameter, R_s the spatial resolution, λ is the laser wavelength, and NA is the numerical aperture; all units are in µm.

Raman spectra were obtained using a Renishaw Invia™ Qontor® confocal Raman microscope equipped with a silicon (Si) internal standard and a 50 mW 532 nm laser. Raman scattering was detected by a Peltier-cooled charge coupled device (CCD) using 1800 l/mm diffraction grating. A 50xL objective lens with a numerical aperture (NA) of 0.5 was used, yielding a theoretical diffraction-limited spot size of 1.3 µm and a spatial resolution of 0.65 µm (equations 4 and 5, respectively).[55]

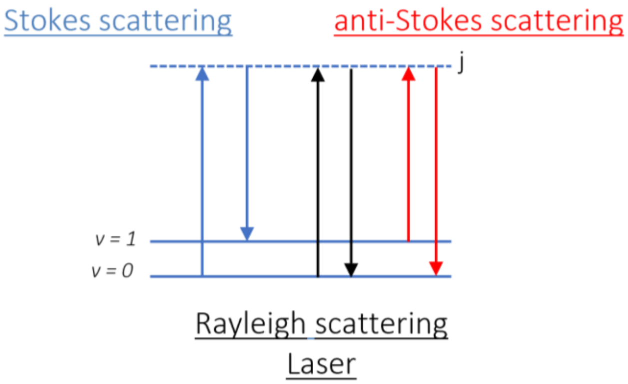

Figure 21. Energy diagram of the states involved in Stokes, Rayleigh, and anti-Stokes scattering.

Raman scattering occurs when an incident photon inelastically interacts with a chemical bond and gains or loses energy; the difference between the incident and scattered photon energy gives rise to the Raman shift peak.[55,56] In this work, the decreased energy of the incident photons from Stokes scattering—arising from the interaction between the incident photons and ground-state electrons—was detected (Figure 21). As such, the Stokes Raman shift is negatively temperature-dependent in two important ways: 1) thermal relaxation of a bond (i.e., lower frequency) decreases the energy transferred to the incident photon (i.e., smaller Raman shift) and 2) increased temperatures excite electrons and lower the ground-state population (i.e., lower Stokes intensity).[55,57] To probe the degree to which the Raman shift peaks of TiO_2 are affected by temperature, a thermal stage was employed to acquire spectra at different temperatures. Spectra were acquired at 50 K intervals over a temperature range of 298–523 K in an inert atmosphere (Ar, Airgas, 99.999%, 5 mL/min).

2.5.7 Raman Thermometry

Equation 6: Raman Local Temperature

$$T = \frac{\omega(\mathrm{T}) - \omega_0}{\chi}$$

T is the temperature in K, ω_0 *is the Raman shift of the phonon mode at 0 K in cm*$^{-1}$*,* $\omega(\mathrm{T})$ *is the measured Raman shift in cm*$^{-1}$*, and* χ *is the temperature cefficient in cm*$^{-1}$*K*$^{-1}$*.*
Ref [56].

To probe the photothermal effect of the catalysts, Raman thermometry can be employed wherein the change in Raman shift for a given peak is correlated to the local temperature at the incident laser spot. To achieve this, a correlation coefficient must be determined via external heating of the sample.

Wang et al. conducted a temperature-dependent study on cubic In_2O_3 thin films wherein a thermal stage was used to obtain the Raman shift at a series of increasing temperatures. The temperature coefficient, χ, for each characteristic peak was determined as the slope of the measured Raman shift (cm^{-1}) vs. stage temperature (K). The linear data were also extrapolated to determine ω_0, the Raman shift at 0 K.[55] These values enable the estimation of the temperature achieved at the incident laser spot for each Raman active phonon mode (Equation 6).[55]

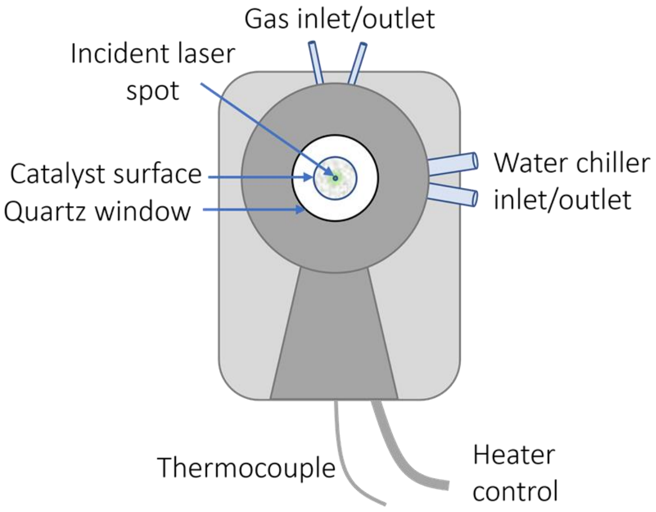

Figure 22. Diagram of thermal stage used temperature-dependent Raman studies.

In this work, a temperature-dependent Raman study was conducted for TiO_2 and $Ni_{12}P_5/TiO_2$ using a Linkam CCR1000 thermal stage (Figure 22). A gas handling system outfitted with a glass rotameter enabled in-situ use of argon (Ar, Airgas, 99.999%, 5 mL/min) within the Raman cell to establish an inert atmosphere. An S-type platinum/rhodium (Pt/Rh) thermocouple was used to control heating and a water circulator (Eheim Pro 4) was used to cool the bod of the thermal stage during heating. The sample was heated from 298–523 K (10 K/min), during which the temperature was held at 10–50 K increments and allowed to stabilize for 1 min before collecting a spectrum. The catalyst was loaded into the sample holder in a 1 mm-deep layer atop a bed of Cab-o-sil and pressed flat to replicate the loading parameters used in the CO_2 HYD reactions.

2.5.7 Photoluminescence

Photoluminescence spectra were acquired with a FluoroLog-3 Horiba spectrofluorometer equipped with dual monochromators (excitation and emission) and a charge-coupled device (CCD) detector. A slit width of 4.0 nm was used for the entrance and exit slits of both monochromators with a grating density of 1200 l/mm, and the signal was integrated for 0.1 s at 1 nm increments across the specified emission wavelengths.

Samples were analyzed as powder pressed between two quartz slides that were held in a custom-designed holder capable of rotating the sample at 30-degree intervals (Figure 23). To minimize specular reflection and scattered light that would otherwise contribute to the emission signal, different incident angles were tested to

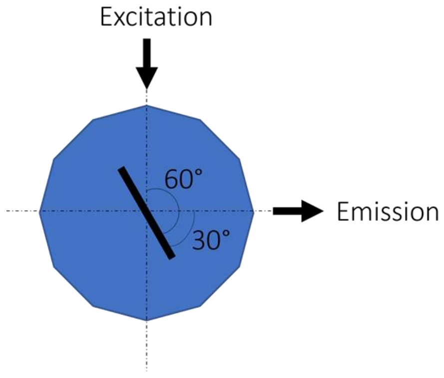

Figure 23. Top-view diagram of the dodecagon solid sample holder used for PL showing sample slide positioned 60° from excitation source and 30° from emission detection.

optimize the S/N. It was determined that S/N was optimized when the sample slide was positioned at 60 degrees from the excitation source (Figure 23). Data were processed in Origin 2021 software to compare spectra across samples. Data manipulation (e.g., baseline subtraction) was not performed unless otherwise specified.

2.5.8 Inductively Coupled Plasma Optical Emission Spectroscopy

P/Ni molar ratio and Ni_xP_y loading (wt%) were determined by inductively coupled plasma emission spectroscopy. Sample preparation and analysis was performed by AmTest Laboratories. Samples were prepared via acid digestion following EPA Method 3050B. Samples were analyzed with a Thermo Scientific iCAP 7000 Duo ICP-OES. A method blank was included throughout the preparatory and analytical processes. A minimum of 10% of the samples in the analytical batch was prepared and analyzed in duplicate and as a laboratory fortified matrix as part of a quality control protocol. An externally-sourced quality control solution and a lab reagent blank were analyzed after every tenth sample to validate continued performance.

2.5.9 Scanning Electron Microscopy

Catalyst morphology was determined using a JEOL JSM-7200F Schottky field emission (FE) SEM outfitted with two secondary electron detectors, a retractable backscattered electron detector (RBED), and an x-ray detector. Accelerating voltages ranging from 300 V to 5 kV were used to obtain images of uncoated specimens. The insulating and semi-conducting properties of SiO_2 and TiO_2, respectively, led to varying degrees of positive charge build-up on the surface of the catalyst. As a result, charge-mitigating strategies such as coating, stage bias, and through-the-lens mode were employed.

For high-resolution imaging purposes, a bias voltage of 2 kV was applied to the specimen stage to help secondary electrons escape the surface by repulsion and, more importantly, lower the effective voltage of the electron beam hitting the specimen. For example, a 3.1 kV applied accelerating voltage with a 2.0 kV negative stage voltage yields a 1.1 kV landing voltage. This method uses an upper secondary electron detector (UED)—also known as a through-the-lens (TTL) detector—to efficiently detect secondary electrons, minimize charging, and maintain the resolution benefits of a higher accelerating voltage.

2.6 Photothermal Catalytic Studies

2.6.1 Photothermal Batch Reactor Design

CO_2 HYD measurements were conducted using a stainless-steel batch reactor (Harrick, Raman High Temperature Reaction Chamber, HVC-MRA-5) outfitted with a fused SiO_2 (quartz) window. Sunlight was simulated by a 300 W xenon (Xe) arc lamp (Newport 6258). A water chiller (Neslab RTE111) was used to cool the external portion of the reactor during all CO_2 HYD studies.

Early experimental efforts resulted in hot spots on the catalyst surface; this was resolved by lowering the lamp height to negatively defocus the light over the catalyst surface.[58] To determine the lamp position with highest incident irradiance and no visible damage, a spectroradiometer (International Light Technologies, ILT960UVIR) and a series of CO_2 HYD studies were used. First, an irradiance measurement was taken with the lamp focused on the spectroradiometer sensor. Next, measurements were taken in 0.5 cm increments above and below the focal point. Lastly, CO_2 HYD reactions were conducted under irradiation at various lamp heights to defocus the light positively and negatively over the catalyst surface. From this, a 0.5 cm negative defocus was found to yield the highest activity and irradiance without causing surface damage.

To ensure reproducible lamp alignment, a custom alignment tool was made to fit securely over the reactor lid (Figure 24).[58] Material stability tests were conducted to ensure the aligner material, glycol-modified polyethylene terephthalate (PETG), could withstand reaction conditions. The tool was put into operating position and the catalyst was heated at 623 K under continuous irradiation for 1 h while monitoring the PETG temperature with a K-type thermocouple (Fluke 52 K/J).[58] The aligner was deemed stable as the PETG showed no sign of damage and its temperature did not exceed 333 K. It is crucial to maintain external water cooling during all heated CO_2 HYD reactions to ensure the aligner and reactor components are below their respective maximum operating temperatures.

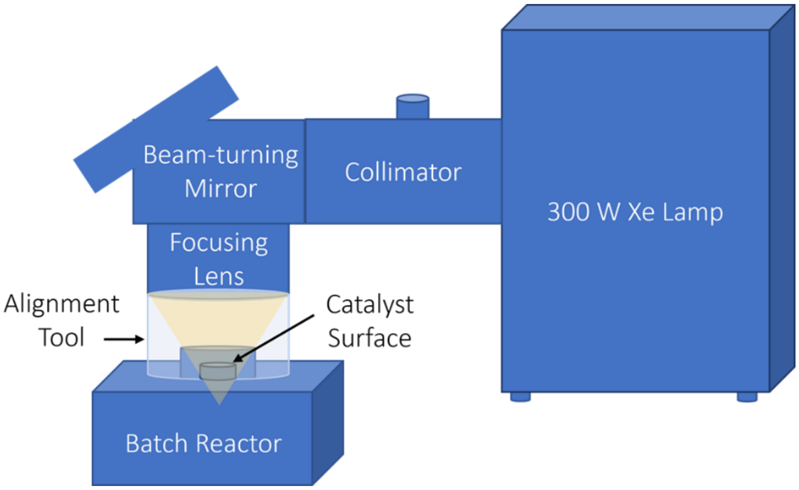

Figure 24. Diagram of the batch reactor setup used for photothermal CO2 HYD measurements.

The reactor was connected to a gas handling system equipped with helium (He, Airgas, 99.999%), H_2 (Airgas, 99.999%), and CO_2 (Airgas, 99.999%) gas tanks, each controlled by a mass flow controller (MFC, Brooks Smart Mass Flow) followed by a check valve (Figure 25)[58,59]

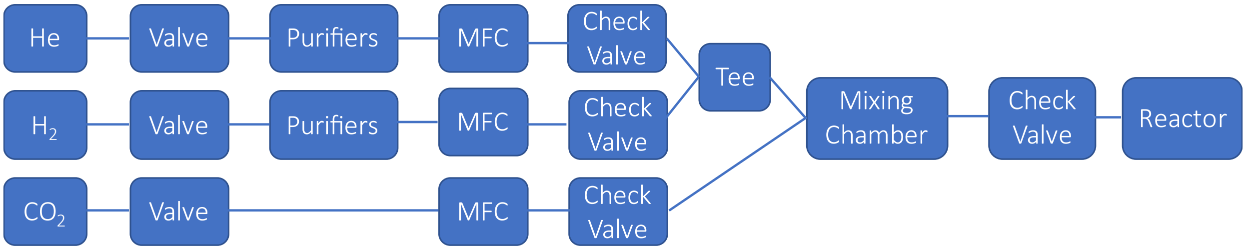

Figure 25. Schematic of gas handling system leading to the photoreactor.

In-line gas purifiers were used for He and H_2 gases to remove moisture (Alltech glass moisture trap) and oxygen (Oxiclear™ disposable gas purifier). The three MFCs enabled custom gas mixes (He:CO_2:H_2) of any ratio, and a mixing chamber with a final check valve were employed to ensure even mixing. The MFC setpoints were calibrated for each gas to determine the corresponding flow rates; a volumetric gas flow meter was used to measure the output for setpoints 1-25, and the data were fit with a linear regression (Figure 26).[54]

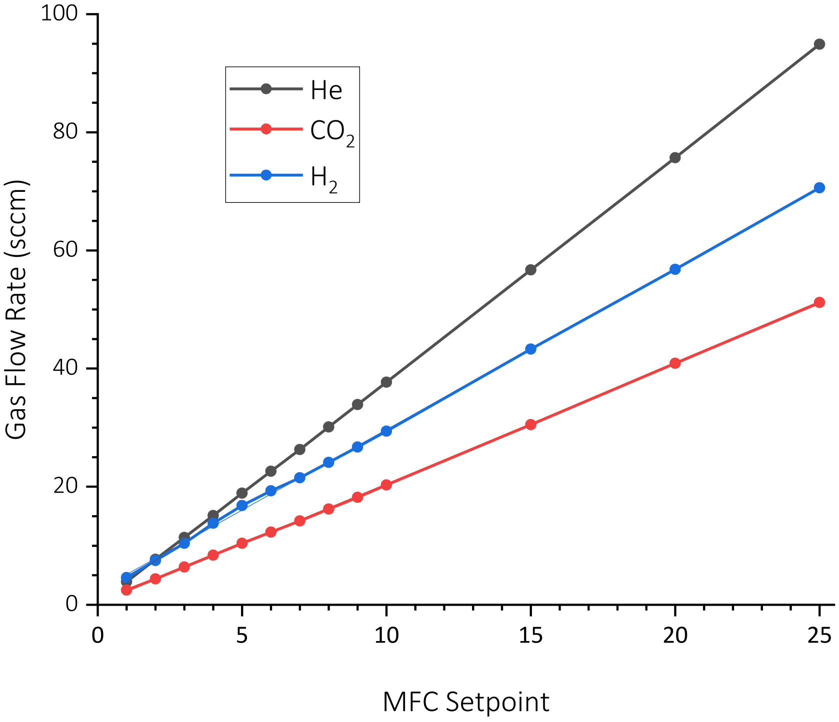

Figure 26. Linear fit of gas flow rates for the mass flow for He with fit parameters [m = 3.790 ± 0.006, b = -0.07 ± 0.06, R^2 = 0.9999], CO_2 with fit parameters [m = 2.031 ± 0.008, b = 0.18 ± 0.09, R^2 = 0.9998], and CO with fit parameters [m = 2.72 ± 0.02, b = 2.4 ± 0.2, R^2 = 0.9996].

The volume of the sample cup inside the reaction chamber exceeded the needs of this research project because the light absorption occurs only in the top 1–2 mm of the sample. To ensure full and complete exposure of the catalyst to light, the sample cup was filled most of the way up with SiO_2 (Cab-o-sil) and then pressed down with a 3D-printed tamping tool with a 1 mm offset to create a 1 mm deep well. A catalyst was then loaded into the well and tamped down so that it is flush with the edges of the sample cup (Figure 27). The amount of catalyst loaded in the reactor was determined by the difference in the masses of the catalyst vial before and after loading. While loading material into the sample cup, a barrier was used to prevent any powder from falling inside the reaction chamber; excess catalyst left on the barrier was recovered and returned to the sample vial before determining the final weight.

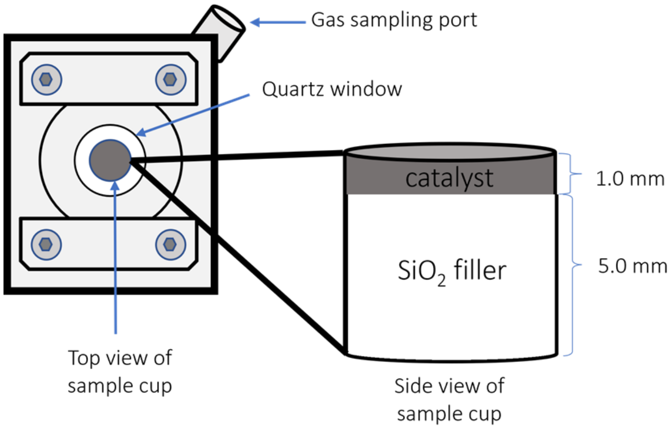

Figure 27. Diagram of the reactor chamber and a sideview of the sample cup with a 1 mm layer of catalyst atop a bed of SiO_2 filler.

2.6.2 Gas Chromatography Detector Response Calibration

The gas phase from the CO_2 hydrogenation reactions was analyzed by gas chromatography using tandem thermal conductivity and flame ionization detectors (TCD and FID, respectively). The exhaust from the TCD was mixed with hydrogen and reduced in a 653 K methanizer before being detected by flame ionization (Figure 28).

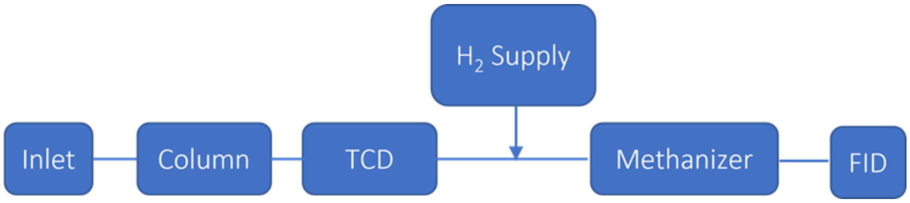

Figure 28. Box diagram of gas chromatography components.

Equation 7.

$$number\ of\ moles = \frac{PV}{RT}$$

Where P is pressure in atm, V is the volume injected in L, R is the gas constant in $L \cdot atm \cdot mol^{-1} \cdot K^{-1}$, and T is temperature in K.

Three commercially available gas standards were used to determine the FID response (mol/peak unit area) for CO, CH_4, and CO_2: 1) 1 mol% each CO, CH_4, CO_2, O_2, and H_2 balanced in N_2 (Supelco), 2) 7 mol% CO, 15 mol% CO_2, and 5% O_2 balanced in N_2 (Supelco), and 3) 100% CO_2 (Airgas, 99.9999%) (Figure 29). Due to the strong linearity, the response factor for CH_4 was based on the area of a single standard. Each analysis consisted of 100 µL of gas injected at room temperature (298 K) under atmospheric pressure (1 atm), from which the number moles of gas injected was calculated (Equation 7).

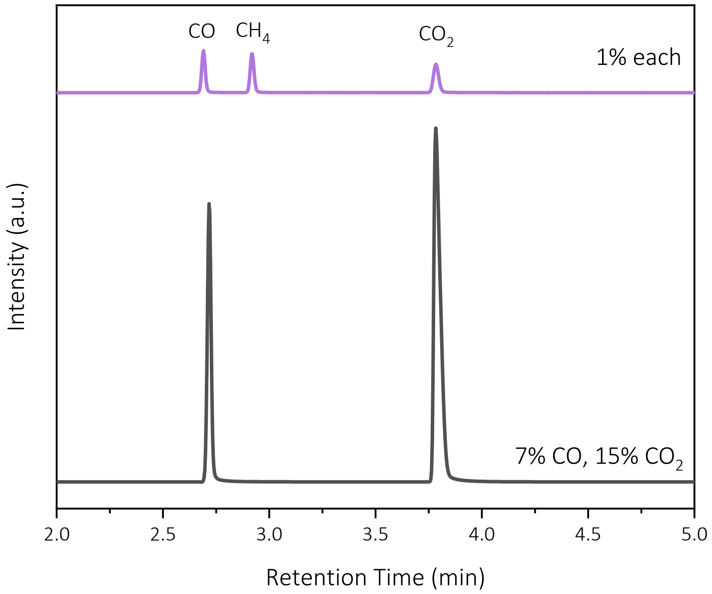

Figure 29. Typical GC-FID traces of C1 standards used for linear response factor calculations.

The peak area of each C1 component was then plotted against concentration, and a linear fit was used to obtain the slope (Figure 30). The FID response factor was then determined from the number of moles injected and the slope of the linear fit (Equation 8, Table 3).

Table 3. Calculated GC-FID response factors

Gas Molecule	Response Factor (mol/peak area)
CO	1.17×10^{-12}
CH_4	1.16×10^{-12}
CO_2	1.15×10^{-12}

Equation 8.

$$FID\ Response\ Factor = \frac{\frac{1}{m}}{100} * no.of\ moles$$

Where m is the slope of peak area vs. concentration (mol%) for each C1 component, yielding a response factor unit of mol/peak area.

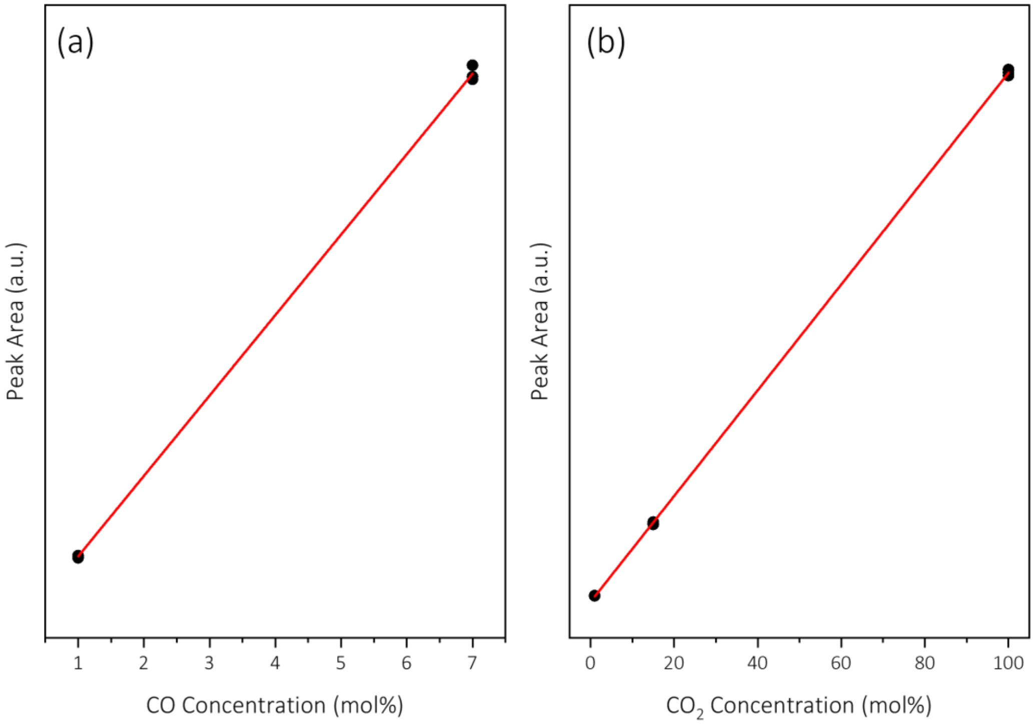

Figure 30. Linear fitting of average peak area versus gas concentration (mol%) for (a) CO with fit parameters [m = 36000 ± 300, $R^2 = 0.9998$] and (b) CO_2 with fit parameters [m = 35500 ± 100, $R^2 = 0.9999$] slope 34960. The average CH_4 peak area for 1 mol% CH_4 was 35000 ± 600 a.u., which was used in place of slope.

2.6.3 CO_2 Hydrogenation Reaction

The photothermal catalytic properties of each catalyst were evaluated for the RWGS reaction. Reactions were carried out in a 14 mL stainless-steel reaction chamber (Harrick, Raman High Temperature Reaction Chamber, HVC-MRA-5) outfitted with a type-K thermocouple, gas inlet/outlet ports, and a gas sampling port.

All reaction series were preceded by an activation step wherein the oxide layer formed on the Ni_xP_y nanoparticles during catalyst passivation was removed in-situ. The catalyst loading procedure is described in section 2.6.1. In brief, 5–15 mg of catalyst was loaded in the reactor sample cup on a layer of inert SiO_2 (Cab-o-sil). The reactor was then degassed with flowing He (30 mL/min) for 30 min at 298 K to displace oxygen. To activate a catalyst, the reactor was heated to 673 K (10 K/min) under flowing H_2 (30 mL/min) and then held at 673 K for 1 h under continued flow.

Following activation, a series of consecutive catalytic reactions were conducted without exposing the system to air. Before each reaction, reactants were flowed through the chamber in a 3:1 CO_2:H_2 ratio (30 mL/min total) for 15 min to displace reacted gas. Next, the reactor was sealed with 20 psi of backpressure and held for 15 min. Reactions were carried out for 15 min with and without irradiation at temperatures of 298–573 K in 50 K increments. After each reaction, 200 µL was drawn from the reactor, dispensed to purge the needle, and then 100 µL was drawn and injected into the GC.

2.6.4 CO_2 HYD Data Treatment

To assess catalytic performance, the catalyst mass, FID response factors, and the GC-FID areas for the peaks corresponding to CO, CH_4, and CO_2 were used in a series of calculations. First, the raw areas were multiplied by the FID response factor to determine the number of moles of each C1 component injected. From that, the number of moles of each component (e.g., CO, CH_4, and CO_2) within reactor after CO_2 HYD and the CO_2 conversion were calculated (Equations 9 and 10, respectively). Next, production rates and selectivity were calculated for CO and CH_4 for each reaction temperature in light and dark (Equations 11 and 12, respectively). Lastly, photoenhancement was determined by dividing the production rates in light and dark for a given temperature (Equation 13).

Equation 9.

$$moles_x\ in\ reactor\ (mol) = mol_x\ injected\ \times \frac{V_{reactor}}{V_{injected}}$$

Equation 10.

$$CO_2\ converted\ (\%)\ \frac{mol_{CO} +\ mol_{CH_4}}{mol_{CO} + mol_{CH_4} +\ mol_{CO_2}} \times 100$$

Equation 11. $production\ rate_x(mmol \cdot g_{cat}^{-1} \cdot h) = \frac{mol_x}{g_{cat} \times t/60}$

Where mol_x is in the number of moles of *x* in mmol, g_{cat} is the mass of catalyst in grams, and t is the reaction time in minutes.

Equation 12. $selectivity_x\ (\%) = \frac{production\ rate_x}{(production\ rate_{CO} + production\ rate_{CH_4})}$

Where *x* is the target product (i.e., CO).

Equation 13. $Photoenhancement_x = \frac{(production\ rate\ at\ T\ in\ light)_x}{(production\ rate\ at\ T\ in\ dark)_x}$

Where T is external reaction temperature in K.

Chapter 3. Results & Discussion

3.1 Catalyst Structure

The 2.5 wt% Ni_xP_y/SiO_2 catalysts were characterized by XRD to confirm synthesis of the target Ni_xP_y phases (Figure 31). The crystallite sizes were too small (<5 nm) to determine using the Scherrer equation for all phases except Ni/SiO_2-c, which had an average crystallite size of 13.9 nm (Table 4).

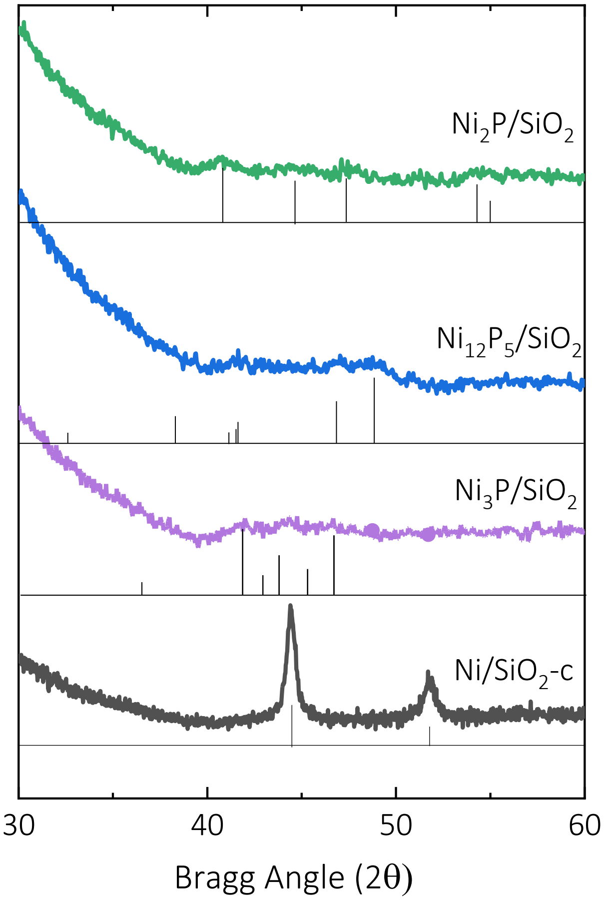

Figure 31. 2.5 wt% Ni-c, Ni_3P, $Ni_{12}P_5$, and Ni_2P on SiO_2 with stick reference patterns for Ni (card no. 00-004-0850), Ni_3P (card no. 00-034-0501), $Ni_{12}P_5$ (card no. 03-065-1623), and Ni_2P (card no. 03-065-1989).

Table 4. XRD determination of Ni_xP_y/SiO_2 average crystallite sizes.

Catalyst	Average Crystallite Size by XRD (nm)
Ni/SiO_2-c	13.9 ± 0.6
Ni_3P/SiO_2	<5
$Ni_{12}P_5/SiO_2$	<5
Ni_2P/SiO_2	<5

Ni/SiO_2 prepared without the calcination step was found to yield a smaller crystallite size than its calcined counterpart.[60] Consistent with the smaller crystallite size, the XRD pattern of uncalcined (UC) Ni/SiO_2 revealed broader and weaker peaks in agreement with the other Ni_xP_y phases (Figure 32). To probe the effect of the different crystallite sizes, physical characterizations and CO_2 HYD studies were carried out on both calcined and uncalcined Ni/SiO_2 (denoted Ni/SiO_2-c and Ni/SiO_2-uc, respectively).

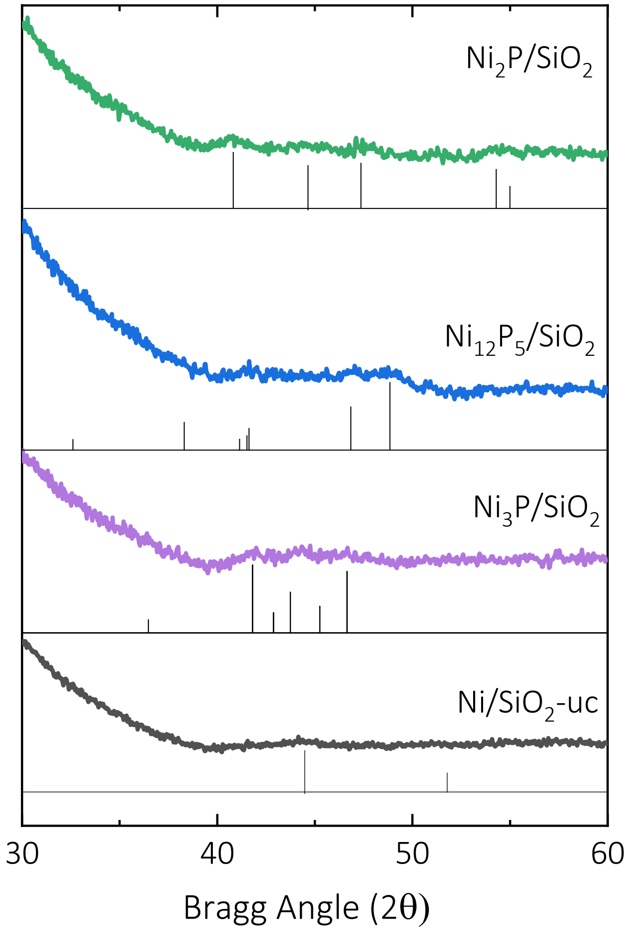

Figure 32. XRD patterns for 2.5 wt% Ni-c, Ni_3P, $Ni_{12}P_5$, and Ni_2P on SiO_2 with stick reference patterns.

The signal-to-noise ratio (S/N) for the 2.5 wt% Ni_xP_y/SiO_2 catalysts was low due to the small amount of Ni_xP_y contributing to the signal. To corroborate the phase identities, higher loadings were also analyzed (Figure 33). TEM is needed for crystallite and particle size determination of the 2.5 wt% Ni_xP_y/SiO_2 series.

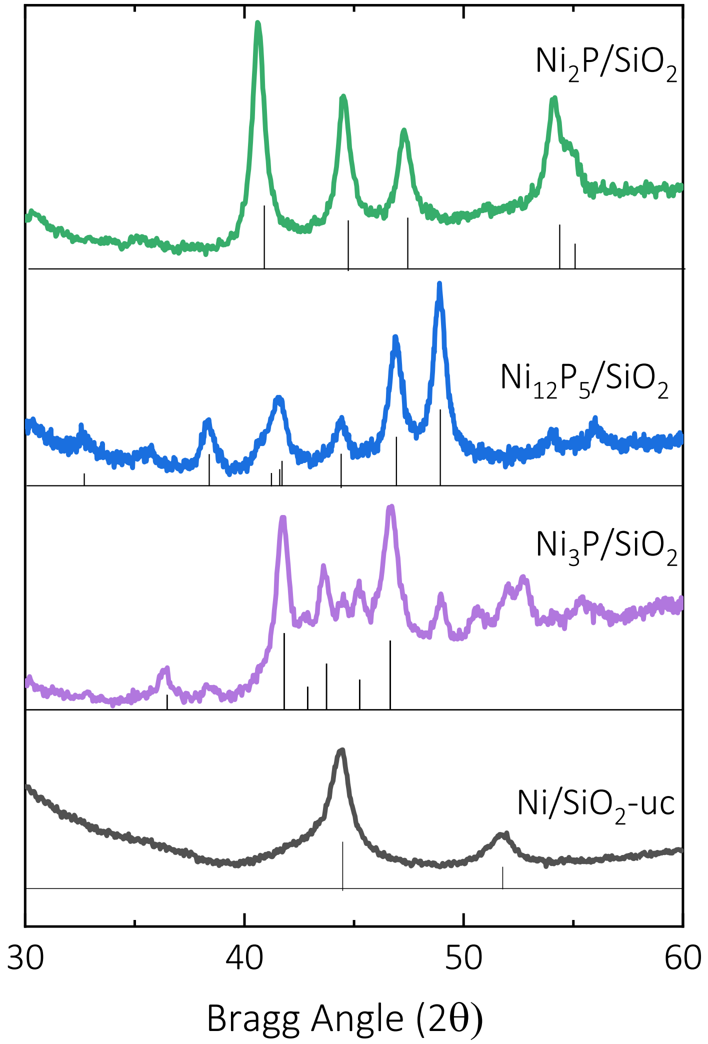

Figure 33. XRD patterns for 15 wt% Ni-uc, Ni_3P, $Ni_{12}P_5$, and Ni_2P on SiO_2 with stick reference patterns.

Two phases of 2.5 wt% Ni_xP_y/TiO_2 catalysts—Ni_2P and $Ni_{12}P_5$—were synthesized to compare the photocatalytic properties to the SiO_2-supported counterparts. Diffraction patterns of 2.5 wt% Ni_xP_y/TiO_2 were obtained using XRD, by which the crystallite sizes were too small to determine using the Scherrer equation. A higher loading was also analyzed for each phase to yield higher signal from the Ni_xP_y crystals to corroborate phase identification (Figure 34). TEM is needed for crystallite and particle size determination of the 2.5 wt% Ni_xP_y/TiO_2 series.

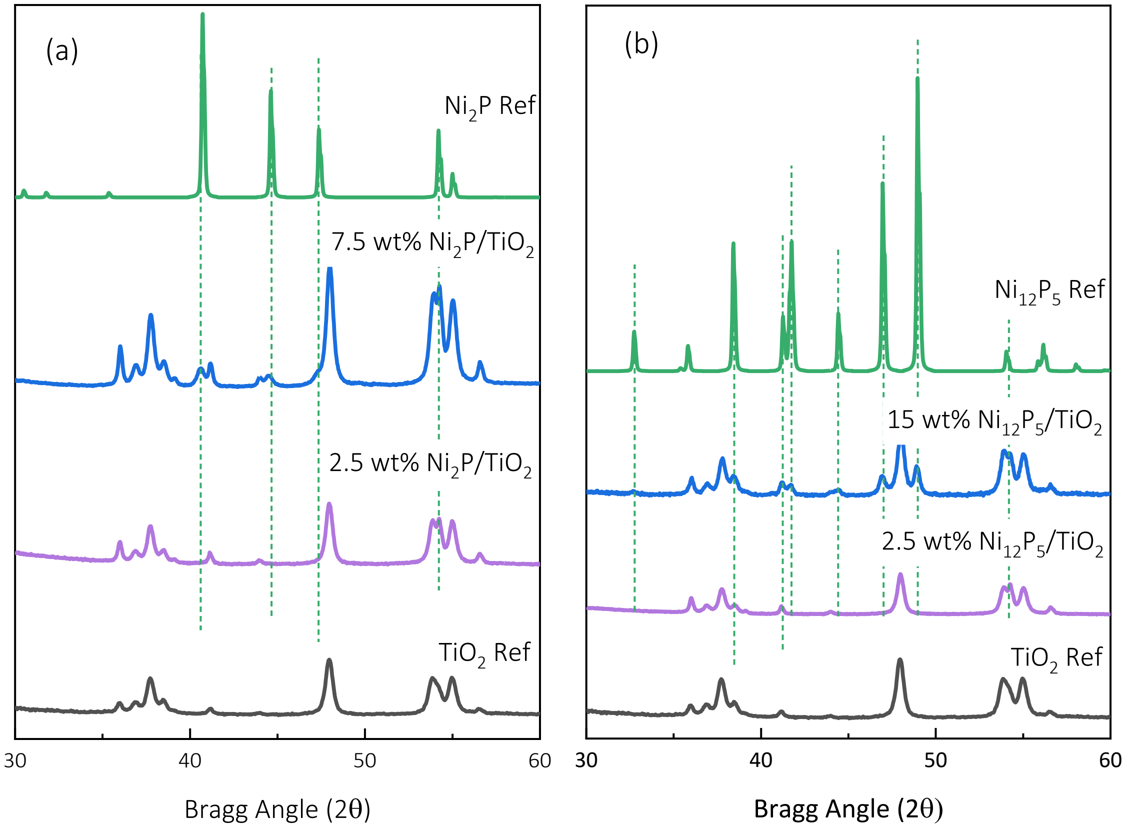

Figure 34. XRD pattern for (a) 2.5 and 7.5 wt% Ni_2P/TiO_2 and (b) 2.5 and 15 wt% $Ni_{12}P_5/TiO_2$ with the reference patterns for Ni_2P, $Ni_{12}P_5$, and TiO_2 (card no. 21-1272).

3.2 Catalyst Composition

The actual P/Ni ratio of the final catalysts was first measured by EDS (Table 5). The SiO_2-supported 2.5 wt% Ni_xP_y catalyst series had measured P/Ni ratios in closer agreement to the stoichiometric ratio than the TiO_2-supported series. However, the non-homogenous distribution of Ni_xP_y NPs on the support leads to variability between P/Ni measurements at different locations on the powdered catalysts, resulting in significant uncertainty in the measured P/Ni and wt% loading value. In order obtain a more representative measurement of the nominal P/Ni ratio and Ni_xP_y wt%, a heat-assisted acid digestion was done to dissolve the Ni and P into solution, which was then analyzed by ICP-OES (Table 5). The composition of Ni_2P/SiO_2 was found to be more P-rich (P/Ni = 0.76) and $Ni_{12}P_5/TiO_2$ more Ni-rich (P/Ni = 0.23) than expected based on their respective P/Ni stoichiometric ratios (0.5 and 0.42, respectively). Overall, the trends in P/Ni ratio and wt% loading were similar between the two analytical techniques.

Table 5. Compositional analysis by EDS and ICP-OES.

Catalyst	Stoichiometric P/Ni Ratio	Measured P/Ni Ratio by EDS	Measured P/Ni Ratio By ICP-OES	Measured Ni_xP_y loading (wt%) by ICP-OES
Ni/SiO_2-c	0	0	0	2.48
Ni/SiO_2-uc	0	0	0	2.48
Ni_3P/SiO_2	0.33	0.26 ± 0.08	0.32	2.24
$Ni_{12}P_5/SiO_2$	0.42	0.4 ± 0.1	0.47	2.22
Ni_2P/SiO_2	0.50	0.6 ± 0.1	0.76	2.79
$Ni_{12}P_5/TiO_2$	0.42	0.28 ± 0.02	0.23	2.31
Ni_2P/TiO_2	0.50	0.78 ± 0.05	0.58	2.61

3.3 Surface Characterization

Pulsed CO chemisorption and N_2 physisorption methods were used to characterize the active site density and BET surface area, respectively (Table 6). Multi-point BET surface area analysis was not performed on all catalysts, so only the surface areas determined by single-point BET analysis was reported for comparison. As the P/Ni ratio increased, the CO chemisorption capacity decreased in a linear trend with the exception of Ni/SiO_2-c (Figure 35), suggesting that CO chemisorption is an effective probe of surface Ni sites.

Table 6. Surface characterization by CO chemisorption and N_2 physisorption.

Catalyst	CO Chemisorption Capacity (μmol/g_{cat})	BET Surface Area (m^2/g)
SiO_2	<1	380
Ni_2P/SiO_2	10.8	240
$Ni_{12}P_5/SiO_2$	14.7	310
Ni_3P/SiO_2	31.1	291
Ni/SiO_2-c	15.5	284
Ni/SiO_2-uc	89.1	300

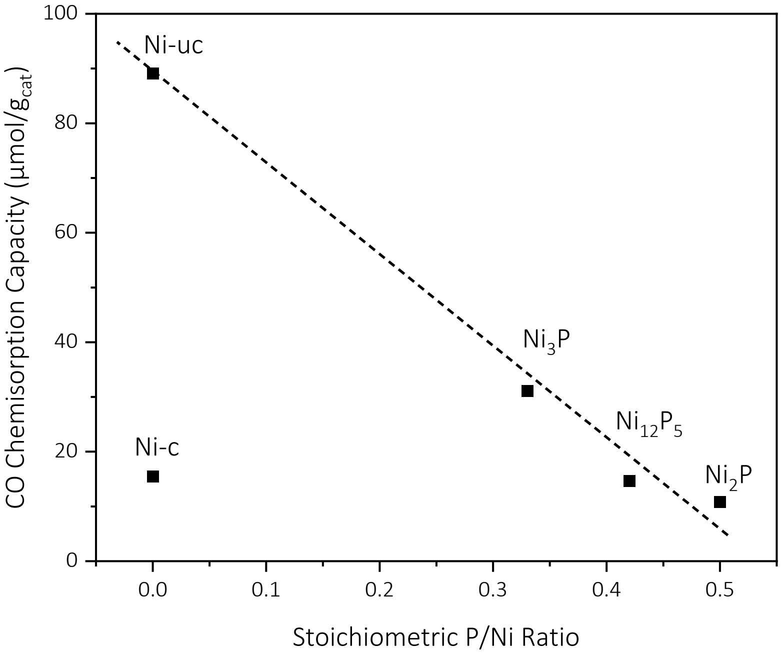

Figure 35. CO chemisorption capacity as a function of P/Ni ratio for 2.5 wt% Ni_xP_y/SiO_2 catalysts.

Moreover, the trend in CO chemisorption capacity as a function of P/Ni ratio was in agreement with that of CO_2 HYD rate as a function of P/Ni ratio (Figure 36). Both measurements had a negative linear correlation with P/Ni ratio with the exception of Ni-c.

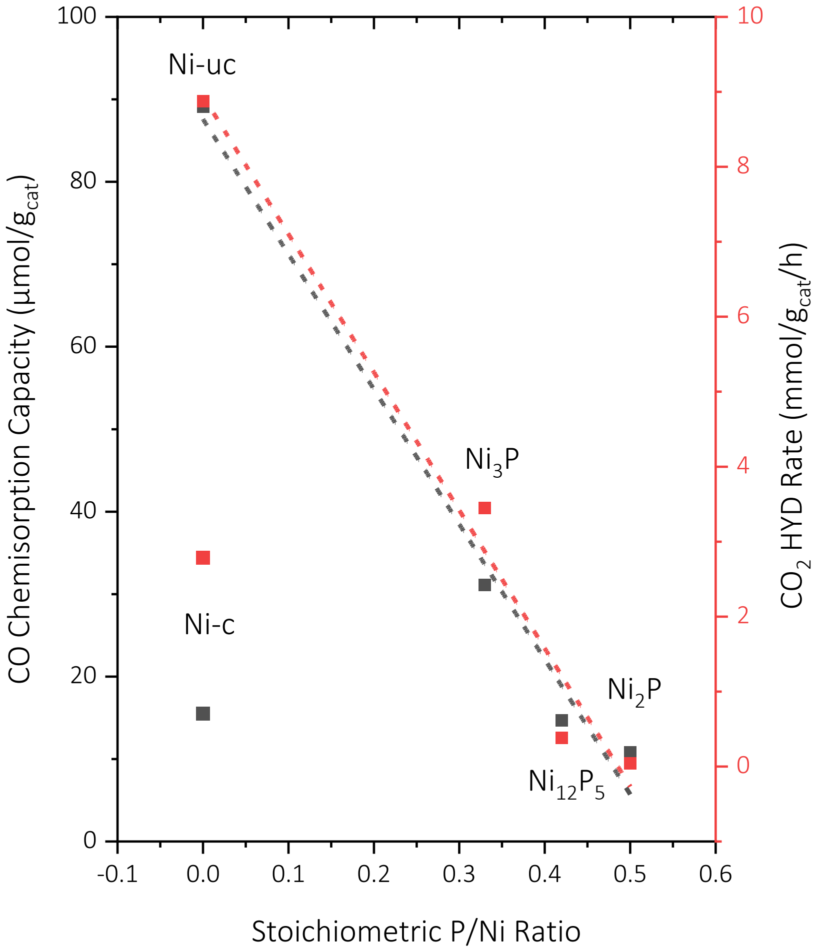

Figure 36. CO chemisorption capacity (black) and CO_2 HYD rate (red) as a functions of P/Ni ratio for 2.5 wt% Ni_xP_y/SiO_2 catalysts. Linear trendlines are shown and exclude Ni-c.

CO_2 HYD was evaluated as a function of CO chemisorption capacity, revealing a positive linear correlation for all Ni_xP_y/SiO_2 phases (Figure 37). These findings suggest that surface Ni sites (as measured by CO chemisorption) are the active sites ve sites for CO_2 hydrogenation.

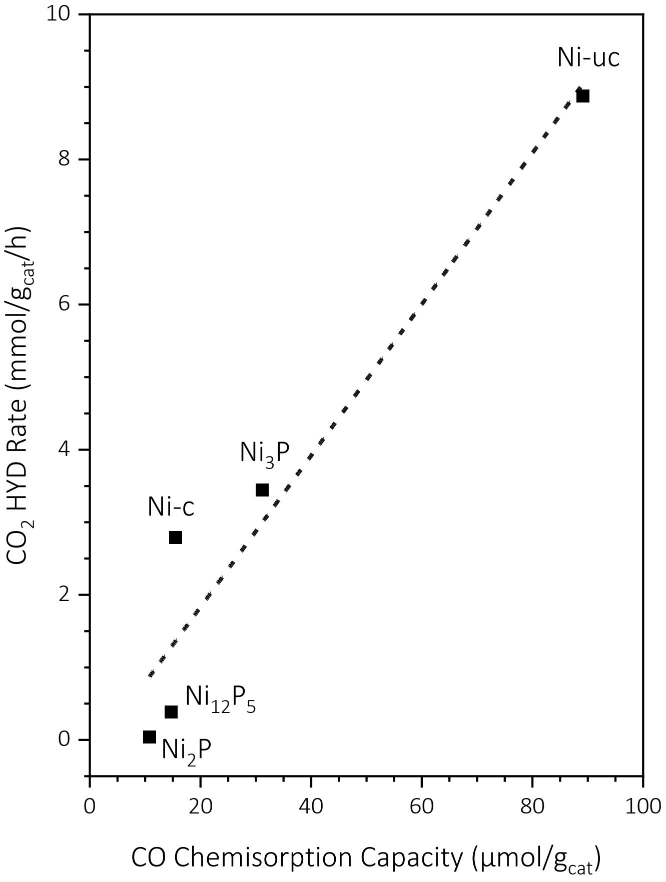

Figure 37. CO_2 HYD rate as a functions of P/Ni ratio for 2.5 wt% Ni_xP_y/SiO_2 catalysts. A linear trendline is shown and includes all Ni_xP_y/SiO_2 phases.

The disparate CO chemisorption capacities for Ni-c and Ni-uc can be explained by their Ni crystallite size differences (13.9 vs. < 5 nm). Nanoparticle size dictates the dispersion—or ratio of surface to bulk atoms—as well as the relative amounts of edge and terrace adsorption sites (Figure 39).[17,61,62] As the crystallite size decreases, the amount of edge sites increases relative to terrace sites.[61] The lower-coordinated edge sites are found to preferentially bind to CO in a linear conformation whereas the higher-coordinated terrace sites facilitate bridge bonding of one CO molecule to two or three Ni atoms.[62,63] In agreement with this trend in size-dependence, Witzke et al. reported a lower CO chemisorption capacity for $Ni_{12}P_5/SiO_2$ nanoparticles of 19 nm compared to and 5 nm (Figure 38).[64]

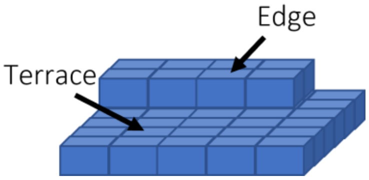

Figure 39. Graphic representation of terrace and step sites.

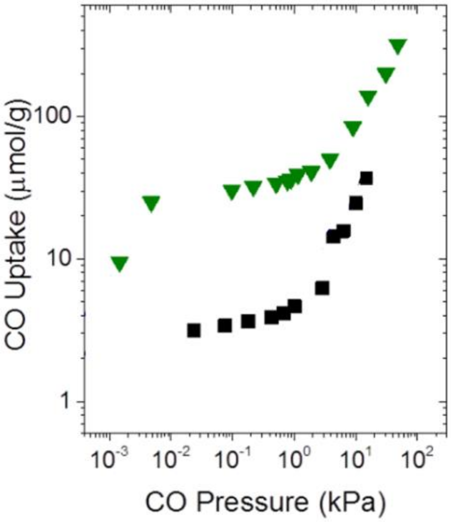

Figure 38. CO adsorption isotherm (298 K) for $Ni_{12}P_5/SiO_2$ for 19 nm (■) and 5 nm (▼) particles. Figure adapted from ref [64] with permission under the Creative Commons Attribution 4.0 International License. Data for other phases removed from plot for clarity.

Future work to characterize the crystallite and particle sizes by high resolution transmission electron microscopy (HRTEM) is necessary and can subsequently be used to gain computational insight on the size-dependent nature of active site density for each Ni_xP_y phase using density functional theory (DFT) calculations.[61,64]

3.4 Optical Absorbance

The optical absorbance of the Ni_xP_y/SiO_2 catalyst was characterized over 250–1250 nm by diffuse reflectance (DR) UV-Vis-NIR spectroscopy. As the relative Ni content increased, the absorbance intensity increased monotonically across the entire spectral range for the Ni_xP_y/SiO_2 catalysts (Figure 40a). The increased absorbance of Ni_xP_y/SiO_2 compared to SiO_2 is consistent with the color change observed in the final products (Figure 40b-f). The absorbance-decreasing effect of P dilution of the Ni ensemble indicates that the hypothesized stabilizing and selectivity-enhancing role of P is accompanied by a deleterious effect on the light absorbing properties.

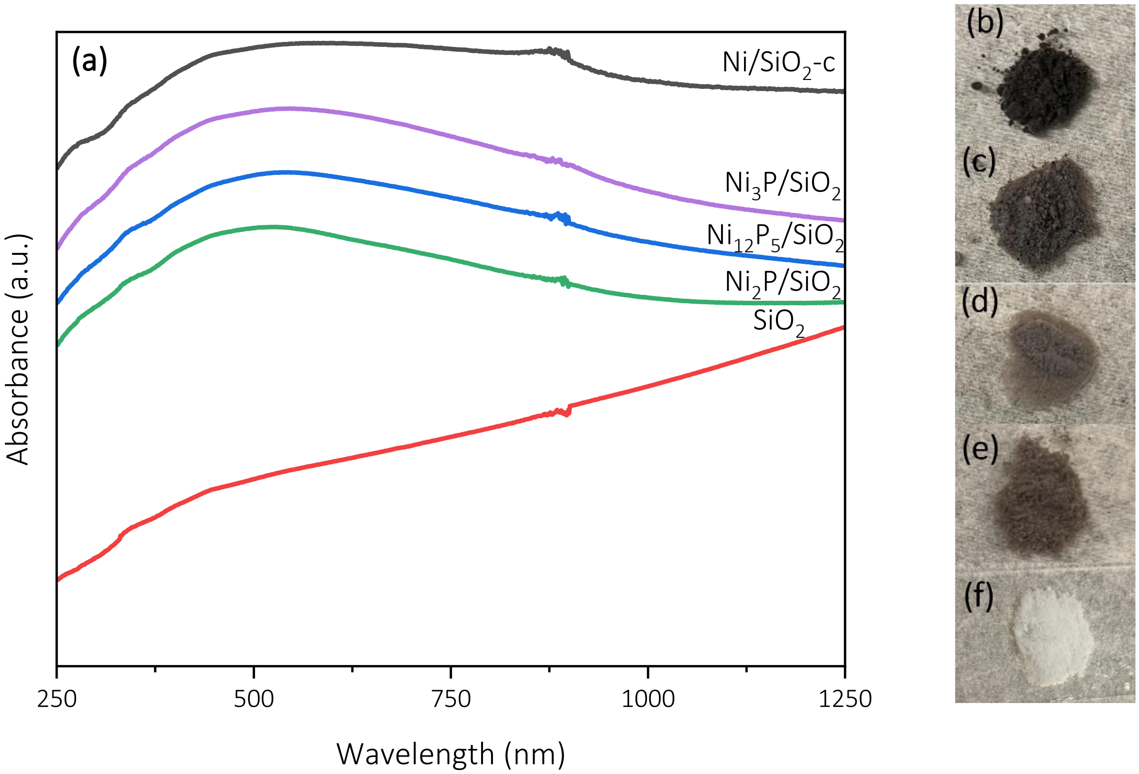

Figure 40. (a) Absorbance spectra for SiO_2 and 2.5 wt% Ni_xP_y/SiO_2 and photos of 2.5 wt% (b) Ni/SiO_2-c, (c) Ni_3P/SiO_2, (d) $Ni_{12}P_5/SiO_2$, (e) Ni_2P/SiO_2, and (f) reduced SiO_2.

The absorbance trend diverged for 2.5 wt% Ni/SiO_2-uc, which was lighter in color and had lower absorbance intensity across the spectrum compared to its calcined counterpart (Figure 41).

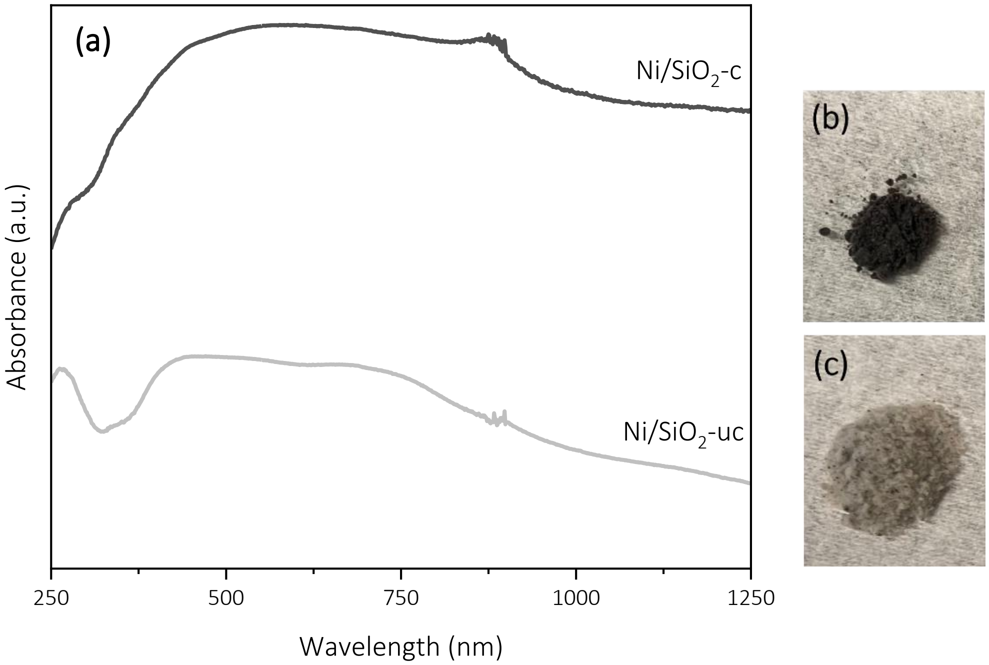

Figure 41. (a) Absorbance spectra of 2.5 wt% Ni/SiO_2-c and Ni/SiO_2-uc with corresponding photos (b) Ni/SiO_2-c and (c) Ni/SiO_2-uc.

However, Ni/SiO_2-uc turned near-black after the in-situ H_2 activation that precedes CO_2 HYD reactions (Figure 42). Color changes were not observed for the calcined Ni_xP_y/SiO_2 catalysts during activation. The smaller Ni crystallite size of Ni/SiO_2-uc compared to Ni/SiO_2-c corresponds to a greater ratio of surface-to-bulk Ni atoms, which allows for more surface atoms to be oxidized (i.e., Ni^{2+} via surface NiO formation) during post-TPR passivation and subsequent air exposure. To achieve

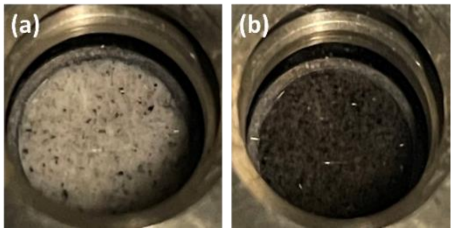

Figure 42. Photos of 2.5 wt% Ni/SiO_2- uc (a) before and (b) after in-situ activation at 673 K under flowing H_2 (30 mL/min) for 1 h.

characterization of the activated (i.e., re-reduced) catalyst's absorbance properties, future work should include in-situ UV-Vis-NIR on Ni/SiO_2-uc following H_2 activation.

TiO_2-supported Ni_xP_y phases were also analyzed by DR-UV-Vis-NIR spectoscopy. As observed for the SiO_2 support, Ni_xP_y increased absorbance across the spectrum and darkened the color compared to reduced TiO_2 alone (Figure 43, Figure 44). The more nickel-rich $Ni_{12}P_5/TiO_2$ phase absorbed light more strongly than Ni_2P/TiO_2—particularly across the visible and NIR range.

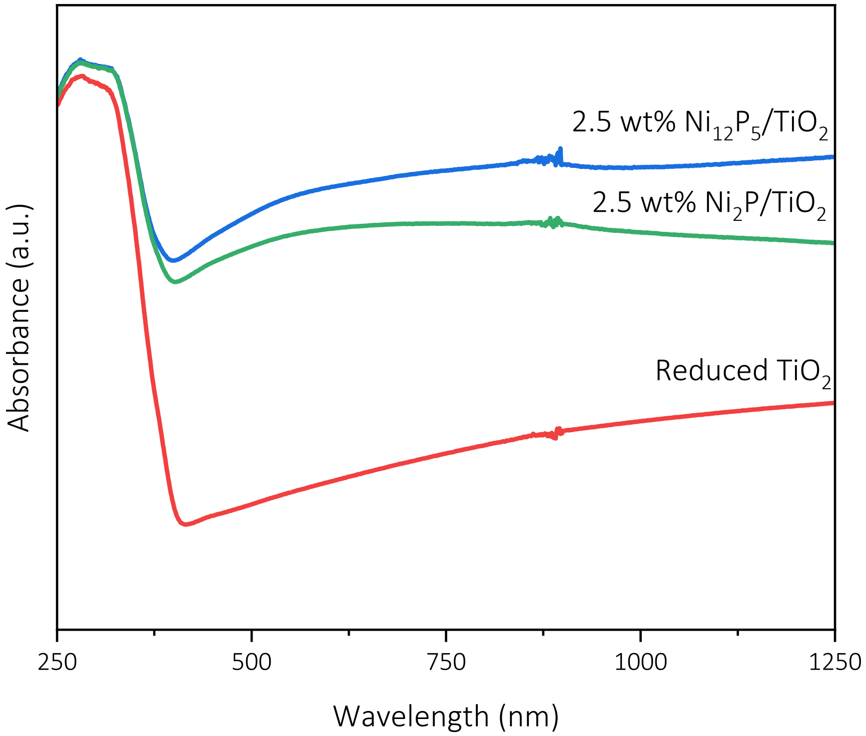

Figure 43. Absorbance spectra for TiO_2 and 2.5 wt% Ni_xP_y/TiO_2 catalyst.

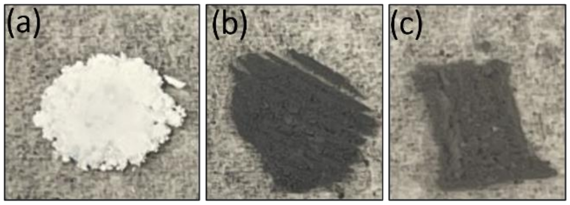

Figure 44. Photos of (a) reduced TiO_2, (b) 2.5 wt% $Ni_{12}P_5/TiO_2$, and (c) 2.5 wt% Ni_2P/TiO_2.

Although reduction conditions for the Ni_xP_y/TiO_2 were milder than is typically used to produce oxygen-deficient TiO_2, an increase in absorbance intensity and slight darkening of color was observed for reduced TiO_2 compared to its unreduced counterpart (Figure 45 and Figure 46).[39,65] The increased absorbance supports the hypothesis that a reducible oxide support will enhance the photothermal properties of the Ni_xP_y/TiO_2 catalysts by contributing mid-bandgap defect states formed by surface defects (i.e., oxygen vacancies).

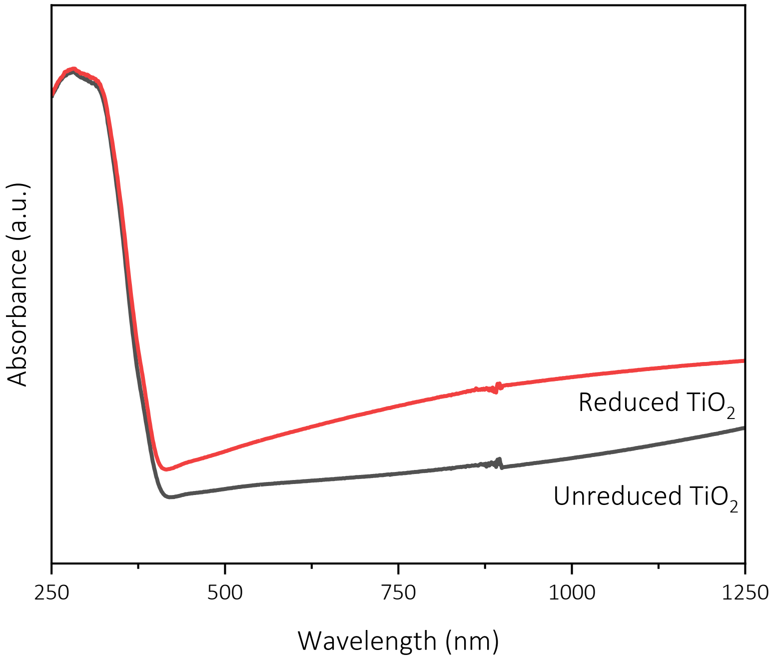

Figure 45. Absorbance spectra of reduced and unreduced TiO_2.

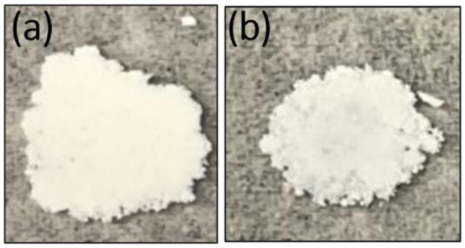

Figure 46. Photos of (a) unreduced and (b) reduced TiO_2.

3.5 Raman Thermometry

3.5.1 TiO_2

Raman spectroscopy was carried out at different temperatures to probe the photothermal properties of TiO_2 and its Ni_xP_y/TiO_2 counterparts. First, a room-temperature spectrum of reduced TiO_2 was acquired. Five Raman peaks at 145.3, 196.7, 394.4, 511.2, and 633.0 cm^{-1}, which can be assigned to the $E_{g(1)}$, $E_{g(2)}$, B_{1g}, $A_{1g} + B_{1g(2)}$, and $E_{g(3)}$ Raman-active modes, respectively, of the anatase phase (Figure 47).[40,65] Though the commercial TiO_2 used in this work contains a mixture of anatase (major) and rutile (minor) phases, only anatase character was present in the Raman spectrum.

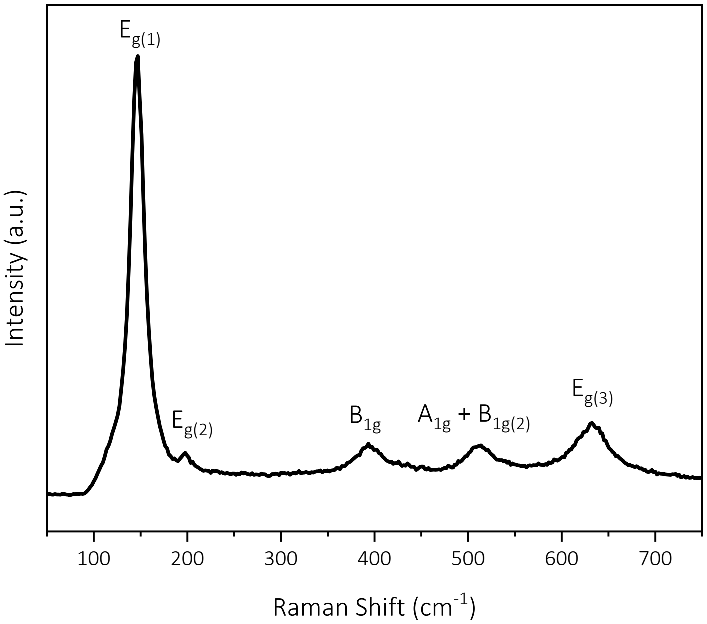

Figure 47. Room-temperature Raman spectrum of reduced TiO_2.

To evaluate the temperature dependence of the Raman scattering for TiO_2, spectral acquisitions were carried out at temperatures of 298–523 K in 50 K intervals. The five characteristic peaks present at room temperature were also observed for the spectra obtained at all tempeartures, but changes in the Raman shift and intensity of each mode were evident as temperature increased (Figure 48).

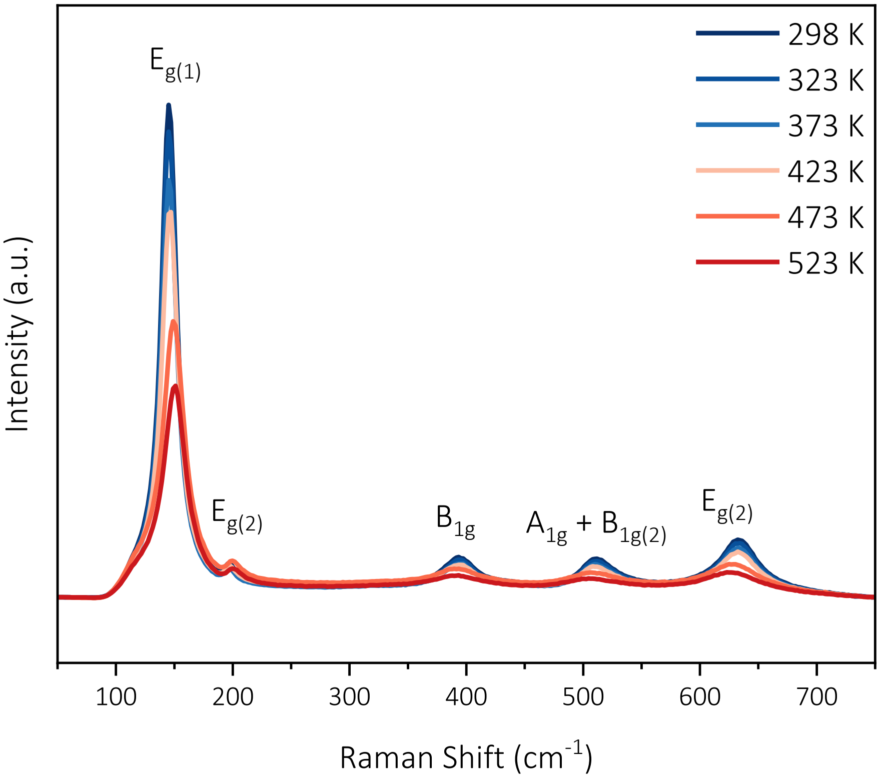

Figure 48. Raman spectra of reduced TiO_2 obtained at temperatures of 298–523 K at 100% laser power and 10 s acquisition time.

The B_{1g}, A_{1g} + $B_{1g(2)}$, and $E_{g(3)}$ vibrational modes exhibited a trend of decreasing Raman shift as the stage temperature increased, which is attributed to thermal relaxation of the bonds with which the incident photons are interacting (Figure 49).[55,56] Additionally, the Raman intensity decreased as the temperature increased, which corresponds to a decrease in ground state electrons available for Stokes scattering.

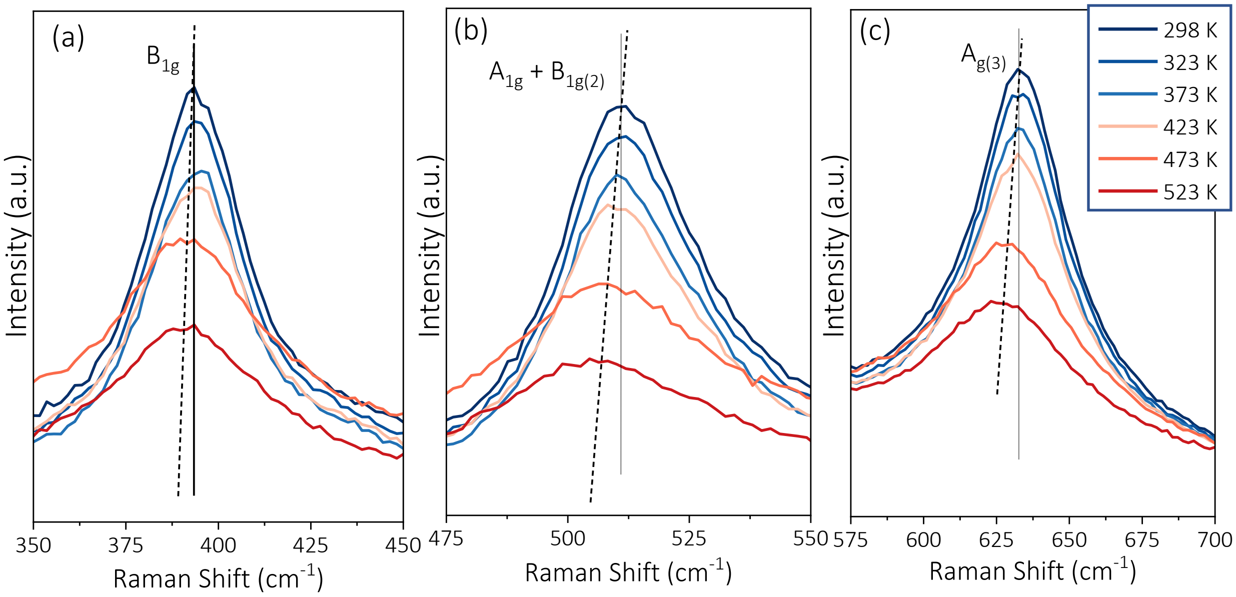

Figure 49. Raman spectra of TiO_2 obtained at temperatures of 298–523 K for vibrational modes (a) B_{1g}, (b) A_{1g} + $B_{1g(2)}$, and (c) $A_{g(3)}$. Solid lines are drawn straight down from the center of the peak at 298 K and dashed lines are drawn to connect the centers of the 298 K and 523 K peak to guide the eye.

The Raman shifts of the B_{1g}, A_{1g} + $B_{1g(2)}$, and $E_{g(3)}$ modes of anatase TiO_2 had a negative linear correlation with temperature over the analyzed range of 298–523 K indicated by Pearson correlation values of -0.953, -0.924, and -0.913, respectively. A linear regression of the Raman shift vs. temperature was then carried out to obtain fit parameters (Figure 50). The slope of the line was used as the temperature coefficient (χ) and the Raman shift at 0 K was extrapolated from the linear regression equation for each phonon mode (Equation 6, Table 7).

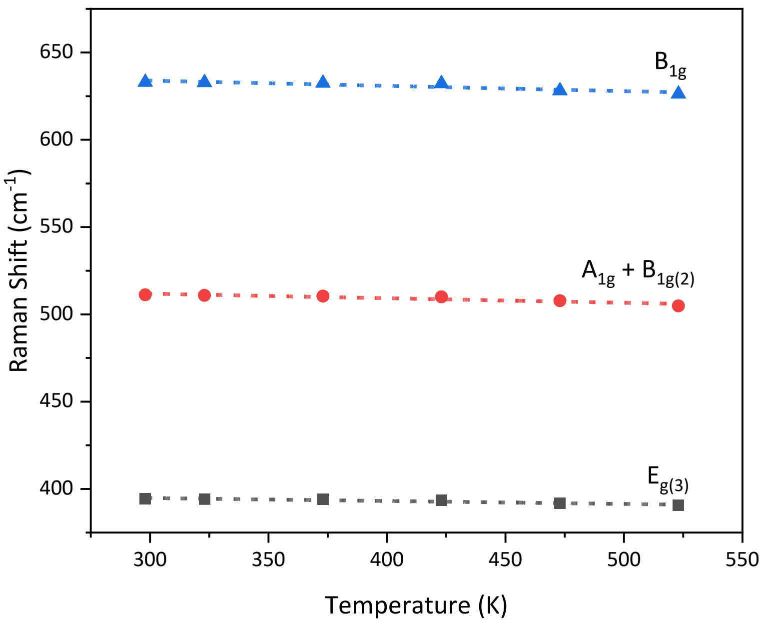

Figure 50. Raman shift vs. temperature for TiO_2 with a linear regression for phonon modes B_{1g} with fit parameters [m = -0.017 ± 0.003, b = 399 ± 1, R^2 = 0.909], $A_{1g} + B_{1g(2)}$ with fit parameters [m = -0.026 ± 0.005, b = 520 ± 2, R^2 = 0.855], and $E_{g(3)}$ with fit parameters [m = -0.030 ± 0.007, b = 643 ± 3, R^2 = 0.833].

Table 7. Fitting parameters for Raman-active modes of TiO_2.

Phonon Mode	χ (cm^{-1}/K)	ω_0 (cm^{-1})
B_{1g}	-0.017 ± 0.003	399 ± 1
$A_{1g} + B_{1g(2)}$	-0.026 ± 0.005	520 ± 2
$E_{g(3)}$	-0.030 ± 0.007	643 ± 3

Conversely, the $E_{g(1)}$ and $E_{g(2)}$ modes centered at ~145 and ~197 cm^{-1} exhibited increasing Raman shift with increasing temperature, which is attributed to the effect of anharmonic phonon coupling dominating over that of thermal expansion for those modes (Figure 51).[56,66]

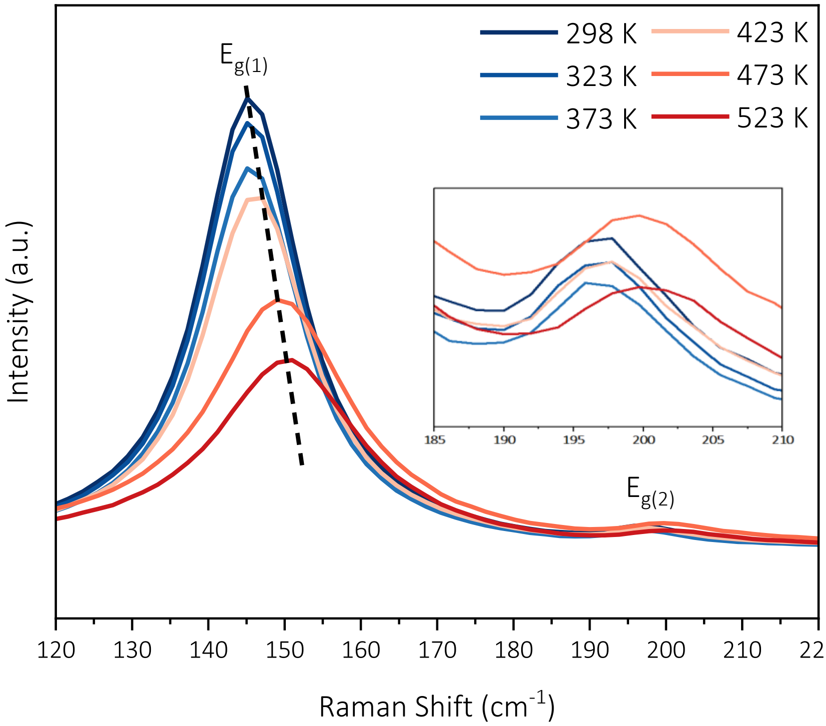

Figure 51. Raman spectra of the $E_{g(1)}$ and $E_{g(2)}$ modes obtained at different stage temperatures. The inset shows an enlargement of shoulder peak corresponding to the $E_{g(2)}$ mode.

Both thermal expansion and phonon-phonon coupling have been shown to contribute to the temperature-dependence of Raman scattering of solids, but the extent of their respective contributions differ for each Raman-active phonon mode.[55,56,67] In the present work, only the linear fitting of the temperature-dependent Raman shift is used to obtain the χ and ω_0 fitting parameters to facilitate a summative estimation of local temperatures for Ni_xP_y/TiO_2. In future work, a multiparameter fitting is recommended to parse out the degree of contribution for anharmonic processes (i.e., thermal expansion vs. phonon-phonon coupling) and facilitate more accurate estimations of local temperature.

3.5.2 $Ni_{12}P_5/TiO_2$

Room-temperature Raman spectroscopy was used to analyze 2.5 wt% $Ni_{12}P_5/TiO_2$, revealing five peaks centered at 146.9, 198.9, 393.0, 510.4, and 631.6 cm^{-1} (Figure 52). No new features were observed, indicating that the Raman scattering can be attributed to the same scattering interactions with TiO_2 modes. However, the $Ni_{12}P_5/TiO_2$ was darker in color and had greater absorbance properties, which corresponded to being sensitive to laser-induced photodamage following exposure to laser powers greater than 5% as observed under the optical microscope. Following laser exposure at powers greater than 5%, the incident spot appeared lighter in color under the optical microscope. Photodamage was avoided by using 5% laser power to acquire spectra of $Ni_{12}P_5/TiO_2$. No evidence of photodamage was present for reduced TiO_2 at any laser power, so 100% laser power was used to acquire spectra with high signal-to-noise ratio (S/N).

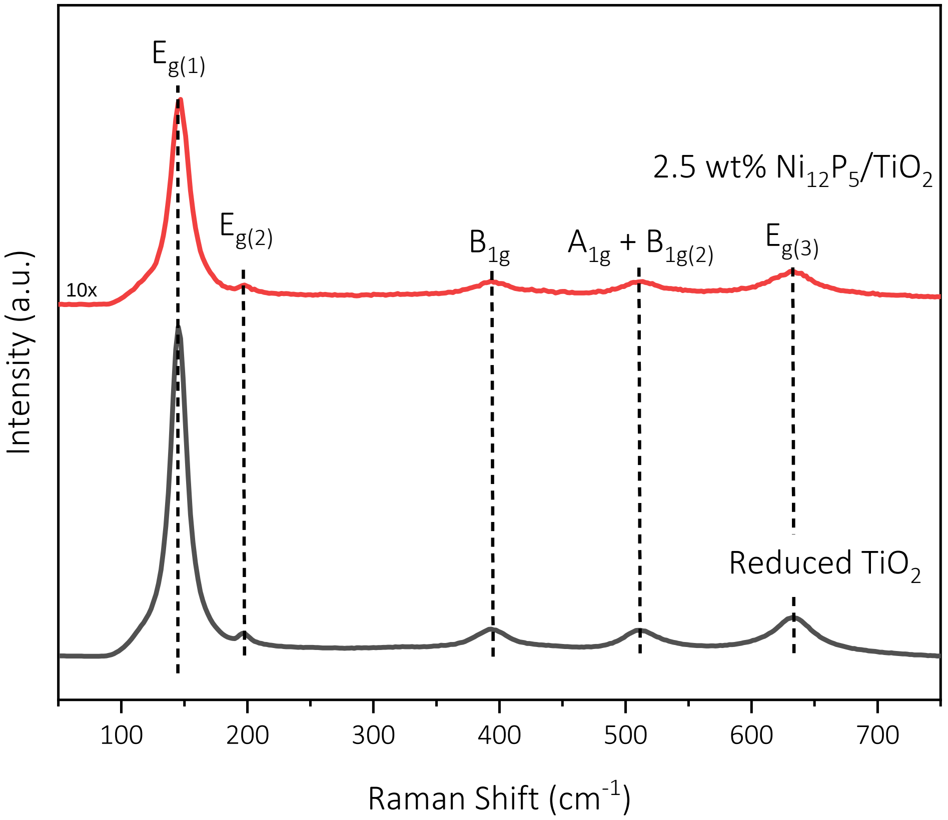

Figure 52. Room-temperature Raman spectra of 2.5 wt% $Ni_{12}P_5/TiO_2$ and reduced TiO_2.

To evaluate the temperature dependence of the Raman scattering for 2.5 wt% $Ni_{12}P_5/TiO_2$, spectra were collected at increasing temperatures (298–523 K) with 20–30 K intervals (Figure 53). From the spectra it is evident that 10 s acquisitions at 5% power resulted in poor S/N; repeated studies with longer acquisition times is recommended to improve S/N in future work.

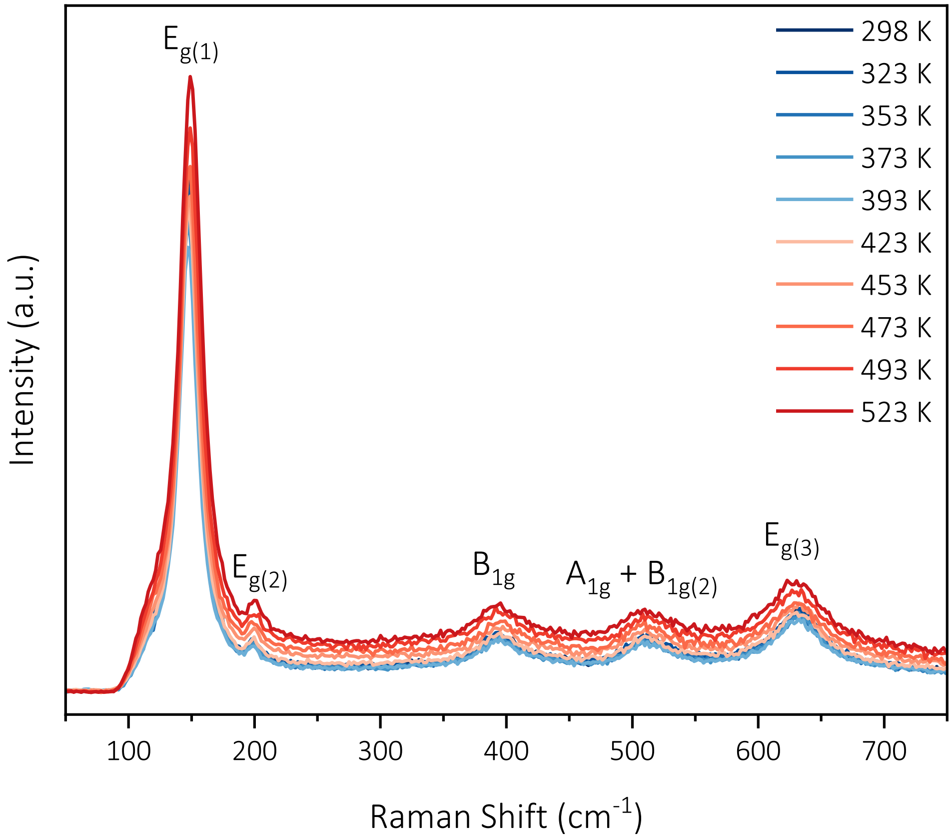

Figure 53. Raman spectra of 2.5 wt% $Ni_{12}P_5/TiO_2$ obtained at temperatures of 298–523 K at 5% laser power with 10 s acquisition time.

Unlike for TiO_2, the intensity of the Stokes scattering for 2.5 wt% $Ni_{12}P_5/TiO_2$ increased monotonically with increasing temperature (Figure 54). The ground-state electon population is expected to decrease as those electrons are excited with increasing temperatures, which would correspond to a decreased intensity of Stokes scattering; the trend observed for $Ni_{12}P_5/TiO_2$ is contrary to this. To gain a better understanding of the temperature dependence of TiO_2 and $Ni_{12}P_5/TiO_2$, it is recommended that future studies include detection of both Stokes and anti-Stokes scattering to probe for changes in their ratio with increasing temperature. However, the same trend of Raman upshift of the $E_{g(1)}$ and $E_{g(2)}$ modes and downshift of the B_{1g}, $A_{1g} + B_{1g(2)}$, and $E_{g(3)}$ modes observed for TiO_2 was also observed for $Ni_{12}P_5/TiO_2$, which is in agreement with the expected temperature-dependence of Stokes scattering (Figure 54, Figure 55).[55,56]

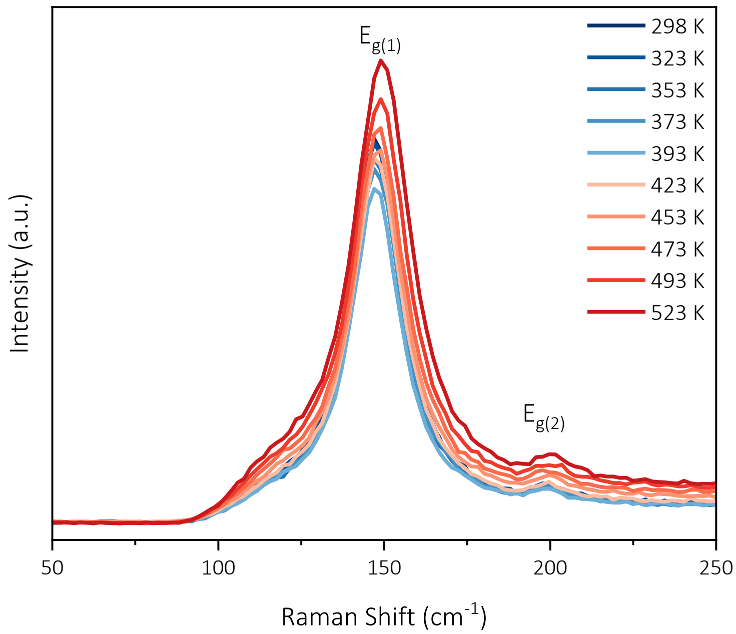

Figure 54. Raman spectra of the $E_{g(1)}$ and $E_{g(2)}$ modes obtained at temperatures of 298–523 K at 5% laser power with 10 s acquisition time.

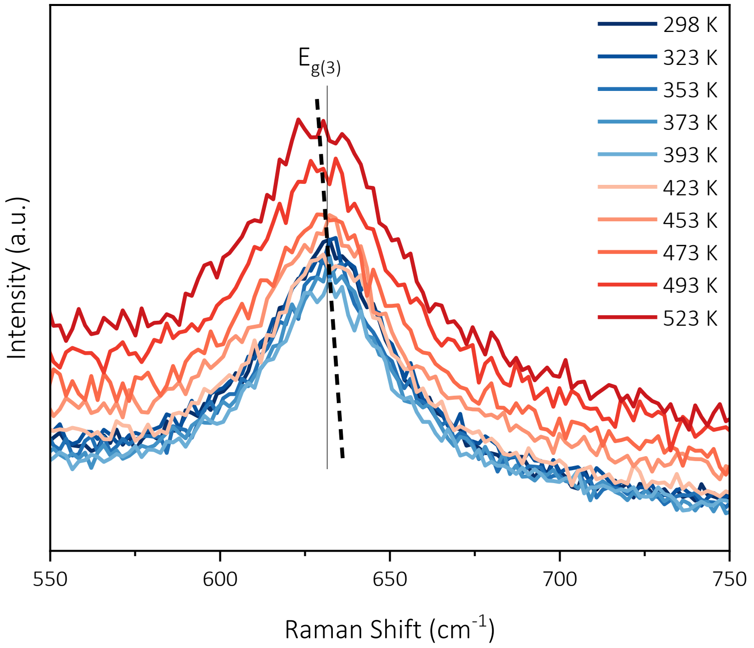

Figure 55. Raman spectra of the $E_{g(3)}$ mode obtained at temperatures of 298–523 K at 5% laser power with 10 s acquisition time.

3.6 Photocatalytic Performance: Ni_xP_y/SiO_2

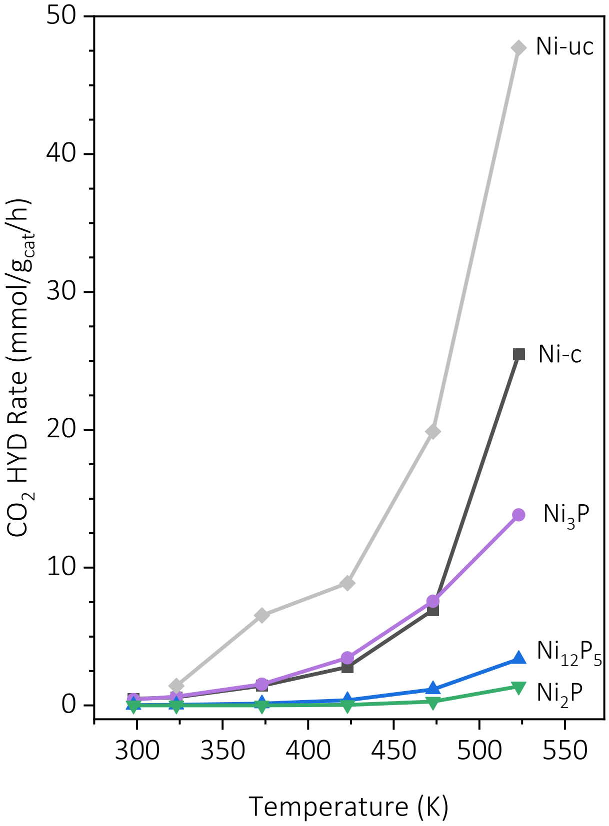

Figure 56. CO_2 hydrogenation rate vs. reaction temperature in light over 2.5 wt% Ni_xP_y/SiO_2 for Ni-uc, Ni-c, Ni_3P, $Ni_{12}P_5$, and Ni_2P.

Photothermal catalytic performance was evaluated for the RWGS reaction in light and dark at temperatures of 298–523 K, from which the effects of external temperature, irradiation, and Ni_xP_y phase could be elucidated. First, CO_2 HYD rates in light were compared for the 2.5 wt% Ni_xP_y/SiO_2 series as a function of reaction temperature (**Figure 56**). The CO_2 HYD rate increased monotonically with increasing temperature for all phases. As the P/Ni ratio of the Ni_xP_y phase decreased, activity increased at all temperatures except over Ni-c, for which Ni_3P outperformed until 523 K. Next, CO production rates were compared for the 2.5 wt% Ni_xP_y/SiO_2 series in the light as a function of reaction temperature (Figure 57). In agreement with the CO_2 HYD trend, CO production rates increased with decreasing P/Ni ratio at all tempeartures with the exception of Ni-c.

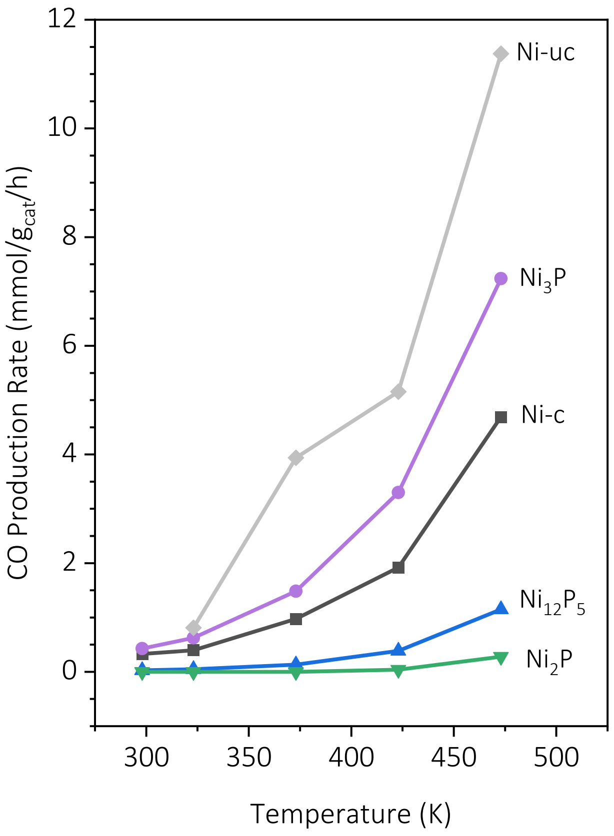

Figure 57. CO production rate vs. reaction temperature in light over 2.5 wt% Ni_xP_y/SiO_2 for Ni-uc, Ni-c, Ni_3P, $Ni_{12}P_5$, and Ni_2P.

Examining the disparity between -uc and -c Ni/SiO_2 performance, the active site density and size difference offer an explanation. Ni/SiO_2-uc had a 5.7 times CO chemisorption capacity than Ni/SiO_2-c and a much smaller average crystallite size (< 5 nm vs 13.9 nm). Larger Ni nanoparticles have a greater proportion of terrace atoms, which can stabilize an adsorbed CO (CO_{ads}) molecule via bridge-bonding with two or three Ni atoms.[63] Lower-coordinated edge Ni atoms are more likely to form a weaker linear bond with one CO molecule, which can desorb more readily and lead to a higher CO production rate.[62,63]

To evaluate the photoenhancement of the RWGS reaction for each catalyst, the CO production rate in light was divided by the CO production rate in dark (Figure 58). At 423 K—the lowest temperature at which all catalysts had activity in light and dark—Ni/SiO_2-uc exhibited 150% greater photoenhancement than Ni/SiO_2-c. With the addition of P, photoenhancement decreased monotonically with increasing P/Ni ratio. For Ni_2P, only a two-fold increase in CO production was observed under irradiation compared to in the dark.

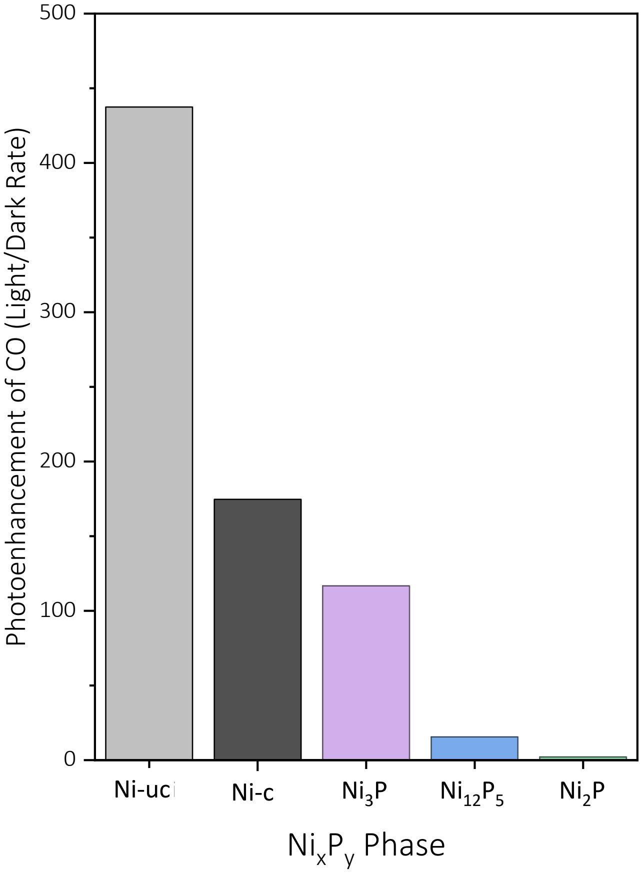

Figure 58. Photoenhancement of CO production rate (light/dark) at 423 K as a function of Ni_xP_y phase for 2.5 wt% Ni_xP_y/SiO_2.

As the reaction temperature increased, photoenhancement decreased monotonically across all Ni_xP_y/SiO_2 catalysts (Figure 59). The more pronounced photoenhancement at lower temperatures found in this work agrees with the findings of Xu et al. for the RWGS reaction over 10.4 wt% $Ni_{12}P_5/SiO_2$ with a ~6.5-fold photoenhancement at 473 K compared to a ~4.2-fold enhancement at 513 K.[25] These results are consistent with the hypothesized photo-induced local heating, the effect of which is expected to be superceded by external heating at high temperatures.

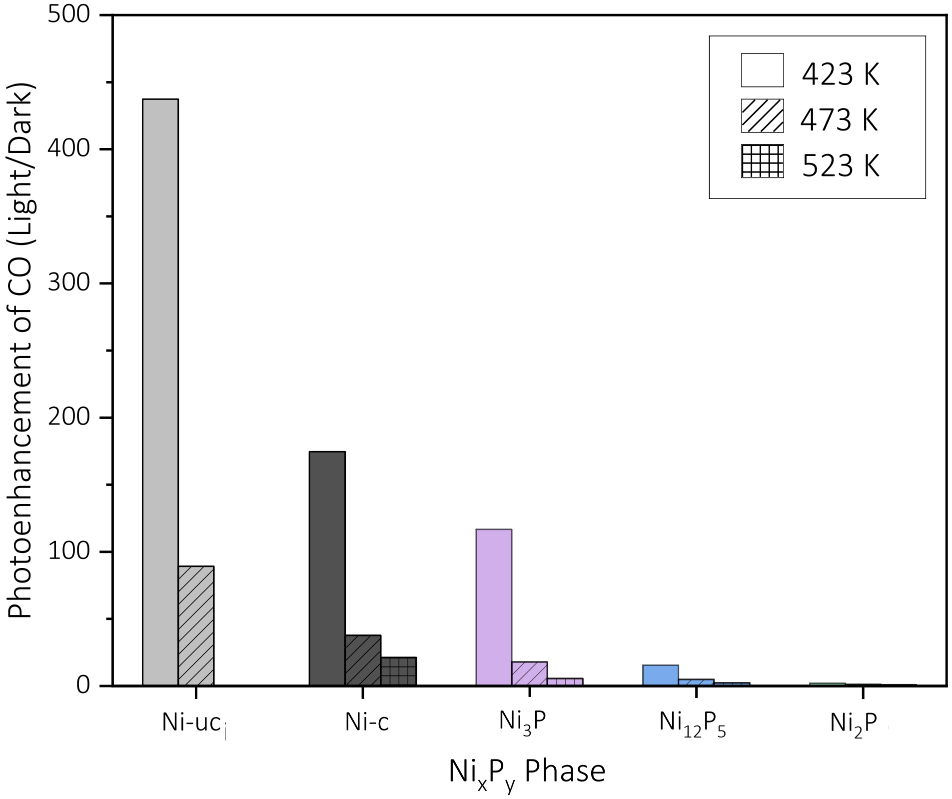

Figure 59. Photoenhancement of CO production rate at 423 , 473, and 523 K as a function of Ni_xP_y phase for 2.5 wt% Ni_xP_y/SiO_2. Data for Ni/SiO_2-uc at 523 K was not obtained.

The trend in optical absorbance intensity of calcined Ni_xP_y/SiO_2 followed the photoenhancement trend for increasing P/Ni ratio. To evaluate the correlation between the two characteristics, the absorbance spectrum of each catalyst was first integrated over 250–1250 nm (Equation 14, Table 8). Photoenhancement was then plotted as a function of integrated absorbance for CO production at 423, 473, and 523 K (Figure 60). A positive linear correlation was found for all three temperatures with Pearson's R coefficients of 0.960, 0.988, and 0.955, respectively.

Equation 14

$$\int_{250}^{1250} Absorbance\ Intensity\ (a.u.)$$

Table 8. Integral of absorbance intensity over 250–1250 nm

Ni_xP_y Phase	Integral of Absorbance over 250–1250 nm (a.u.)
Ni-c	832.8
Ni_3P	589.8
$Ni_{12}P_5$	467.9
Ni_2P	344.2

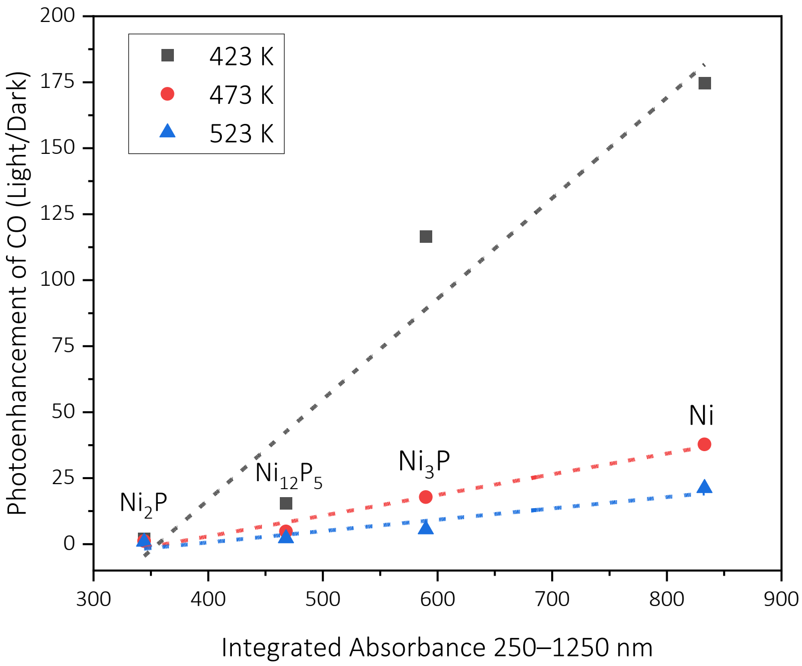

Figure 60. Photoenhancement of CO formation as a function of the integrated absorbance intensity for 2.5 wt% Ni_xP_y/SiO_2 at 423, 473, and 523 K with linear trendlines.

The effect of in-situ activation on the appearance of uncalcined Ni/SiO_2 (light gray to nearly black) makes it challenging to assess the absorbance of the activated catalyst used in the CO_2 HYD reactions. At present, Ni/SiO_2-uc is excluded from the analysis of photoenhancement vs. integrated absorbance. To extend the correlation between photoenhancement and absorbance to the uncalcined Ni/SiO_2, future work is recommended to include efforts to replicate the conditions of in-situ activation—or recover the catalyst after treatment in the reactor—to obtain an absorbance spectrum of the catalyst that more accurately matches what was used in the CO_2 HYD reactions.

Central to the goals if this project is probing the effect of P/Ni ratio on CO selectivity. First, the Ni_xP_y/SiO_2 catalysts were compared (Figure 61). At 423 K in light, CO selectivity increased in the order of Ni-c < Ni_3P < $Ni_{12}P_5$ = Ni_2P, with Ni/SiO_2-c having only 68.8% selectivity compared to 100% achieved by Ni_2P.

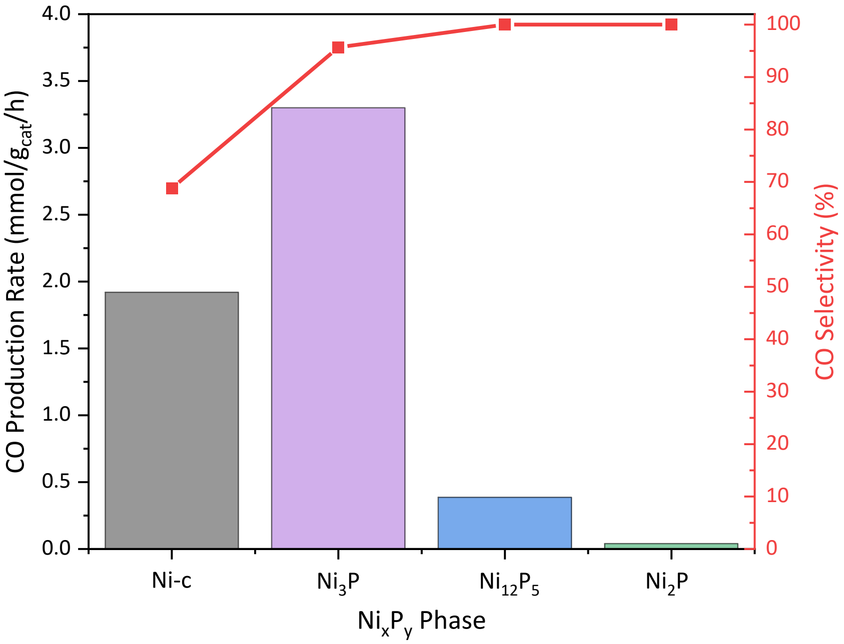

Figure 61. Overlayed plots of CO production rate and CO selectivity vs. Ni_xP_y phase for the RWGS reaction carried out over calcined 2.5 wt% Ni_xP_y/SiO_2 in the light at 423 K.

To investigate the influence of the larger average crystallite size of Ni/SiO_2-c compared to the other phases (13.9 nm vs. < 5 nm), Ni/SiO_2-uc (< 5 nm) was also evaluated (Figure 62). As previously discussed, the smaller crystallite size of Ni/SiO_2-uc was associated with a higher CO production rate compared its calcined counterpart. However, a decrease in CO selectivity was observed, suggesting smaller Ni particles also contain a higher proportion of sites that yield CH_4 instead of CO.

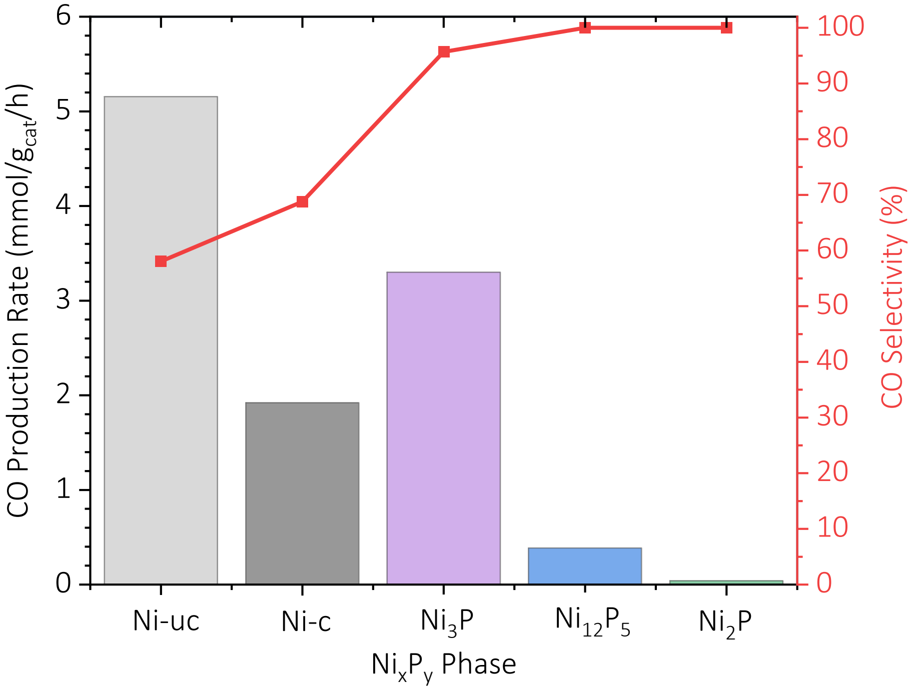

Figure 62. Overlayed plots of CO production rate and CO selectivity vs. Ni_xP_y phase for the RWGS reaction carried out over 2.5 wt% Ni_xP_y/SiO_2 in the light at 423 K.

Equation 14. Apparent quantum yield

$$\text{AQY (\%)} = \frac{\text{CO molecules produced per second}}{\text{number of incident photons per second}} \times 100$$

Another metric used to quantify performance as a CO_2 HYD catalyst under irradiation was apparent quantum yield (AQY), which is the number of CO molecules produced per incident photon (Equation 14). In contrast to quantum yield, which accounts only for photons that are absorbed by the material, AQY includes all incident photons entering the reactor. As such, the calculated AQY represents the low estimate of the quantum efficiency and avoids involving variables that are challenging to accurately quantify for quantum yeild (e.g., internal scattering).

AQY was calculated for the Ni_xP_y/SiO_2 catalysts at 298 and 423 K, which increased monotonically with decreasing P/Ni ratio at both temperatures (Table 9, Figure 63). Xu et al. reported a 0.0086% internal quantum yield of CO (IQY%)—which accounts for photon absorption—of 3.1 wt% $Ni_{12}P_5/SiO_2$ at room temperature.[25] In this work, the AQY for 2.5 wt% $Ni_{12}P_5/SiO_2$ at room temperature was determined to be 0.0042%, which agrees well with the literature value.

Table 9. CO apparent quantum yield for 2.5 wt% Ni_xP_y/SiO_2 at 298 and 423 K.

Ni_xP_y Phase	AQY_{CO} at 298 K (%)	AQY_{CO} at 423 K (%)
Ni-uc	--	1.5
Ni-c	0.086	0.50
Ni_3P	0.054	0.41
$Ni_{12}P_5$	0.0042	0.056
Ni_2P	0	0.0083

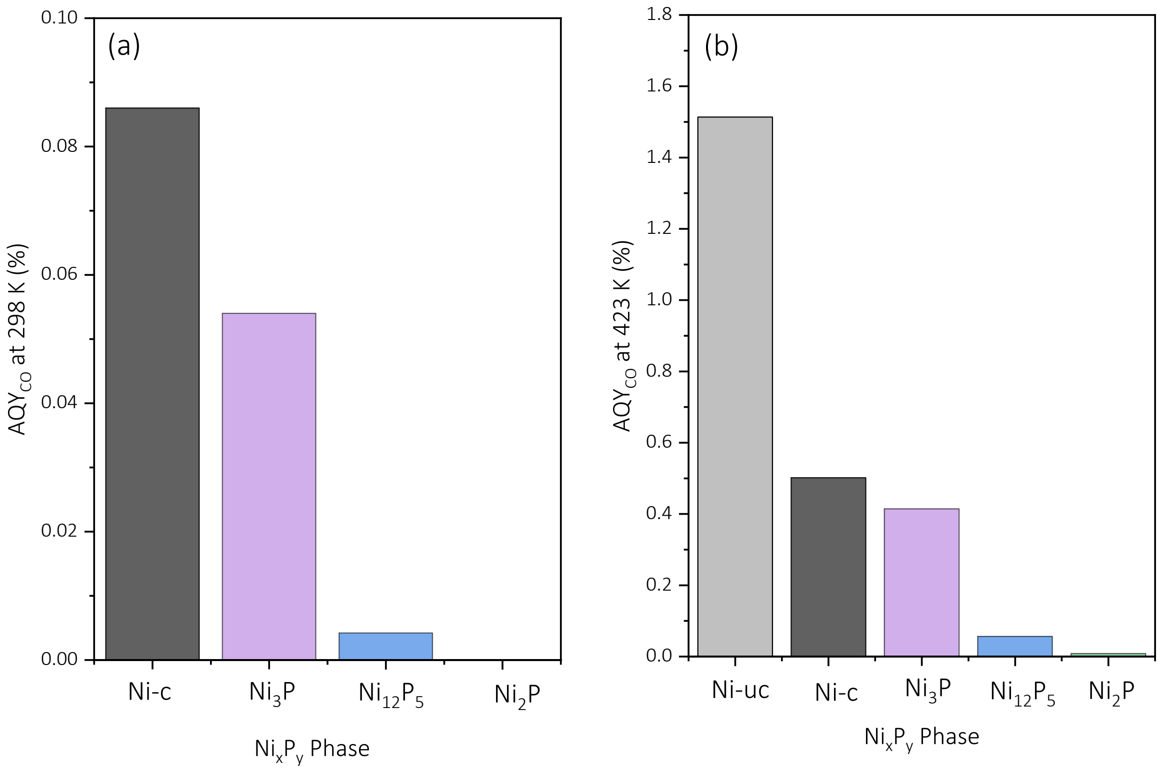

Figure 63. Apparent quantum yield of CO for 2.5 wt% Ni_xP_y/SiO_2 at (a) 298 K and (b) 423 K.

3.5 Photocatalytic Performance: Ni_xP_y/TiO_2

CO_2 HYD study measurements were also carried out for 2.5 wt% Ni_xP_y/TiO_2 catalysts to enable comparison of the Ni_xP_y phsaes on the two support materials (i.e., SiO_2 and TiO_2). Within the timeframe of this project, only $Ni_{12}P_5/TiO_2$ and Ni_2P/TiO_2 were successfully synthesized. Once available, extending this work to additional Ni_xP_y phases is recommended.

CO_2 HYD rate was compared between the two phases as a function of temperature (298–423 K) for the RWGS reaction carried out in light (Figure 64). CO and CH_4 were the only products observed, so CO_2 HYD rate is determined as the sum of their production rates. $Ni_{12}P_5/TiO_2$ had higher rates of CO_2 HYD at all temperatures compared to Ni_2P/TiO_2.

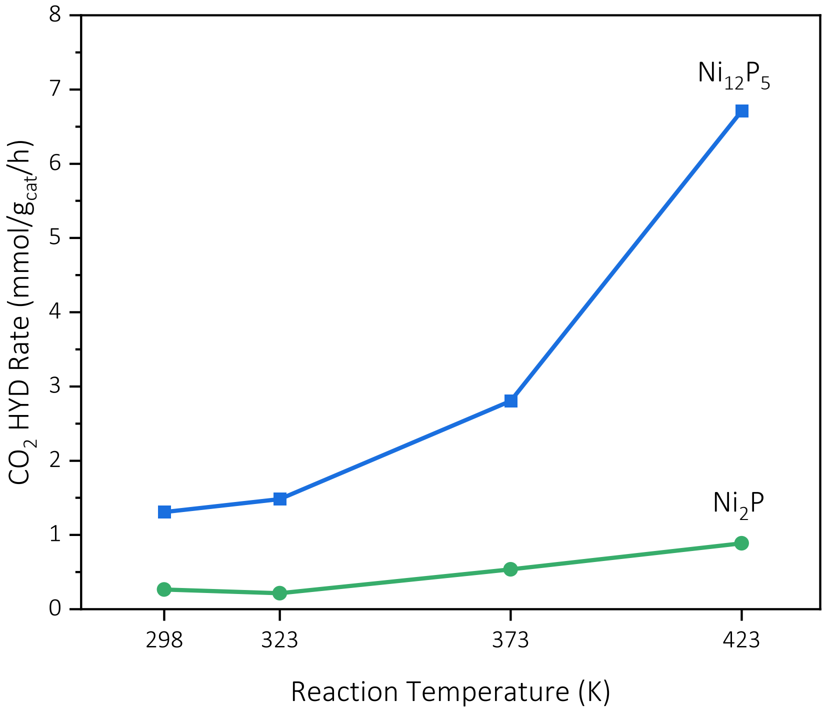

Figure 64. CO_2 HYD rate vs. reaction temperature for the RWGS reaction carried out in light over Ni_xP_y/TiO_2 for $Ni_{12}P_5$ (blue) and Ni_2P (green) phases.

CO production rate was compared between the two Ni_xP_y phases as a function of temperature (298–423 K) for the RWGS reaction carried out in light (Figure 65). In contrast with CO_2 HYD rates, CO production rates were comparable between the two phases, indicating that CH_4 production was a major contributor to the overall CO_2 HYD activity.

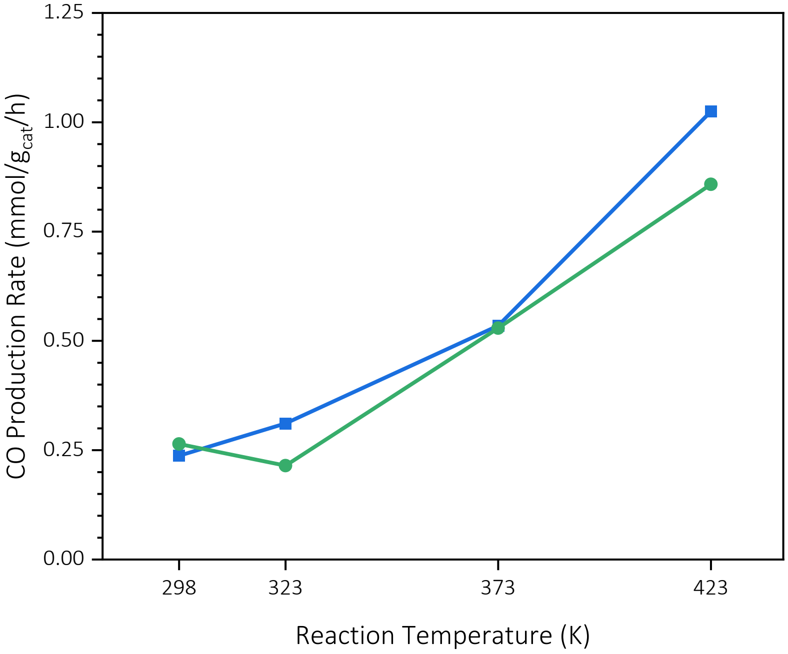

Figure 65. CO production vs. reaction temperature for the RWGS reaction carried out in light over Ni_xP_y/TiO_2 for $Ni_{12}P_5$ (blue) and Ni_2P (green) phases.

CO production rate and selectivity toward CO were compared between the two phases in light at 423 K (Figure 66). As seen with the SiO_2-supported catalysts, the $Ni_{12}P_5$ had higher CO activity than the more phosphorous-rich Ni_2P at 423 K. However, $Ni_{12}P_5/TiO_2$ had very poor selectivity toward CO (~15%) while Ni_2P/TiO_2 maintained high CO selectivity (>96%).

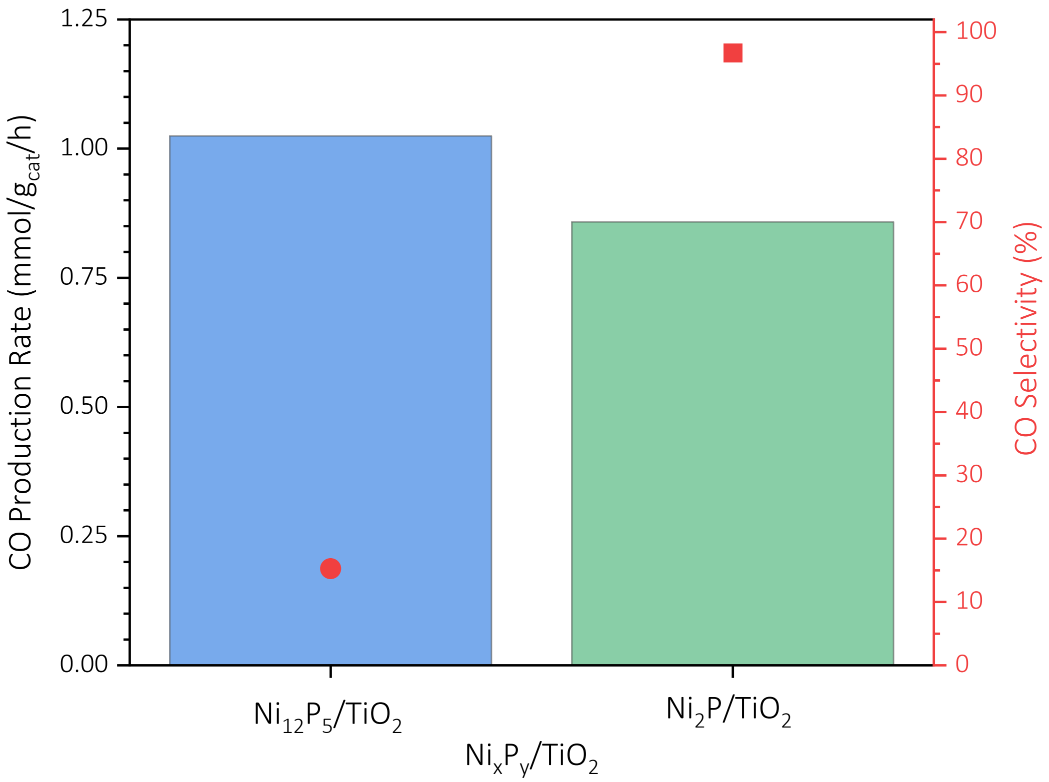

Figure 66. CO production rate and CO selectivity vs. Ni_xP_y phase for the RWGS reaction carried out over 2.5 wt% Ni_xP_y/TiO_2 in the light at 423 K.

Next, SiO_2 and TiO_2 support materials were compared for both Ni_xP_y phases to probe photothermal effects on catalyzed CO_2 HYD (Figure 67). At 423 K in light, $Ni_{12}P_5$ supported on TiO_2 had a 2.6-fold increase in CO production rate compared to SiO_2. Ni_2P had a 21.9-fold increase in CO production rate supported on TiO_2 compared to SiO_2.

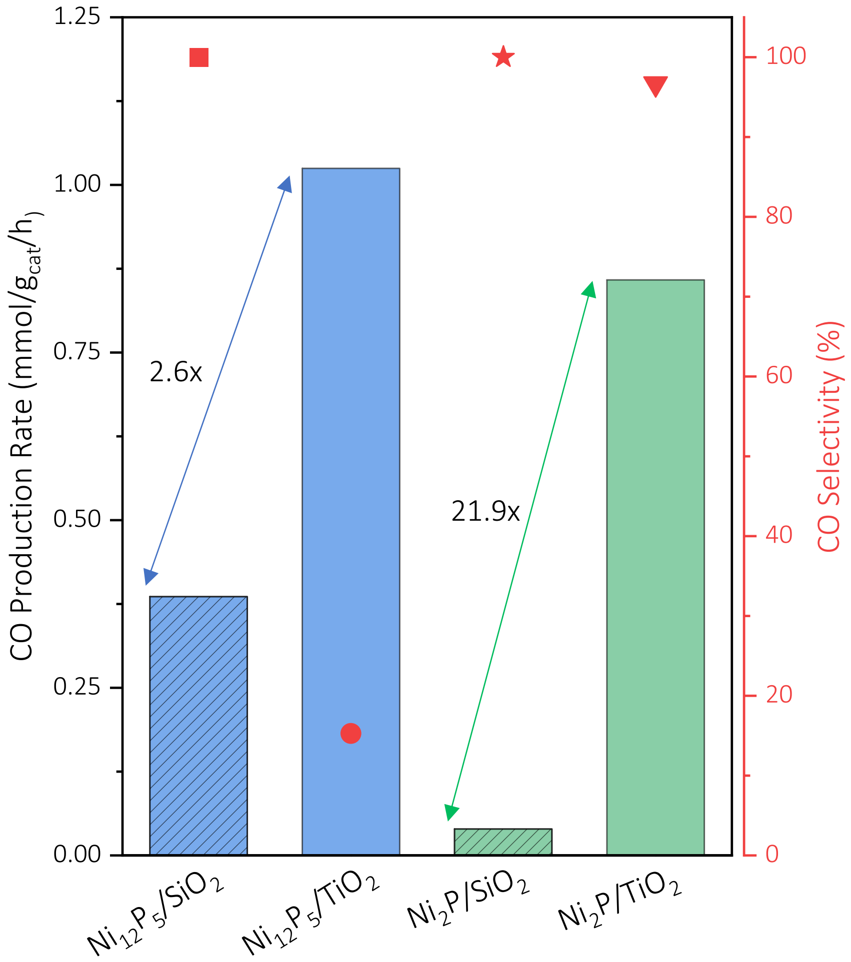

Figure 67. CO production rate over 2.5 wt% Ni_xP_y supported on TiO_2 (shaded) and SiO_2 (solid) in the RWGS reaction at 423 K in the light.

To determine the catalytic contribution of the support materials to the RWGS reaction, a CO_2 HYD study was carried out over the pure supports—TiO_2 and SiO_2—and the empty reactor in light and dark at temperatures of 298–523 K in 50 K intervals (Figure 68). For the empty reactor, a bed of Cab-o-sil was loaded into the sample cup and an in-situ activation was carried out to replicate the reaction conditions used in this work, but no mass was used in the reporting of CO production rate (i.e., mmol/h). Under all reaction conditions, the empty reactor had an activity of

≤ 0.004 mmol/h. At all temperatures, the activity of SiO_2 was consistent with that of the empty reactor in light and dark. However, CO was produced over TiO_2 starting at 473 K in both light and dark.

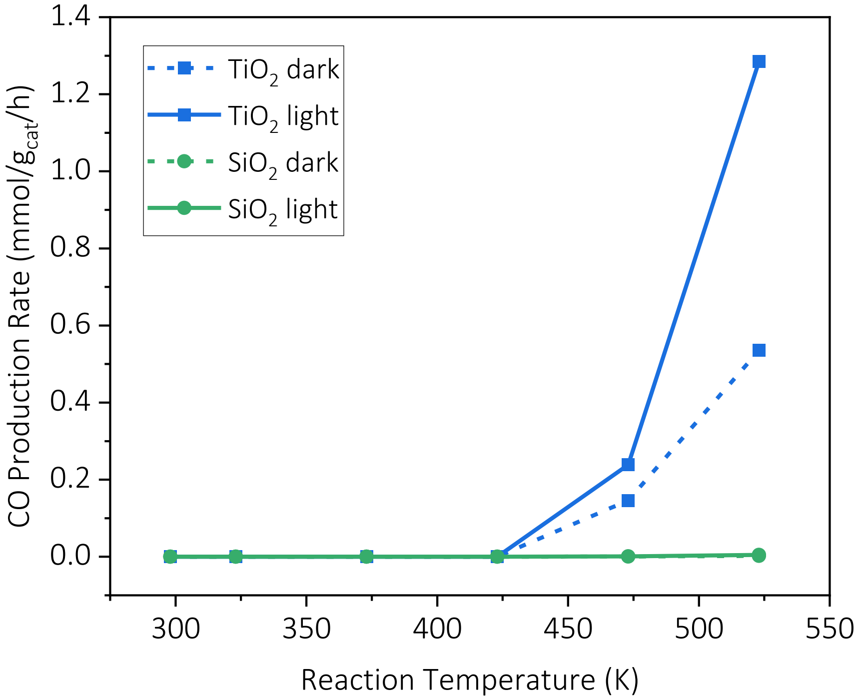

Figure 68. CO production rate for the RWGS reaction carried out over the support materials in light and dark at 298–523 K. Measurements on the empty reactor were carried out, and CO production rate ≤ 0.004 mmol/h under all reaction conditions.

Chapter 4: Conclusions

A series of 2.5 wt% Ni_xP_y/SiO2 and Ni_xP_y/TiO_2 catalyst precursors were synthesized by incipient wetness and wet impregnation, respectively. The precursors were reduced to yield the final product by temperature-programmed reduction under flowing H_2. Adjustments to the nominal amounts and ratio of P and Ni sources were used to achieve the target Ni_xP_y crystalline phase and Ni_xP_y loading (wt%), which were characterized by XRD and ICP-OES, respectively. It was determined that the calcination step used in Ni/SiO_2-c synthesis resulted in an average crystallite size of 13.9 nm, prompting synthesis of an uncalcined version to yield a more comparable average crystallite size to the other Ni_xP_y/SiO_2 catalysts (< 5 nm). Both versions of Ni/SiO_2 were included in subsequent characterizations to probe the effect of size.

Optical absorbance properties were determined by UV-Vis-NIR spectroscopy and revealed a monotonic trend of increasing absorbance intensity with decreasing P/Ni ratio for the Ni_xP_y/SiO_2 catalysts prepared from calcined precursors. However, Ni/SiO_2-uc was lighter in color and had a lower absorbance intensity across the spectrum (250–1250 nm) than Ni/SiO_2-c. Accompanying this, Ni/SiO_2-uc was darker in color following the in-situ activation that preceded CO_2 HYD reactions. It can be concluded that that the absorbance spectrum of the passivated Ni/SiO_2-uc catalyst does not reflect the optical properties of the activated catalyst due to the small size of the Ni crystallites (< 5 nm).

The degree to which P dilution of the Ni ensemble in the supported Ni_xP_y catalysts was beneficial for the RWGS reaction was investigated first on an inert SiO_2 support. CO_2 HYD studies were carried out in light and dark at 298–523 K to evaluate the photothermal catalytic properties. CO activity decreased with increasing P/Ni ratio across all temperatures in light for catalysts of comparable crystallite size. CO chemisorption capacity mirrored this trend: active site density decreased with increasing P/Ni ratio for catalysts. From this it can be concluded that surface Ni atoms are the active sites for CO_2 HYD and that dilution of the Ni ensemble with P reduces the number of active sites. Furthermore, selectivity toward CO increased with increasing P/Ni ratio, suggesting that the presense of P within the Ni ensemble influences the types of binding sites and/or adsorption strength of the intermedates.

At 423 K, all SiO_2-supported Ni_xP_y catalysts had activity in light and dark, enabling comparison for all performance metrics. Ni_3P/SiO_2 had high CO selectivity (≥ 95.7%), photoenhancement of CO production (117-fold rate increase in light), and CO activity (3.3 mmol/g_{cat}/h). The increased relative concentration of P in $Ni_{12}P_5$ correseponded to increased selectivity to 100%, but resulted in a disproportionately deleterious effect on photoenhancement and activity (15.5 light/dark and 0.038 mmol/g_{cat}/h, respectively). This trend persisted for Ni_2P, which had the highest P/Ni ratio.

To gain insight on the role of the support and the Ni_xP_y-support interface, TiO_2-supported $Ni_{12}P_5$ and Ni_2P were also evaluated as photothermal RWGS catalysts. Comparing each Ni_xP_y on both supports, a 2.6-fold increase in CO production was observed for $Ni_{12}P_5$ and a 21.9-fold increase for Ni_2P on TiO_2 compared to SiO_2 at 423 K in light. The selectivity toward CO remained high (96.3%) for Ni_2P on TiO_2, but was vastly lowered for $Ni_{12}P_5$ from 100% on SiO_2 to 15.3% on TiO_2. The low CO selectivity of the $Ni_{12}P_5/TiO_2$ catalyst reaquires further study, noting the unexpecdely low P/Ni ratio measured for this catalyst.

References

(1) *Climate Change 2014: Synthesis Report*; Pachauri, R. K., Mayer, L., Intergovernmental Panel on Climate Change, Eds.; Intergovernmental Panel on Climate Change: Geneva, Switzerland, 2015.

(2) *The Paris Agreement | UNFCCC*. https://unfccc.int/process-and-meetings/the-paris-agreement/the-paris-agreement (accessed 2021-03-18).

(3) Arias, P. A.; Bellouin, N.; Coppola, E.; Jones, R. G.; Krinner, G.; Marotzke, J.; Naik, V.; Palmer, M. D.; Plattner, G.-K.; Rogelj, J.; Rojas, M.; Sillmann, J.; Storelvmo, T.; Thorne, P. W.; Trewin, B.; Achutarao, K. M.; Adhikary, B.; Allan, R. P.; Armour, K.; Bala, G.; Barimalala, R.; Berger, S.; Canadell, J. G.; Cassou, C.; Cherchi, A.; Collins, W.; Collins, W. D.; Connors, S. L.; Corti, S.; Cruz, F. A.; Dentener, F. J.; Dereczynski, C.; Di Luca, A.; Diongue-Niang, A.; Doblas-Reyes, F. J.; Dosio, A.; Douville, H.; Engelbrecht, F.; Eyring, V.; Fischer, E.; Forster, P.; Fox-Kemper, B.; Fuglestvedt, J. S.; Fyfe, J. C.; Gillett, N. P.; Goldfarb, L.; Gorodetskaya, I. V.; Gutiérrez, J. M.; Hamdi, R.; Hawkins, E.; Hewitt, H. T.; Hope, P.; Islam, A. S.; Jones, C.; Kaufman, D. S.; Kopp, R. E.; Kosaka, Y.; Kossin, J.; Krakovska, S.; Lee, J.-Y.; Li, J.; Mauritsen, T.; Maycock, T. K.; Meinshausen, M.; Min, S.-K.; Scheel Monteiro, P.; Ngo-Duc, T.; Otto, F.; Pinto, I.; Pirani, A.; Raghavan, K.; Ranasinghe, R.; Ruane, A. C.; Ruiz, L.; Sallée, J.-B.; Samset, B. H.; Sathyendranath, S.; Seneviratne, S. I.; Sörensson, A. A.; Szopa, S.; Takayabu, I.; Treguier, A.-M.; Hurk, B. van den; Vautard, R.; von Schuckmann, K.; Zaehle, S.; Zhang, X.; Zickfeld, K. Technical Summary. In *Climate Change 2021: The Physical Science Basis. Contribution of Working Group I to the Sixth Assessment Report of the Intergovernmental Panel on Climate Change*; Masson-Delmotte, V., Zhai, P., Pirani, A., Connors, S. L., Péan, C., Berger, S., Caud, N., Chen, Y., Goldfarb, L., Gomis, M. I., Huang, M., Leitzell, K., Lonnoy, E., Matthews, J. B. R., Maycock, T. K., Waterfield, T., Yelekçi, Ö., Yu, R., Zhou, B., Eds.; Cambridge University Press, 2021.

(4) *Greenhouse Gases | Monitoring References | National Centers for Environmental Information (NCEI)*. https://www.ncdc.noaa.gov/monitoring-references/faq/greenhouse-gases.php#intro (accessed 2021-09-02).

(5) US EPA, O. *Overview of Greenhouse Gases*. https://www.epa.gov/ghgemissions/overview-greenhouse-gases (accessed 2021-09-02).

(6) Marchese, M.; Giglio, E.; Santarelli, M.; Lanzini, A. Energy Performance of Power-to-Liquid Applications Integrating Biogas Upgrading, Reverse Water Gas Shift, Solid Oxide Electrolysis and Fischer-Tropsch Technologies. *Energy Convers. Manag. X* **2020**, *6*, 100041. https://doi.org/10.1016/j.ecmx.2020.100041.

(7) Wang, X.; Song, C. Carbon Capture From Flue Gas and the Atmosphere: A Perspective. *Front. Energy Res.* **2020**, *8*, 265. https://doi.org/10.3389/fenrg.2020.560849.

(8) Chen, T.; Wang, Z.; Liu, L.; Pati, S.; Wai, M. H.; Kawi, S. Coupling CO2 Separation with Catalytic Reverse Water-Gas Shift Reaction via Ceramic-Carbonate Dual-Phase Membrane Reactor. *Chem. Eng. J.* **2020**, *379*, 122182. https://doi.org/10.1016/j.cej.2019.122182.

(9) Zhuang, S.; Li, Y.; Zuo, M.; Tan, X.; Meng, B.; Yang, N.; Liu, S. Dense Composite Electrolyte Hollow Fibre Membranes for High Temperature CO2 Separation. *Sep. Purif. Technol.* **2014**, *132*, 712–718. https://doi.org/10.1016/j.seppur.2014.06.025.

(10) Anderson, M.; Lin, Y. S. Carbonate–Ceramic Dual-Phase Membrane for Carbon Dioxide Separation. *J. Membr. Sci.* **2010**, *357* (1), 122–129. https://doi.org/10.1016/j.memsci.2010.04.009.

(11) Chung, S. J.; Park, J. H.; Li, D.; Ida, J.-I.; Kumakiri, I.; Lin, J. Y. S. Dual-Phase Metal−Carbonate Membrane for High-Temperature Carbon Dioxide Separation. *Ind. Eng. Chem. Res.* **2005**, *44* (21), 7999–8006. https://doi.org/10.1021/ie0503141.

(12) *Water gas shift equilibria via the NIST Webbook*. https://kitchingroup.cheme.cmu.edu/blog/2013/02/01/Water-gas-shift-equilibria-via-the-NIST-Webbook/ (accessed 2021-04-09).

(13) gonzález, M.; Arellano-Garcia, H. The Reverse Water Gas Shift Reaction: A Process Systems Engineering Perspective. *React. Chem. Eng.* **2021**, *6*. https://doi.org/10.1039/D0RE00478B.

(14) Wenzel, M.; Rihko-Struckmann, L.; Sundmacher, K. Thermodynamic Analysis and Optimization of RWGS Processes for Solar Syngas Production from CO2. *AIChE J.* **2017**, *63* (1), 15–22. https://doi.org/10.1002/aic.15445.

(15) Kho, E. T.; Tan, T. H.; Lovell, E.; Wong, R. J.; Scott, J.; Amal, R. A Review on Photo-Thermal Catalytic Conversion of Carbon Dioxide. *Green Energy Environ.* **2017**, *2* (3), 204–217. https://doi.org/10.1016/j.gee.2017.06.003.

(16) Schlögl, R. Heterogeneous Catalysis. *Angew. Chem. Int. Ed.* **2015**, *54* (11), 3465–3520. https://doi.org/10.1002/anie.201410738.

(17) Holm, A.; Goodman, E. D.; Stenlid, J. H.; Aitbekova, A.; Zelaya, R.; Diroll, B. T.; Johnston-Peck, A. C.; Kao, K.-C.; Frank, C. W.; Pettersson, L. G. M.; Cargnello, M. Nanoscale Spatial Distribution of Supported Nanoparticles Controls Activity and Stability in Powder Catalysts for CO Oxidation and Photocatalytic H2 Evolution. *J. Am. Chem. Soc.* **2020**, *142* (34), 14481–14494. https://doi.org/10.1021/jacs.0c03842.

(18) Schmid, G. *Nanoparticles: From Theory to Application*; Wiley, 2011.

(19) Prins, R.; Bussell, M. E. Metal Phosphides: Preparation, Characterization and Catalytic Reactivity. *Catal. Lett.* **2012**, *142* (12), 1413–1436. https://doi.org/10.1007/s10562-012-0929-7.

(20) Ghoussoub, M.; Xia, M.; Duchesne, P. N.; Segal, D.; Ozin, G. Principles of Photothermal Gas-Phase Heterogeneous CO2 Catalysis. *Energy Environ. Sci.* **2019**, *12* (4), 1122–1142. https://doi.org/10.1039/C8EE02790K.

(21) Sharma, J. N.; Pattadar, D. K.; Mainali, B. P.; Zamborini, F. P. Size Determination of Metal Nanoparticles Based on Electrochemically Measured Surface-Area-to-Volume Ratios. *Anal. Chem.* **2018**, *90* (15), 9308–9314. https://doi.org/10.1021/acs.analchem.8b01905.

(22) Qi, Y.; Zhu, Y.-A.; Chen, D. Mechanism Investigation and Catalyst Screening of High-Temperature Reverse Water Gas Shift Reaction. *Green Chem. Eng.* **2020**, *1* (2), 131–139. https://doi.org/10.1016/j.gce.2020.10.001.

(23) *Nickel - Element information, properties and uses | Periodic Table*. https://www.rsc.org/periodic-table/element/28/nickel (accessed 2021-04-09).

(24) Jain, A.; Ong, S. P.; Hautier, G.; Chen, W.; Richards, W. D.; Dacek, S.; Cholia, S.; Gunter, D.; Skinner, D.; Ceder, G.; Persson, K. A. Commentary: The Materials Project: A Materials

Genome Approach to Accelerating Materials Innovation. *APL Mater.* **2013**, *1* (1), 011002. https://doi.org/10.1063/1.4812323.

(25) Xu, Y.-F.; Duchesne, P. N.; Wang, L.; Tavasoli, A.; Jelle, A. A.; Xia, M.; Liao, J.-F.; Kuang, D.-B.; Ozin, G. A. High-Performance Light-Driven Heterogeneous CO 2 Catalysis with near-Unity Selectivity on Metal Phosphides. *Nat. Commun.* **2020**, *11* (1), 5149. https://doi.org/10.1038/s41467-020-18943-2.

(26) Du, G.; Lim, S.; Yang, Y.; Wang, C.; Pfefferle, L.; Haller, G. Methanation of Carbon Dioxide on Ni-Incorporated MCM-41 Catalysts: The Influence of Catalyst Pretreatment and Study of Steady-State Reaction. *J. Catal. - J CATAL* **2007**, *249*, 370–379. https://doi.org/10.1016/j.jcat.2007.03.029.

(27) Layman, K. A.; Bussell, M. E. Infrared Spectroscopic Investigation of CO Adsorption on Silica-Supported Nickel Phosphide Catalysts. *J. Phys. Chem. B* **2004**, *108* (30), 10930–10941. https://doi.org/10.1021/jp037101e.

(28) Amin, M. H.; Sudarsanam, P.; Field, M. R.; Patel, J.; Bhargava, S. K. Effect of a Swelling Agent on the Performance of Ni/Porous Silica Catalyst for CH4–CO2 Reforming. *Langmuir* **2017**, *33* (40), 10632–10644. https://doi.org/10.1021/acs.langmuir.7b02753.

(29) Costa, D. C.; Soldati, A. L.; Pecchi, G.; Bengoa, J. F.; Marchetti, S. G.; Vetere, V. Preparation and Characterization of a Supported System of Ni2P/Ni12P5 Nanoparticles and Their Use as the Active Phase in Chemoselective Hydrogenation of Acetophenone. *Nanotechnology* **2018**, *29* (21), 215702. https://doi.org/10.1088/1361-6528/aab3a8.

(30) Yang, Y.; Lim, S.; Du, G.; Chen, Y.; Ciuparu, D.; Haller, G. L. Synthesis and Characterization of Highly Ordered Ni-MCM-41 Mesoporous Molecular Sieves. *J. Phys. Chem. B* **2005**, *109* (27), 13237–13246. https://doi.org/10.1021/jp044227i.

(31) Eskandari, S.; Dong, A.; De Castro, L. T.; AB Rahman, F. B.; Lipp, J.; Blom, D. A.; Regalbuto, J. R. Pushing the Limits of Electrostatic Adsorption: Charge Enhanced Dry Impregnation of SBA-15. *Catal. Today* **2019**, *338*, 60–71. https://doi.org/10.1016/j.cattod.2019.06.082.

(32) Ruiz Puigdollers, A.; Schlexer, P.; Tosoni, S.; Pacchioni, G. Increasing Oxide Reducibility: The Role of Metal/Oxide Interfaces in the Formation of Oxygen Vacancies. *ACS Catal.* **2017**, *7* (10), 6493–6513. https://doi.org/10.1021/acscatal.7b01913.

(33) Sápi, A.; Dobó, D. G.; Sebők, D.; Halasi, G.; Juhász, K. L.; Szamosvölgyi, Á.; Pusztai, P.; Varga, E.; Kálomista, I.; Galbács, G.; Kukovecz, Á.; Kónya, Z. Silica-Based Catalyst Supports Are Inert, Are They Not?: Striking Differences in Ethanol Decomposition Reaction Originated from Meso- and Surface-Fine-Structure Evidenced by Small-Angle X-Ray Scattering. *J. Phys. Chem. C* **2017**, *121* (9), 5130–5136. https://doi.org/10.1021/acs.jpcc.7b00034.

(34) Vella, E.; Messina, F.; Cannas, M.; Boscaino, R. Unraveling Exciton Dynamics in Amorphous Silicon Dioxide: Interpretation of the Optical Features from 8 to 11 EV. *Phys. Rev. B* **2011**, *83* (17), 174201. https://doi.org/10.1103/PhysRevB.83.174201.

(35) Ravindra, N.; Narayan, J. Optical Properties of Amorphous Silicon and Silicon Dioxide. *J. Appl. Phys.* **1986**, *60*, 1139–1146. https://doi.org/10.1063/1.337358.

(36) van Santen, R. A. Heterogeneous Catalysis. In *Modern Heterogeneous Catalysis*; John Wiley & Sons, Ltd, 2017; pp 1–13. https://doi.org/10.1002/9783527810253.ch1.

(37) Wang, L.; Dong, Y.; Yan, T.; Hu, Z.; Jelle, A. A.; Meira, D. M.; Duchesne, P. N.; Loh, J. Y. Y.; Qiu, C.; Storey, E. E.; Xu, Y.; Sun, W.; Ghoussoub, M.; Kherani, N. P.; Helmy, A. S.; Ozin, G. A.

Black Indium Oxide a Photothermal CO 2 Hydrogenation Catalyst. *Nat. Commun.* **2020**, *11* (1), 2432. https://doi.org/10.1038/s41467-020-16336-z.

(38) Yin, G.; Huang, X.; Chen, T.; Zhao, W.; Bi, Q.; Xu, J.; Han, Y.; Huang, F. Hydrogenated Blue Titania for Efficient Solar to Chemical Conversions: Preparation, Characterization, and Reaction Mechanism of CO2 Reduction. *ACS Catal.* **2018**, *8* (2), 1009–1017. https://doi.org/10.1021/acscatal.7b03473.

(39) Hu, X.; Xie, L.; Xu, Z.; Liu, S.; Tan, X.; Qian, R.; Zhang, R.; Jiang, M.; Xie, W.; Tian, W. Photothermal-Enhanced Fenton-like Catalytic Activity of Oxygen-Deficient Nanotitania for Efficient and Safe Tooth Whitening. *ACS Appl. Mater. Interfaces* **2021**, *13* (30), 35315–35327. https://doi.org/10.1021/acsami.1c06774.

(40) Chen, X.; Liu, L.; Yu, P. Y.; Mao, S. S. Increasing Solar Absorption for Photocatalysis with Black Hydrogenated Titanium Dioxide Nanocrystals. *Science* **2011**, *331* (6018), 746–750. https://doi.org/10.1126/science.1200448.

(41) Lei, F.; Sun, Y.; Liu, K.; Gao, S.; Liang, L.; Pan, B.; Xie, Y. Oxygen Vacancies Confined in Ultrathin Indium Oxide Porous Sheets for Promoted Visible-Light Water Splitting. *J. Am. Chem. Soc.* **2014**, *136* (19), 6826–6829. https://doi.org/10.1021/ja501866r.

(42) Hu, J.; Guo, Z.; Mcwilliams, P. E.; Darges, J. E.; Druffel, D. L.; Moran, A. M.; Warren, S. C. Band Gap Engineering in a 2D Material for Solar-to-Chemical Energy Conversion. *Nano Lett.* **2016**, *16* (1), 74–79. https://doi.org/10.1021/acs.nanolett.5b02895.

(43) Qi, Y.; Song, L.; Ouyang, S.; Liang, X.; Ning, S.; Zhang, Q.; Ye, J. Photoinduced Defect Engineering: Enhanced Photothermal Catalytic Performance of 2D Black In2O3−x Nanosheets with Bifunctional Oxygen Vacancies. *Adv. Mater.* **2020**, *32* (6), 1903915. https://doi.org/10.1002/adma.201903915.

(44) Kattel, S.; Yan, B.; Chen, J. G.; Liu, P. CO2 Hydrogenation on Pt, PtiSiO(2) and Pt/TiO2: Importance of Synergy between Pt and Oxide Support. 41.

(45) Cargnello, M.; Montini, T.; Smolin, S. Y.; Priebe, J. B.; Delgado Jaén, J. J.; Doan-Nguyen, V. V. T.; McKay, I. S.; Schwalbe, J. A.; Pohl, M.-M.; Gordon, T. R.; Lu, Y.; Baxter, J. B.; Brückner, A.; Fornasiero, P.; Murray, C. B. Engineering Titania Nanostructure to Tune and Improve Its Photocatalytic Activity. *Proc. Natl. Acad. Sci. U. S. A.* **2016**, *113* (15), 3966–3971. https://doi.org/10.1073/pnas.1524806113.

(46) Zhang, A.-Y.; Lin, T.; He, Y.-Y.; Mou, Y.-X. Heterogeneous Activation of H2O2 by Defect-Engineered TiO(2-x) Single Crystals for Refractory Pollutants Degradation: A Fenton-like Mechanism. *J. Hazard. Mater.* **2016**, *311*, 81–90. https://doi.org/10.1016/j.jhazmat.2016.02.071.

(47) Bai, Y.; Mora-Seró, I.; De Angelis, F.; Bisquert, J.; Wang, P. Titanium Dioxide Nanomaterials for Photovoltaic Applications. *Chem. Rev.* **2014**, *114* (19), 10095–10130. https://doi.org/10.1021/cr400606n.

(48) Zhang, M.; Chen, T.; Wang, Y. Insights into TiO2 Polymorphs: Highly Selective Synthesis, Phase Transition, and Their Polymorph-Dependent Properties. *RSC Adv.* **2017**, *7* (83), 52755–52761. https://doi.org/10.1039/C7RA11515F.

(49) Prins, R. Hydrogen Spillover. Facts and Fiction. *Chem. Rev.* **2012**, *112* (5), 2714–2738. https://doi.org/10.1021/cr200346z.

(50) Mateo, D.; Cerrillo, J. L.; Durini, S.; Gascon, J. Fundamentals and Applications of Photo-Thermal Catalysis. *Chem. Soc. Rev.* **2021**, *50* (3), 2173–2210. https://doi.org/10.1039/D0CS00357C.
(51) Alex Bullock. Research Report Fall 2021, 2021.
(52) Hargreaves, J. S. J. Some Considerations Related to the Use of the Scherrer Equation in Powder X-Ray Diffraction as Applied to Heterogeneous Catalysts. *Catal. Struct. React.* **2016**, *2* (1–4), 33–37. https://doi.org/10.1080/2055074X.2016.1252548.
(53) Gates-Rector, S.; Blanton, T. The Powder Diffraction File: A Quality Materials Characterization Database. *Powder Diffr.* **2019**, *34* (4), 352–360. https://doi.org/10.1017/S0885715619000812.
(54) Jake Schare. Summer 2021 Research Report, 2021.
(55) Wang, X.; Chen, Z.; Saito, K.; Tanaka, T.; Nishio, M.; Guo, Q. Temperature-Dependent Raman Scattering in Cubic (InGa)2O3 Thin Films. *J. Alloys Compd.* **2017**, *690*, 287–292. https://doi.org/10.1016/j.jallcom.2016.08.129.
(56) Wang, D.; Chen, B.; Zhao, J. Lattice Vibration Fundamentals of Nanocrystalline Anatase: Temperature-Dependent Study Using Micro-Raman Scattering Spectroscopy. *J. Appl. Phys.* **2007**, *101* (11), 113501. https://doi.org/10.1063/1.2736309.
(57) Wang, R.; Xu, S.; Yue, Y.; Wang, X. Thermal Behavior of Materials in Laser-Assisted Extreme Manufacturing: Raman-Based Novel Characterization. *Int. J. Extreme Manuf.* **2020**, *2* (3), 032004. https://doi.org/10.1088/2631-7990/aba17c.
(58) Jake Schare. Winter Quarter 2021 Research Summary, 2021.
(59) Jake Schare. Summer Research Goals and Updates, 2021.
(60) Stern, E. Winter 2022 Final Report, 2022.
(61) Jia, J.; Wang, H.; Lu, Z.; O'Brien, P. G.; Ghoussoub, M.; Duchesne, P.; Zheng, Z.; Li, P.; Qiao, Q.; Wang, L.; Gu, A.; Jelle, A. A.; Dong, Y.; Wang, Q.; Ghuman, K. K.; Wood, T.; Qian, C.; Shao, Y.; Qiu, C.; Ye, M.; Zhu, Y.; Lu, Z.-H.; Zhang, P.; Helmy, A. S.; Singh, C. V.; Kherani, N. P.; Perovic, D. D.; Ozin, G. A. Photothermal Catalyst Engineering: Hydrogenation of Gaseous CO2 with High Activity and Tailored Selectivity. *Adv. Sci.* **2017**, *4* (10), 1700252. https://doi.org/10.1002/advs.201700252.
(62) Vogt, C.; Groeneveld, E.; Kamsma, G.; Nachtegaal, M.; Lu, L.; Kiely, C. J.; Berben, P. H.; Meirer, F.; Weckhuysen, B. M. Unravelling Structure Sensitivity in CO2 Hydrogenation over Nickel. *Nat. Catal.* **2018**, *1*, 127–134. https://doi.org/10.1038/s41929-017-0016-y.
(63) Galhardo, T. S.; Braga, A. H.; Arpini, B. H.; Szanyi, J.; Gonçalves, R. V.; Zornio, B. F.; Miranda, C. R.; Rossi, L. M. Optimizing Active Sites for High CO Selectivity during CO2 Hydrogenation over Supported Nickel Catalysts. *J. Am. Chem. Soc.* **2021**, *143* (11), 4268–4280. https://doi.org/10.1021/jacs.0c12689.
(64) Witzke, M. E.; Almithn, A.; Conrad, C. L.; Hibbitts, D. D.; Flaherty, D. W. Mechanisms and Active Sites for C–O Bond Rupture within 2-Methyltetrahydrofuran over Ni, Ni12P5, and Ni2P Catalysts. *ACS Catal.* **2018**, *8* (8), 7141–7157. https://doi.org/10.1021/acscatal.7b04403.
(65) Chen, S.; Xiao, Y.; Wang, Y.; Hu, Z.; Zhao, H.; Xie, W. A Facile Approach to Prepare Black TiO2 with Oxygen Vacancy for Enhancing Photocatalytic Activity. *Nanomaterials* **2018**, *8* (4), 245. https://doi.org/10.3390/nano8040245.

(66) Zhu, K.-R.; Zhang, M.-S.; Chen, Q.; Yin, Z. Size and Phonon-Confinement Effects on Low-Frequency Raman Mode of Anatase TiO2 Nanocrystal. *Phys. Lett. A* **2005**, *340* (1), 220–227. https://doi.org/10.1016/j.physleta.2005.04.008.

(67) Li, W. S.; Shen, Z. X.; Feng, Z. C.; Chua, S. J. Temperature Dependence of Raman Scattering in Hexagonal Gallium Nitride Films. *J. Appl. Phys.* **2000**, *87* (7), 3332–3337. https://doi.org/10.1063/1.372344.